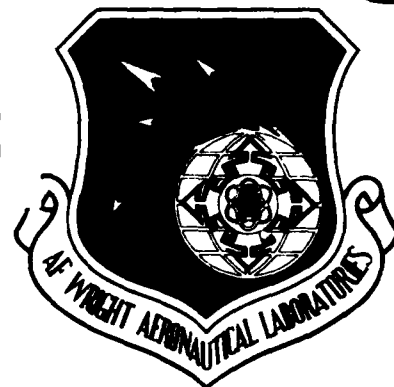


DTIC FILE COPY

AD-A203 911

AFWAL-TR-88-1125



SPECTROSCOPY AND LASER PERFORMANCE OF TI³⁺ DOPED AND Cr³⁺, Nd³⁺ CO-DOPED CRYSTALS

**K. L. Schepler
Electro-Optics Technology Branch
Electronic Technology Division**

AUGUST 1988

**Final Report for Period:
November 1984 - December 1987**

Approved for public release; distribution unlimited.

**DTIC
ELECTE
S E D**

**Avionics Laboratory
Air Force Wright Aeronautical Laboratories
Air Force Systems Command
Wright-Patterson Air Force Base, Ohio 45433**

89 1 24 020

NOTICE

When Government drawings, specifications, or other data are used for any purpose other than in connection with a definitely Government-related procurement, the United States Government incurs no responsibility or any obligation whatsoever. The fact that the Government may have formulated or in any way supplied the said drawings, specifications, or other data, is not to be regarded by implication, or otherwise in any manner construed, as licensing the holder, or any other person or corporation; or as conveying any rights or permission to manufacture, use, or sell any patented invention that may in any way be related thereto.

This report has been reviewed by the office of public affairs (ASD/CPA) and is releasable to the National Technical Information Service (NTIS). At NTIS, it will be available to the general public, including foreign nations.

This technical report has been reviewed and is approved for publication.

Kenneth L. Schepler
KENNETH L. SCHEPLER, Physicist
Electro-Optics Sources Group
Electro-Optics Technology Branch

Virginia McMullan
VIRGINIA MCMILLAN, Acting Chief
Electro-Optics Sources Group
Electro-Optics Technology Branch

FOR THE COMMANDER

Donald J. Smith
DONALD J. SMITH, Acting Chief
Electro-Optics Technology Branch
Electronic Technology Division

If your address has changed, if you wish to be removed from our mailing list, or if the addressee is no longer employed by your organization please notify AFWAL/ELOS, Wright-Patterson AFB, OH 45433-6543 to help us maintain a current mailing list.

Copies of this report should not be returned unless return is required by security considerations, contractual obligations, or notice on a specific document.

UNCLASSIFIED

ADA203911

SECURITY CLASSIFICATION OF THIS PAGE

REPORT DOCUMENTATION PAGE

Form Approved
OMB No. 0704-0188

1a. REPORT SECURITY CLASSIFICATION UNCLASSIFIED		1b. RESTRICTIVE MARKINGS	
2a. SECURITY CLASSIFICATION AUTHORITY		3. DISTRIBUTION/AVAILABILITY OF REPORT Approved for public release; distribution unlimited	
2b. DECLASSIFICATION/DOWNGRADING SCHEDULE		5. MONITORING ORGANIZATION REPORT NUMBER(S)	
4. PERFORMING ORGANIZATION REPORT NUMBER(S) AFWAL-TR-88-1125		7a. NAME OF MONITORING ORGANIZATION	
6a. NAME OF PERFORMING ORGANIZATION Air Force Wright Aeronautical Laboratories	6b. OFFICE SYMBOL (if applicable) AFWAL/AADO-1	7b. ADDRESS (City, State, and ZIP Code)	
6c. ADDRESS (City, State, and ZIP Code) Wright-Patterson AFB OH 45433-6543		9. PROCUREMENT INSTRUMENT IDENTIFICATION NUMBER	
8a. NAME OF FUNDING/SPONSORING ORGANIZATION	8b. OFFICE SYMBOL (if applicable)	10. SOURCE OF FUNDING NUMBERS	
8c. ADDRESS (City, State, and ZIP Code)		PROGRAM ELEMENT NO. 61101F	TASK NO. A5
		PROJECT NO. ILIR	WORK UNIT ACCESSION NO. 04
11. TITLE (Include Security Classification) Spectroscopy and Laser Performance of Ti^{3+} Doped and Cr^{3+}, Nd^{3+} Co-doped Crystals			
12. PERSONAL AUTHOR(S) K. L. Schepler			
13a. TYPE OF REPORT Final	13b. TIME COVERED FROM 11-84 TO 12-84	14. DATE OF REPORT (Year, Month, Day) 1988 August 24	15. PAGE COUNT 108
16. SUPPLEMENTARY NOTATION This research was partially funded by the Inhouse Independent Research Fund. Neodymium, Chromium,			
17. COSATI CODES		18. SUBJECT TERMS (Continue on reverse if necessary and identify by block number)	
FIELD	GROUP	SUB-GROUP	
20	05	tunable lasers, energy transfer, titanium lasers, Aluminum Oxides	
20	06	Ti:sapphire, Ti:YALO, Ti:YAG, Ti:GSAG, Cr,Nd:GSGG, fluorescence, nonradiative relaxation, YAG lasers. (mgm)	
19. ABSTRACT (Continue on reverse if necessary and identify by block number) Lasers used in airborne applications need to be compact, rugged, versatile, and efficient. The objective of this inhouse research program was to explore, assess, and demonstrate the performance of new, solid-state laser materials which have high efficiency and broadband tunability. The temperature-dependent spectroscopy of titanium doped sapphire was investigated in detail. Laser performance of commercially available Ti:sapphire crystals was demonstrated to be near the theoretical quantum slope efficiency limit. Tuning was demonstrated over the 695-864 nm region using a single set of mirrors. Mirror damage limited energy per pulse to 8 mJ. Ti^{3+} ions were introduced into other crystalline hosts. Spectroscopic samples of $Ti:YALO_3$, $Ti:YAG$, and $Ti:GSAG$ (Gd-Sc-Al garnet) were grown. Absorption, fluorescence and fluorescence lifetime were measured for each of these samples. Based on a configuration coordinate model which includes Jahn-Teller and nonradiative relaxation effects, the (SEE REVERSE SIDE)			
20. DISTRIBUTION/AVAILABILITY OF ABSTRACT <input checked="" type="checkbox"/> UNCLASSIFIED/UNLIMITED <input type="checkbox"/> SAME AS RPT. <input type="checkbox"/> DTIC USERS		21. ABSTRACT SECURITY CLASSIFICATION UNCLASSIFIED	
22a. NAME OF RESPONSIBLE INDIVIDUAL K. L. Schepler		22b. TELEPHONE (Include Area Code) (513) 255-3804	22c. OFFICE SYMBOL AFWAL/AADO

BLOCK 19 CONTINUED

spectroscopic properties of Ti^{3+} ions in all hosts studied were successfully interpreted. Crystal field strength was found to play a dominant role in Ti^{3+} optical properties and decreased in the following order ($YAlO_3 : Al_2O_3 : YAG : GSAG$). Nonradiative relaxation rates were found to be extremely sensitive to crystal field strength. Fits of temperature-dependent lifetime data to a quantum mechanical, harmonic-oscillator model showed that nonradiative relaxation is so high in $Ti:GSAG$ that radiative relaxation is almost totally quenched at room temperature. In contrast, $Ti:YAlO_3$ showed little sign of nonradiative relaxation even at temperatures up to 400 K. Good host materials for titanium must have crystal field strengths equal to or greater than that of $Ti:sapphire$.

The spectroscopic and lasing properties of co-doped $Cr,Nd:GSGG$ (Gd-Sc-Ga garnet) were measured. Long-pulse slope efficiency of 8.9% was demonstrated at energies up to 700 mJ in $Cr,Nd:GSGG$ with no falloff in efficiency at the higher energies; $Nd:YAG$ in the same cavity had a slope efficiency of 4.7%. $Cr,Nd:GSGG$ and $Nd:YAG$ Q-switched slope efficiencies of 3.4% and 2.7%, respectively, were demonstrated. The reduced relative performance of $Cr,Nd:GSGG$ when Q-switched may be due to higher thermal birefringence losses.

FOREWORD

This final report describes the results of an In-house Laboratory Director's Independent Research program (ILIRA504) to investigate the spectroscopy and laser performance of new solid-state laser materials. Program management and technical effort were performed by Dr. K. L. Schepler. Mr. W. Deleranko, Mr. R. Wade, and Capt. R. Simpson assisted with data acquisition and analysis. Helpful discussions with Mr. D. Smith, Dr. A. Sanchez, and Dr. P. Moulton are gratefully acknowledged. Finally, the diligent efforts of crystal growers at Airtron, Allied, Crystal Systems, Materials Progress, and Union Carbide to make crystal samples available are acknowledged with thanks.

Accession For	
NTIS GRA&I	<input checked="checked" type="checkbox"/>
DTIC TAB	<input type="checkbox"/>
Unannounced	<input type="checkbox"/>
Justification	
By _____	
Distribution/	
Availability Codes	
Dist	Avail and/or Special
A-1	



TABLE OF CONTENTS

<u>SECTION</u>	<u>Page</u>
INTRODUCTION	1
1 Ti:sapphire Assessment	3
Ti:sapphire Sample Identification	3
Ti:sapphire Absorption Spectra	4
Ti:sapphire Fluorescence	4
Ti:sapphire Zero Phonon Linewidth Measurements	10
Fluorescence Lifetime	13
Quantum Efficiency	20
2 Other Ti^{3+} Doped Materials	22
$Ti^{3+}:YAlO_3$	22
$Ti^{3+}:YAG$	31
$Ti^{3+}:GSGG$	34
$Ti^{3+}:GSAG$	36
3 Theoretical Review of Ti^{3+} Spectroscopic Properties	41
The Vibronic Hamiltonian	41
Configuration-Coordinate Model	44
Jahn-Teller Effect on Ti^{3+} Ions	47
Ti^{3+} Optical Properties	52
4 Comparison of Ti^{3+} Spectroscopic Properties in	
Different Hosts	55
Ti^{3+} Energy Levels	55
Thermal Dependence of Lifetime	60
5 Laser Performance of Ti^{3+} Doped Sapphire	74

SECTION**Page**

6	Cr,Nd:GSGG Lasing Performance	80
	Cr,Nd:GSGG Spectroscopy	80
	Long-Pulse Lasing Performance	83
	Q-switched Laser Performance	88
REFERENCES		94

LIST of ILLUSTRATIONS

<u>Figure</u>		<u>Page</u>
1	Polarized absorption spectra of Ti^{3+} :sapphire sample CS-H at room temperature	5
2	Diagram of the experimental arrangement to measure laser pumped fluorescence of temperature controlled samples.	6
3	Polarized fluorescence of Ti^{3+} :sapphire at 11 and 300 K. The inset shows sharp zero-phonon features at 11 K	8
4	Half-maximum intensity positions of Ti^{3+} :sapphire broadband fluorescence.	9
5	Linewidth of R_1 , the higher energy zero-phonon line, in four Ti^{3+} :sapphire samples	11
6	Linewidth of R_2 , the lower energy zero-phonon line, in four Ti^{3+} :sapphire samples	12
7	Fit of a theoretical linewidth model to experimental data.	14
8	Integrated intensity of Ti^{3+} :sapphire R_1 line fluorescence.	15
9	Time dependence of Ti^{3+} :sapphire fluorescence when pumped by 532 nm, 10 ns pulses at room temperature. The large noise spikes at the beginning of the pulse are due to electromagnetic interference from the pump laser.	17

<u>Figure</u>		<u>Page</u>
10	Logarithmic plot of the Ti^{3+} :sapphire fluorescence data shown in Figure 9.	18
11	Ti^{3+} :sapphire lifetime as a function of temperature	19
12	Ti^{3+} :sapphire integrated fluorescence intensity . .	21
13	Ti^{3+} : YAlO_3 absorption at room temperature	23
14	Polarized Ti^{3+} : YAlO_3 fluorescence (a) at 11 K and (b) at 300 K. Zero-phonon emission at 540 nm is shown in the inset.	25
15	Half-maximum intensity positions of Ti^{3+} : YAlO_3 broadband fluorescence.	26
16	Ti^{3+} : YAlO_3 broadband fluorescence linewidth	27
17	Ti^{3+} : YAlO_3 fluorescence lifetime and integrated intensity vs. temperature	29
18	Experimental arrangement to measure single-pass gain in Ti^{3+} : YAlO_3	30
19	Ti^{3+} :YAG absorption at room temperature	32
20	Ti^{3+} :YAG fluorescence at 12 and 300 K. Zero-phonon emission in the 650 - 655 nm region is shown in the inset	33
21	Ti^{3+} :YAG fluorescence lifetime and integrated intensity vs. temperature	35

22	Absorption at room temperature by (a) a Ti^{3+} :GSAG crystal and by (b) a Ce^{3+} :GSAG crystal. The presence of a peak at 450 nm in sample (a) indicates that some Ce^{3+} impurity ions are present. The weak features at 520 and 620 nm are Ti^{3+} absorption.	37
23	Ti^{3+} :GSAG fluorescence at 12 and 300 K. Zero-phonon emission in the 690 nm region is shown in the inset	38
24	Ti^{3+} :GSAG fluorescence lifetime and integrated intensity vs. temperature	40
25	Splitting of a d orbital under crystal fields of successively lower symmetry	42
26	Generalized configuration coordinate diagram for a transition metal ion with two vibrationally coupled energy levels. The excited state is also Stokes shifted	46
27	Ti^{3+} Jahn-Teller distorted potential energy surfaces. The energy separation of the two levels and the ${}^2\text{T}_2$ spread in paraboloid minima are exaggerated for clarity	50
28	Cross-sectional view of one of the ${}^2\text{T}_2$ paraboloids along its centroid and the corresponding slice through the excited ${}^2\text{E}$ level. This figure is to scale for the model calculations of Section 4 . . .	53

<u>Figure</u>		<u>Page</u>
29	Illustration of configuration coordinate model parameters.	64
30	Model fit of $\text{Ti}^{3+}:\text{YAlO}_3$ fluorescence lifetime . . .	68
31	Model fit of $\text{Ti}^{3+}:\text{sapphire}$ fluorescence lifetime. .	69
32	Model fit of $\text{Ti}^{3+}:\text{YAG}$ fluorescence lifetime	70
33	Model fit of $\text{Ti}^{3+}:\text{GSAG}$ fluorescence lifetime. . . .	71
34	Experimental apparatus used to measure $\text{Ti}^{3+}:\text{sapphire}$ laser performance	75
35	$\text{Ti}^{3+}:\text{sapphire}$ laser performance when pumped with 532 nm, Q-switched pulses	77
36	$\text{Ti}^{3+}:\text{sapphire}$ tuning demonstrated using a single set of mirrors.	78
37	Cr,Nd:GS GG absorption spectrum. Broadband peaks at 460 and 640 nm are Cr^{3+} absorption; sharp peaks are Nd^{3+} absorption	81
38	Cr,Nd:GS GG fluorescence at room temperature pumped by an argon ion laser at 488 nm	82
39	Laser performance of Cr,Nd:GS GG and Nd:YAG. Rod diameters were 5 mm and 1/4 inch respectively . . .	84
40	Long term change in laser output near threshold after pumping at high input energies.	85

<u>Figure</u>		<u>Page</u>
41	Cr,Nd:GSGG long-pulse laser performance	87
42	Cr,Nd:GSGG vs. Nd:YAG long-pulse laser performance.	89
43	Cr,Nd:GSGG vs. Nd:YAG Q-switched laser performance.	90
44	Cr,Nd:GSGG Q-switched pulse width for two pump energies.	92
45	Nd:YAG Q-switched pulse width	93

LIST of TABLES

<u>Table</u>		<u>Page</u>
1	Ti:Sapphire Sample Identification	3
2	Normal Modes for the Octrahedral XY_6 Complex . . .	49
3	Ti^{3+} Spectroscopy Calculations.	59
4	Cr^{3+} Absorption Peaks	60
5	Titanium Lifetime Modeling.	66
6	Integrated Intensity S Values	67
7	Laser Rod Doping Levels	86

INTRODUCTION

Lasers used in airborne applications need to be compact, rugged, versatile, and efficient. These requirements match very well with the properties of solid-state laser materials. Since its discovery in 1964¹ Nd:YAG has been shown to be a useful laser material not only in military applications but also in numerous commercial and scientific applications where a reliable and efficient laser is needed. However, Nd:YAG also has definite limitations. Energy conversion efficiency is limited to typically less than 3% for low energy (≤ 1 J/pulse) Q-switched operation. At higher energies thermal birefringence and thermal stress become severe problems. Nd:YAG also has the basic limitation that it can lase at only a few specific wavelengths, primarily 1.064 μm , with even less efficiency at a few other wavelengths. Often wavelength tunability (in some cases discrete switching among several wavelengths and in other cases continuous tunability) is needed for certain applications and the only way of achieving that with Nd:YAG is to use nonlinear processes such as frequency doubling, Raman conversion, and optical parametric oscillator conversion. But there are concomitant sacrifices in decreased efficiency and increased complexity.

The objective of this in-house program was to explore, assess, and demonstrate the performance of new solid-state materials which have high efficiency and broadband tunability. Laser research in the late 70's resulted in the discovery of some promising new solid-state laser materials. One important breakthrough which encouraged a renaissance in solid-state laser research was the discovery of alexandrite (Cr^{3+} doped chrysoberyl). In 1978, alexandrite was shown to be continuously tunable in the 700-800 nm region² and was the first solid-state laser material capable of tunable laser operation at room temperature.

The discovery of alexandrite encouraged investigators to consider other host-dopant combinations as possible tunable lasers. As part of an AFWAL funded program³ P. Moulton investigated sapphire (Al_2O_3) doped with Ti^{3+} ions. He found that this material lased tunably over the extremely broad range of 660 - 990 nm.⁴

At about the same time, efficiency almost two times higher than Nd:YAG was reported for a new co-doped laser material.⁵ The host material was a garnet with gadolinium, scandium, and gallium occupying the dodecahedral (8 coordinated O^{2-} ions), the octahedral (6 coordinated O^{2-} ions) and the tetrahedral (4 coordinated O^{2-} ions) sites respectively. The garnet was doped with Cr^{3+} substituting at the octahedral sites and Nd^{3+} substituting at the dodecahedral sites. Broadband absorption by the Cr^{3+} ions and rapid transfer to the Nd^{3+} ions enabled Nd,Cr:GSGG to be more efficient than Nd:YAG.

New, solid-state laser materials such as Ti:sapphire and Cr,Nd:GSGG showed strong potential for improved performance in military applications over currently used materials. However, they needed further investigation. This in-house program was initiated to assess their strengths and weaknesses. Experimental measurements of spectroscopy and laser performance plus theoretical modeling of the results will be presented in this report.

SECTION 1

Ti:sapphire Assessment

Ti:sapphire Sample Identification

Crystalline samples of Ti:sapphire were acquired from MIT Lincoln Labs; Crystal Systems Inc., Union Carbide, and Oklahoma State University. Most of the samples were small single crystals suitable for spectroscopic measurements. These varied in doping level depending on the source and growth technique used. The absolute value of the titanium concentration was difficult to measure but the relative concentrations were calculated from spectrophotometer measurements of absorbance at a specific wavelength. Moulton⁶ has measured the EIIc absorption cross section to be $6.4 \times 10^{-20} \text{ cm}^2$ at 490 nm. Sample identifications and relative Ti^{3+} concentrations based on Moulton's calibration factor are given in Table 1.

TABLE 1

TI:SAPPHIRE SAMPLE IDENTIFICATION

<u>Sample ID</u>	<u>Source</u>	<u>Size</u>	<u>Abs. Coeff. [cm⁻¹]</u>	<u>Ti³⁺ Wt%</u>
CS-L	a	1 cm diam x 0.86 cm	0.26	0.0088
CS-H	a	1 cm diam x 0.80 cm	0.53	0.018
UC-H	b	irreg. .33 cm thick	2.3	0.078
LT	c	0.2 x 0.2 x 1.1 cm	0.05	0.0017
UC-B	b	0.5 cm diam x 4.8 cm	—	0.1*
CS-B	a	0.7 cm diam x 3.5 cm	—	0.03*

a Crystal Systems, Inc. - Heat Exchanger Method

b Union Carbide - Czochralski Method

c Army Materials Research Center (Cazlovsky) - Heat Exchanger

* The UC-B rod concentration is shown as reported by the grower. The CS-B rod concentration was measured relative to it.

Ti:sapphire Absorption Spectra

Absorption spectra were taken first using a Cary 14 and later using a Perkin Elmer Lambda 9. Figure 1 shows the polarized absorption spectra of sample CS-H at room temperature. The two peaks at 490 and 560 nm are characteristic of Ti^{3+} ions. Some early Ti:sapphire crystals had a broadband absorption peak in the 800-nm region which could be removed with an annealing treatment. Since this peak was located in the lasing region, it was detrimental to laser performance. In fact, users of Ti:sapphire often characterize the quality of a sample by the ratio of the absorption coefficient near the 490-nm peak and at 800 nm. In this sample the ratio was 115 which is quite good. The 800-nm peak is believed to be due to Ti^{3+} - Ti^{4+} pair formation⁷. The ultraviolet absorption edge is probably a combination of Ti^{4+} and lattice absorption.

Polarization dependence of Ti:sapphire absorption is also shown in Figure 1. Sapphire is uniaxial (one optic axis - the c axis) so absorption is shown for the a and the c axes. Polarization measurements were taken by using polarizer/depolarizer combinations in the spectrophotometer sample and reference beams. The two polarization spectra had identical shapes but the E1lc absorption spectrum was more intense by a factor of 2.5 than the E1la spectrum. In contrast, the E1lc absorption at 800 nm is less than the E1la absorption; this is fortuitous for laser operation where emission is polarized along the c axis.

Ti:sapphire Fluorescence

Fluorescence spectra were taken using a SPEX 1.26-m spectrometer and a Spectra Physics 165 argon ion laser as a pump source. A diagram of the experimental arrangement is shown in Figure 2. Temperature-dependent measurements were taken using an

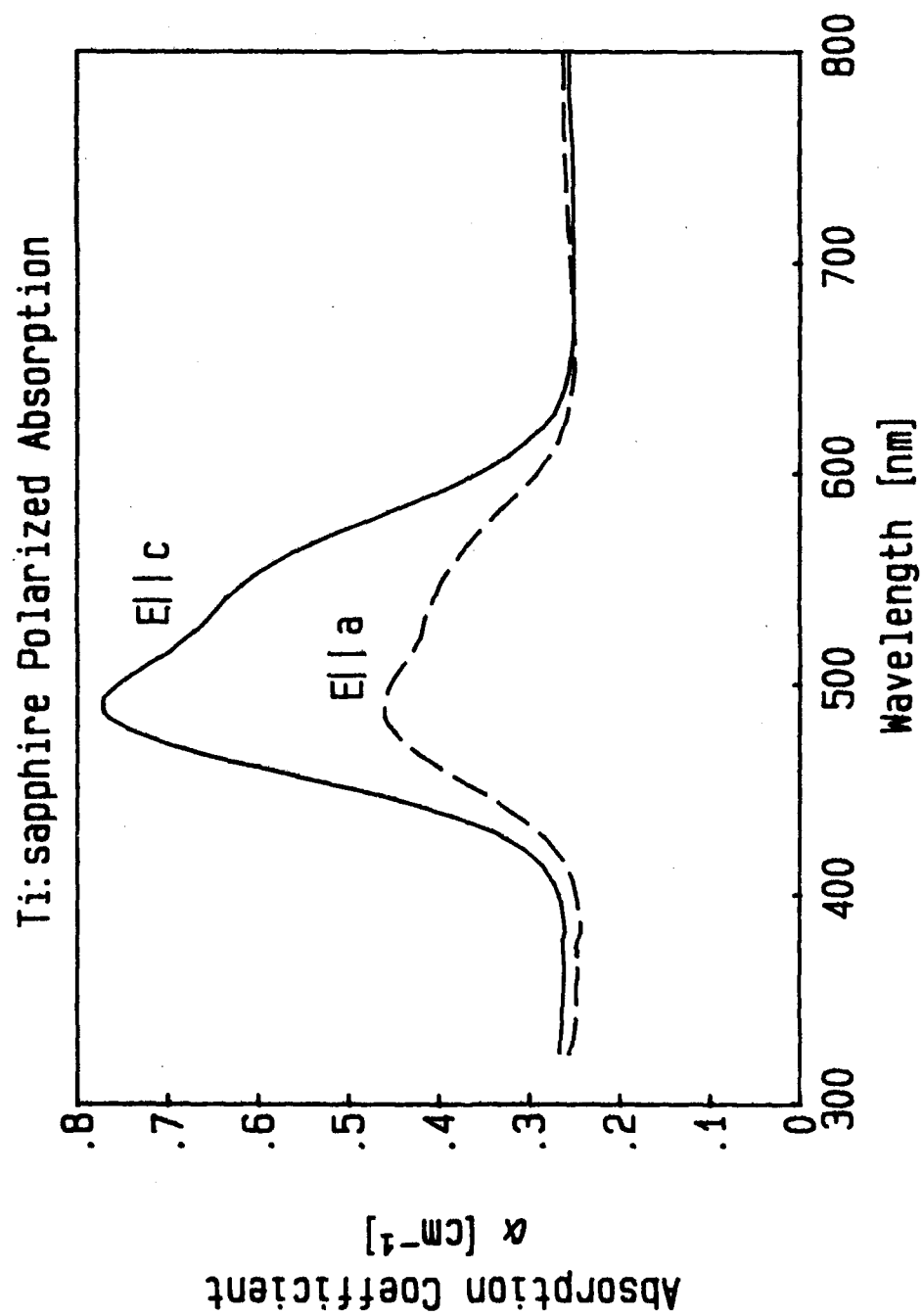


Figure 1. Polarized absorption spectra of Ti^{3+} :sapphire sample CS-H at room temperature.

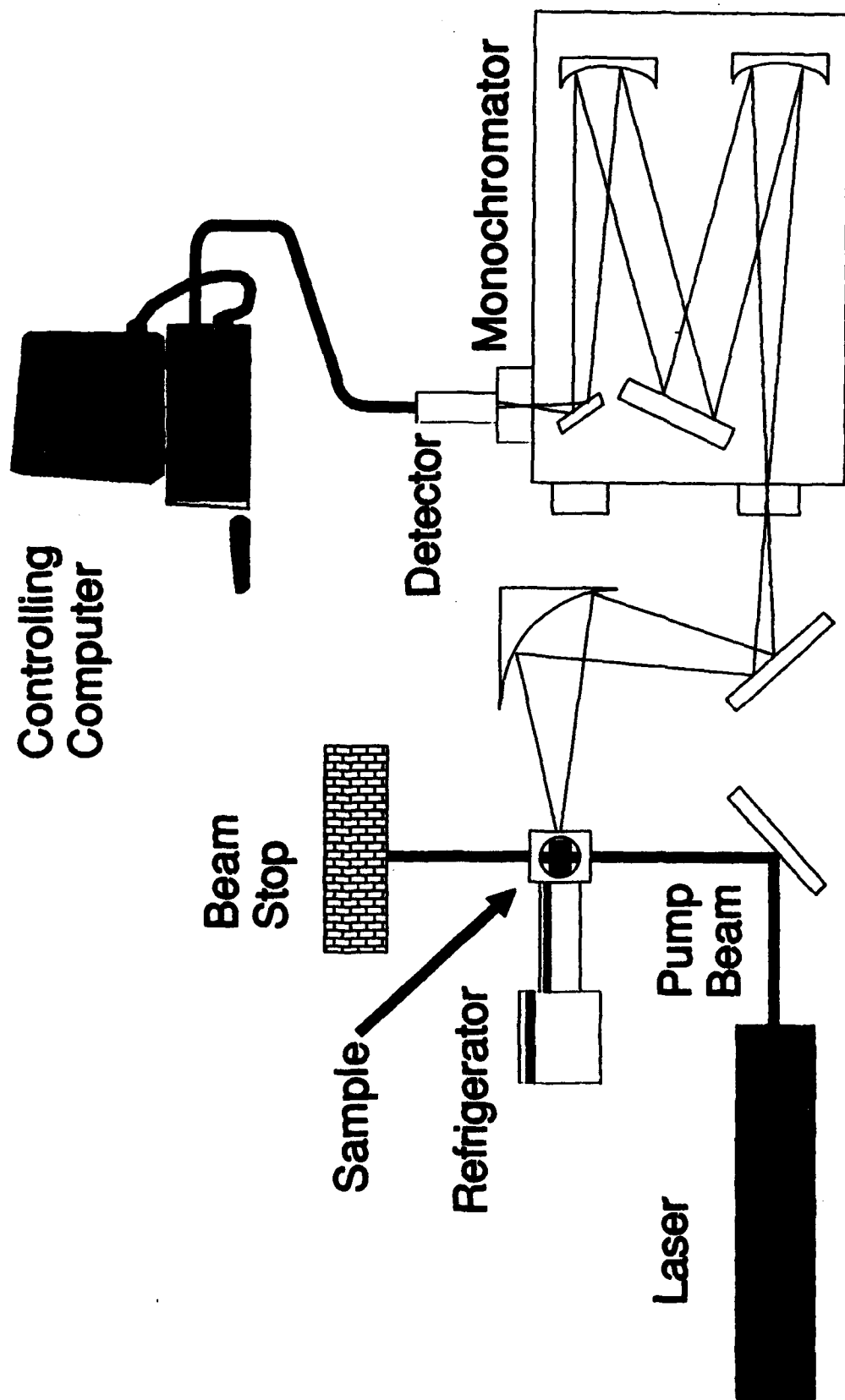


Figure 2. Diagram of the experimental arrangement to measure laser pumped fluorescence of temperature controlled samples.

Air Products closed cycle helium refrigerator which could set the temperature of a sample anywhere in the 10-400 K region to ± 0.1 K.

Figure 3 shows the observed fluorescence of a Ti:sapphire crystal at 11 K and 300 K. The sample was cw pumped with 200 mW of 488-nm argon laser output. No differences were observed when pumping at the other available argon laser lines other than changes in fluorescence intensity. The fluorescence spectra were extremely broad with emission observed throughout the 600-1050 nm region. A silicon detector was used to measure the complete spectrum since the photomultiplier usually used (Hamamatsu R928) was not sensitive beyond 850 nm. The relative fluorescence intensities for the a and c axis polarizations differed by a factor of 2.6 but the spectral shapes were quite similar. The fluorescence intensity decreased as temperature increased so the 300-K spectra have been multiplied by a factor of two to more easily compare them to the 11-K spectra.

The inset of Figure 3 is a plot of Ti:sapphire fluorescence on the short wavelength (high energy) side of the broadband emission at 11 K. A number of very sharp features are present. Two of these at 616.67 and 618.11 nm are interpreted as zero-phonon transitions between the lowest vibrational state of the upper metastable level and the ground-state triplet⁸. IR absorption measurements⁹ showed that the ground-state triplet is split in Ti:sapphire with the two higher levels separated from the lowest level by 37.8 cm^{-1} and 107.5 cm^{-1} . The two sharp features in the inset of Figure 3 are also separated by 38 cm^{-1} . The separation between the 616.67-nm peak and the small, broad peak at 621 nm corresponds to the 107.5 cm^{-1} splitting.

Figure 4 shows the half-maximum intensity positions of Ti:sapphire fluorescence spectra taken at several different temperatures. In general, the linewidth (full width at half maximum (FWHM)) increased with temperature but the increase occurred principally on the long wavelength side. In fact, above

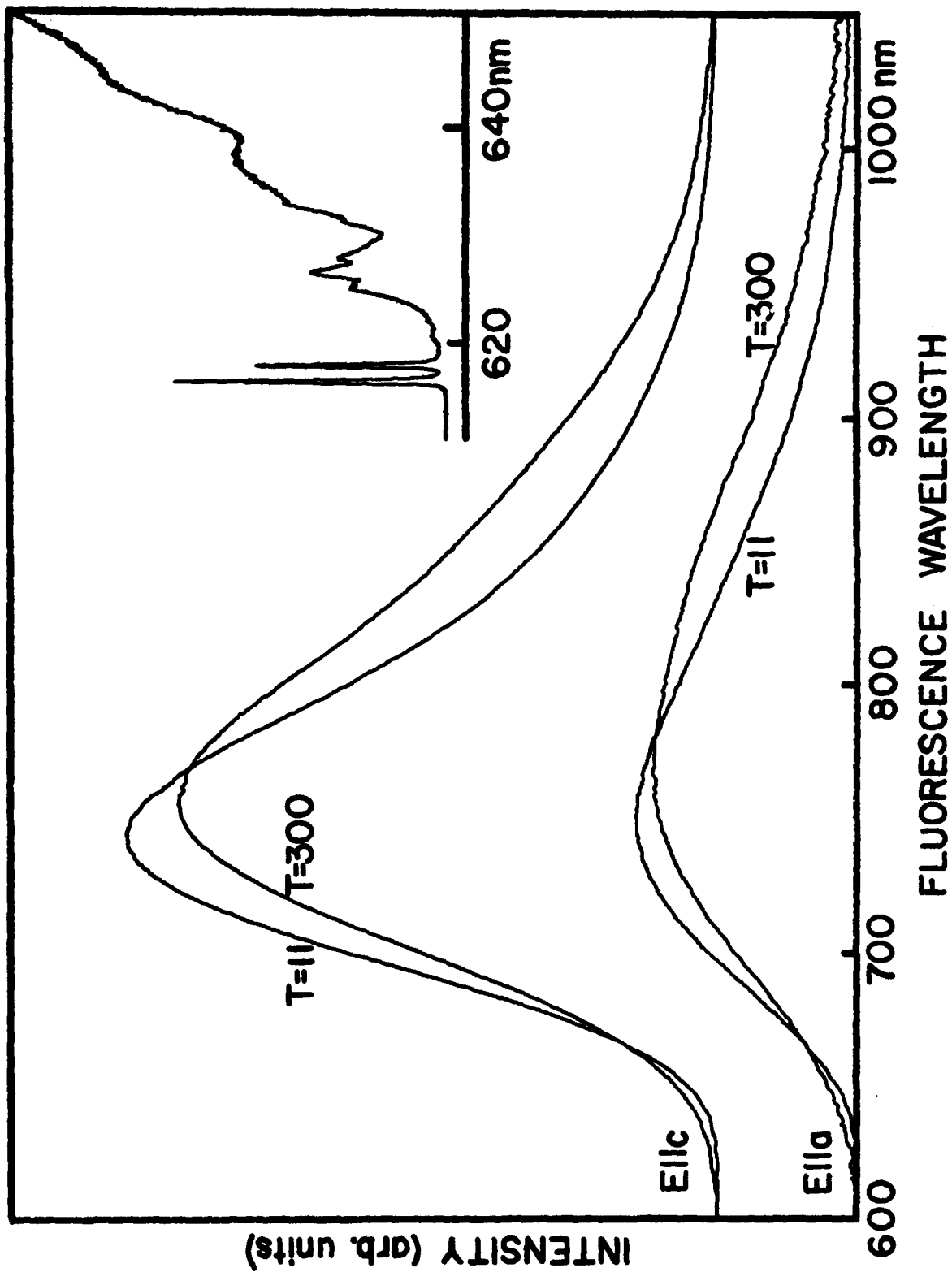


Figure 3. Polarized fluorescence of Ti^{3+} :sapphire at 11 and 300 K. The inset shows sharp zero-phonon features at 11 K.

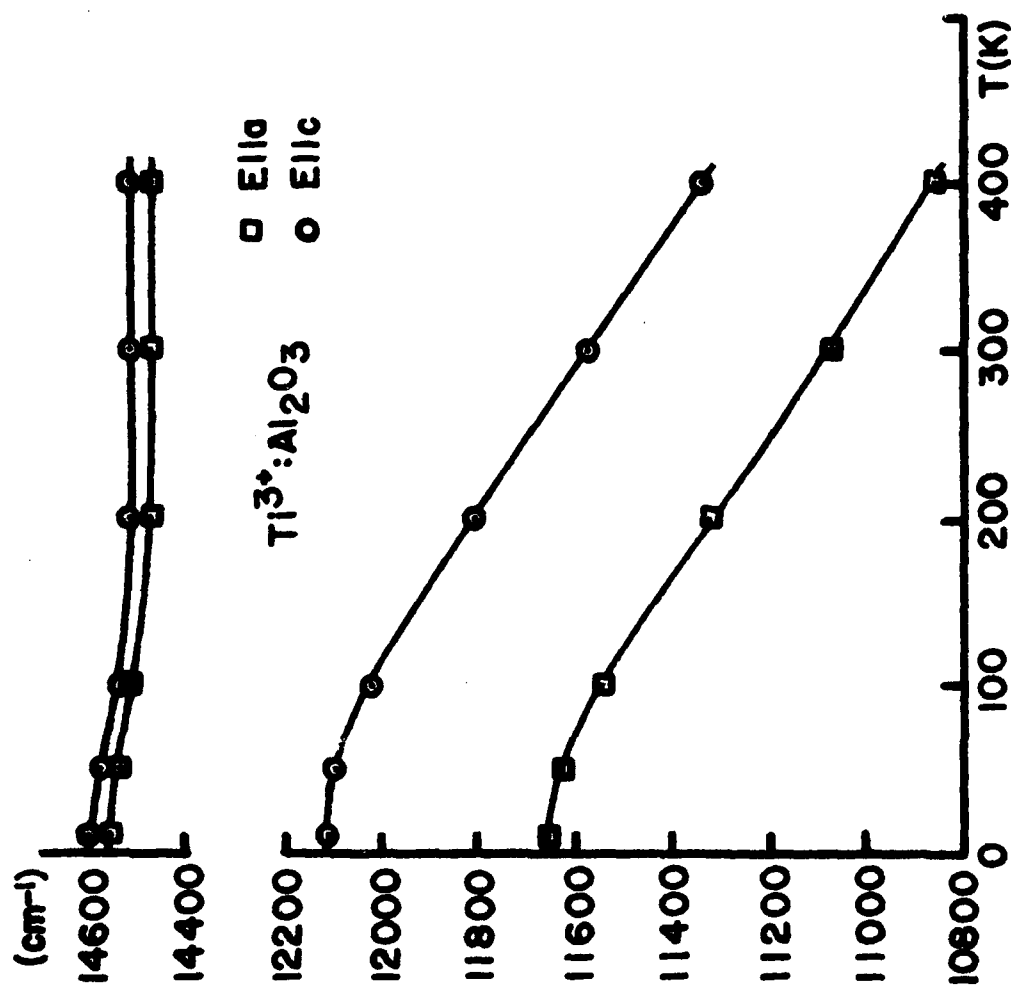


Figure 4. Half-maximum intensity positions of $\text{Ti}^{3+}:\text{sapphire}$ broadband fluorescence.

100 K the increase was nearly linear with temperature. The E11a fluorescence was slightly broader with most of the difference present on the long wavelength side.

Ti³⁺:sapphire Zero-Phonon Linewidth Measurements

The temperature dependence of the zero-phonon lines was also measured. Figures 5 and 6 are plots of FWHM vs. temperature of the two sharp zero-phonon lines using four different Ti:sapphire samples described in Table 1 above. Here R_1 is the higher energy zero-phonon line and R_2 is the lower energy zero-phonon line. Powell et al. have made similar measurements of linewidth dependence on temperature¹⁰. But there are some notable differences between this data and Powell's data. First of all, Powell et al. saw a linear change in linewidth as a function of temperature in the 20-60 K region but the linewidth increased nonlinearly in the same temperature region for all but the heavily doped R_1 line results in the measurements reported here. Also, the knee at 60 K in Powell's data is not present here.

The measured linewidth approached asymptotically at low temperatures ($\Delta\nu_0$) is expected to represent the inhomogeneous linewidth contributions due to microscopic strains in the lattice plus the homogeneous linewidth characteristic of the transition. The different samples were found to have different $\Delta\nu_0$'s indicating that they had different amounts of strain present. The Crystal Systems crystals had the least amount of inhomogeneous broadening and the heavily doped Union Carbide crystal had the most. Both the Ti³⁺ concentration and the growth method could affect the amount of broadening but determination of the relative magnitude of the two causes was not possible based on the limited amount of data available here.

Powell et al. described line broadening as a function of two contributions: (1) stimulated phonon emission or absorption between ground-state levels which is dominant at low temperatures

Ti:sapphire R-line Linewidths

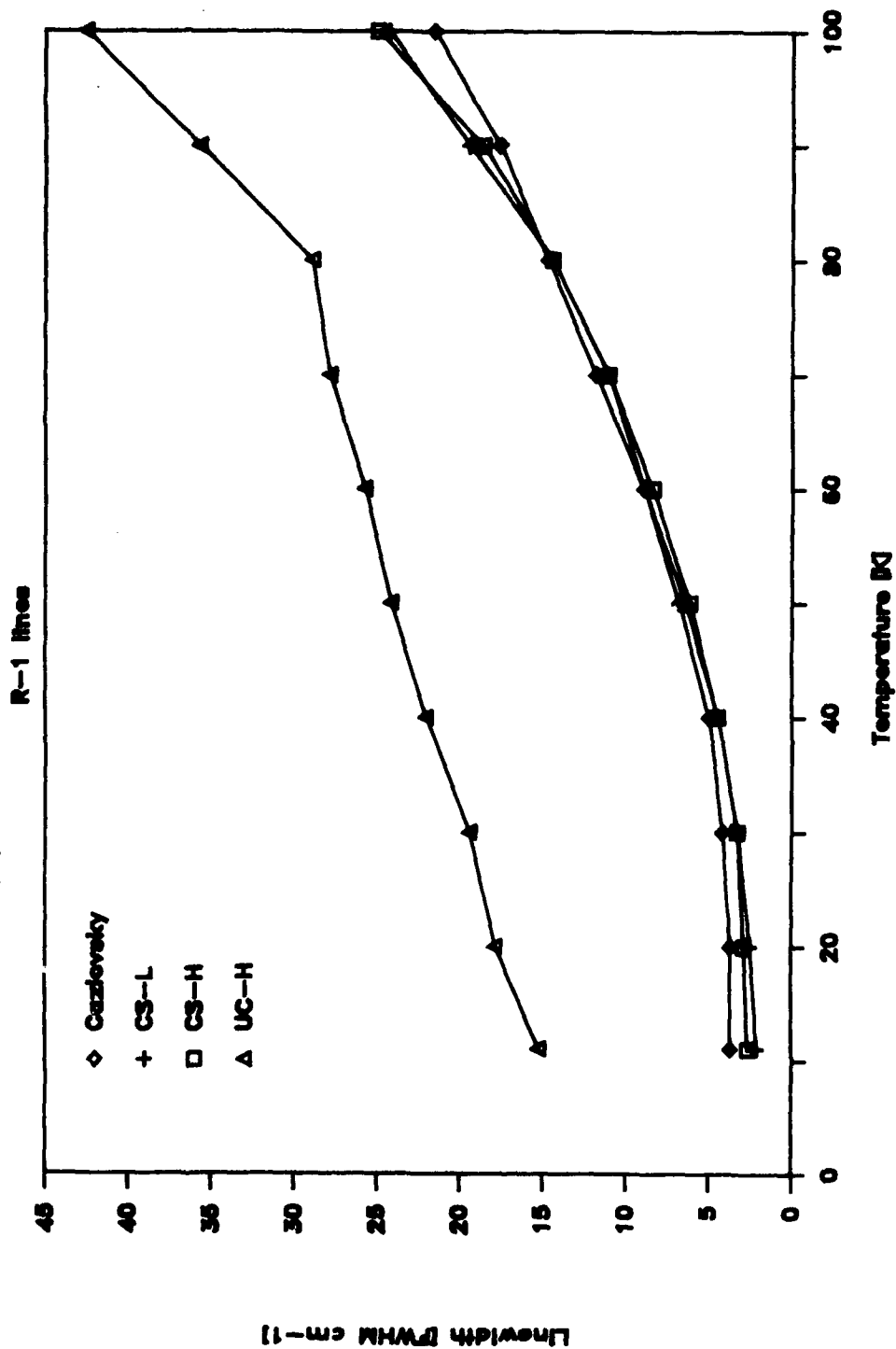


Figure 5. Linewidth of R_1 , the higher energy zero-phonon line, in four Ti^{3+} :sapphire samples.

Ti:sapphire R-line Linewidths

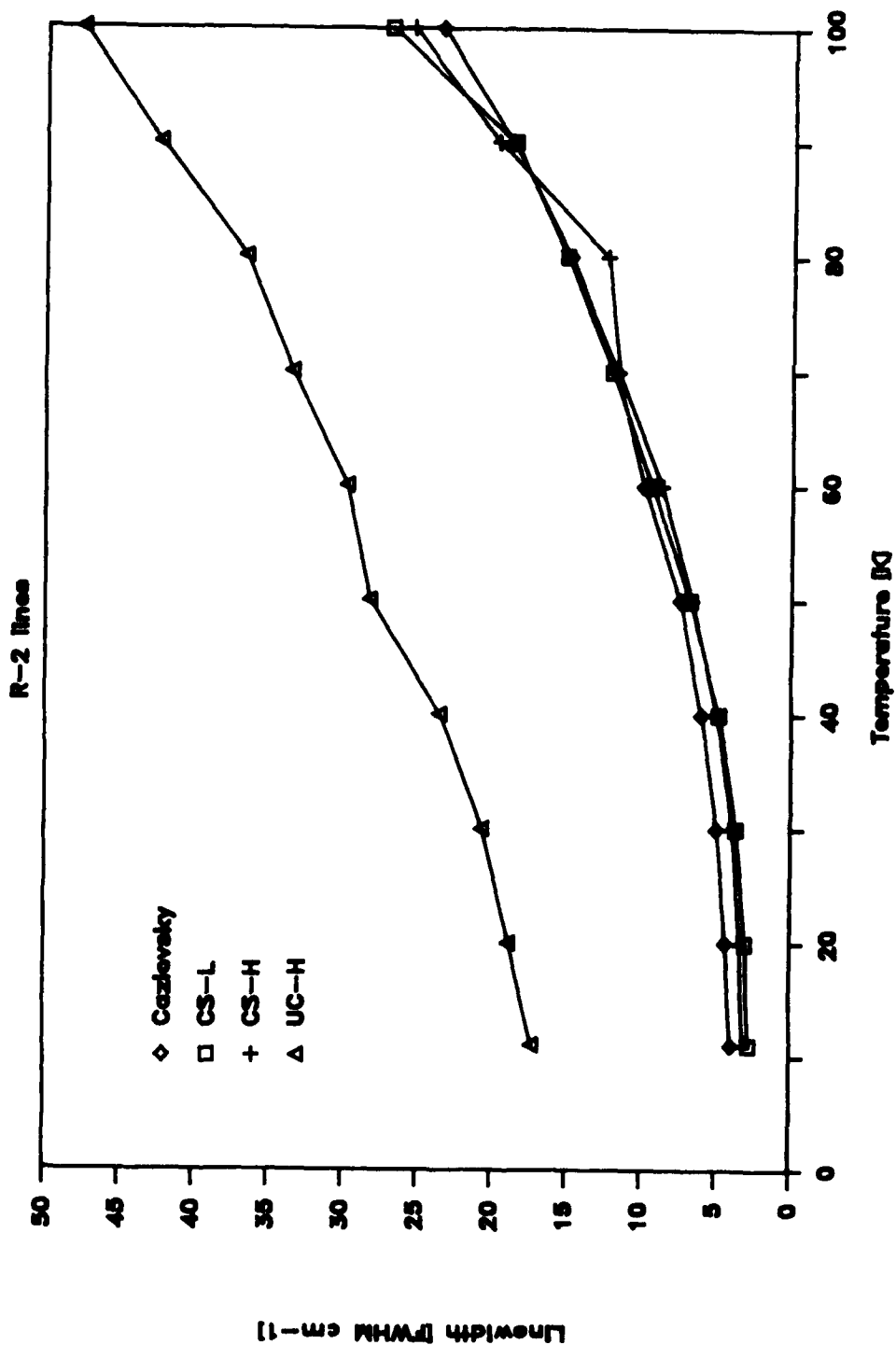


Figure 6. Linewidth of R₂, the lower energy zero-phonon line, in four Ti³⁺:sapphire samples.

and (2) two-phonon Raman scattering with a T^7 temperature dependence dominant at high temperatures. The linewidth as a function of temperature can be written as:

$$\Delta\nu = \Delta\nu_0 + K_1[\exp(\Delta E/kT)-1]^{-1} + K_2T^7 \quad [1.1]$$

where $\Delta\nu_0$ is the inhomogeneous linewidth, K_1 is an electron-phonon coupling parameter, K_2 is the two-phonon Raman scattering constant, ΔE is the energy separation of R_1 and R_2 , k is the Boltzmann constant and T is temperature. Using ΔE as 38 cm^{-1} , $\Delta\nu_0$, K_1 and K_2 can be fit to the data. An example of such a fit is shown in Figure 7. Agreement with experiment is reasonably good.

Figure 8 shows integrated intensity of the R_1 line as a function of temperature for the four Ti:sapphire samples. All show an approximately linear decrease in intensity with increasing temperature. The large scatter in the data is probably due to the difficulty in correctly subtracting the background emission of the short wavelength tail of the broadband peak.

Fluorescence Lifetime

Ti:sapphire fluorescence lifetime was measured as a function of temperature. Samples were pumped with Q-switched pulses from a frequency doubled Quantel Nd:YAG laser. The 532-nm pulses were 10 ns in duration. The fluorescence passed through a 0.5-m Jarrell-Ash monochromator and was detected by an S-1 photomultiplier tube (PMT). The PMT output was, in turn, measured with a LeCroy 3500SA transient digitizer. The input impedance of the LeCroy input was 50 Ω but that made the PMT signal too small to measure. The problem was remedied by using a Tektronix 468 oscilloscope amplifier and a variable load switch. The amplifier had a 50- Ω output impedance which matched the

Ti:sapphire R₁ Linewidth
Sample CS-H

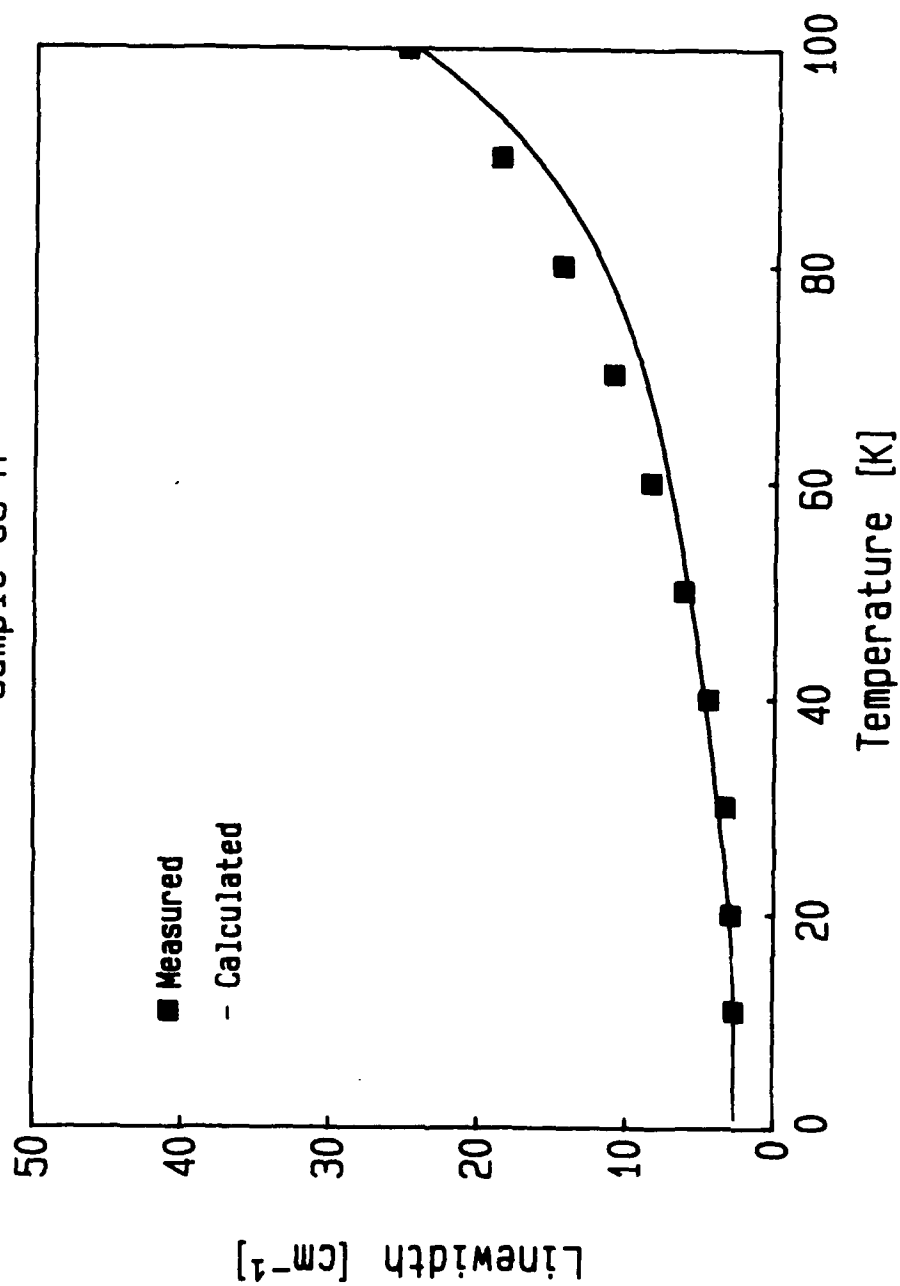


Figure 7. Fit of a theoretical linewidth model to experimental data.

Ti:sapphire R-line Intensities

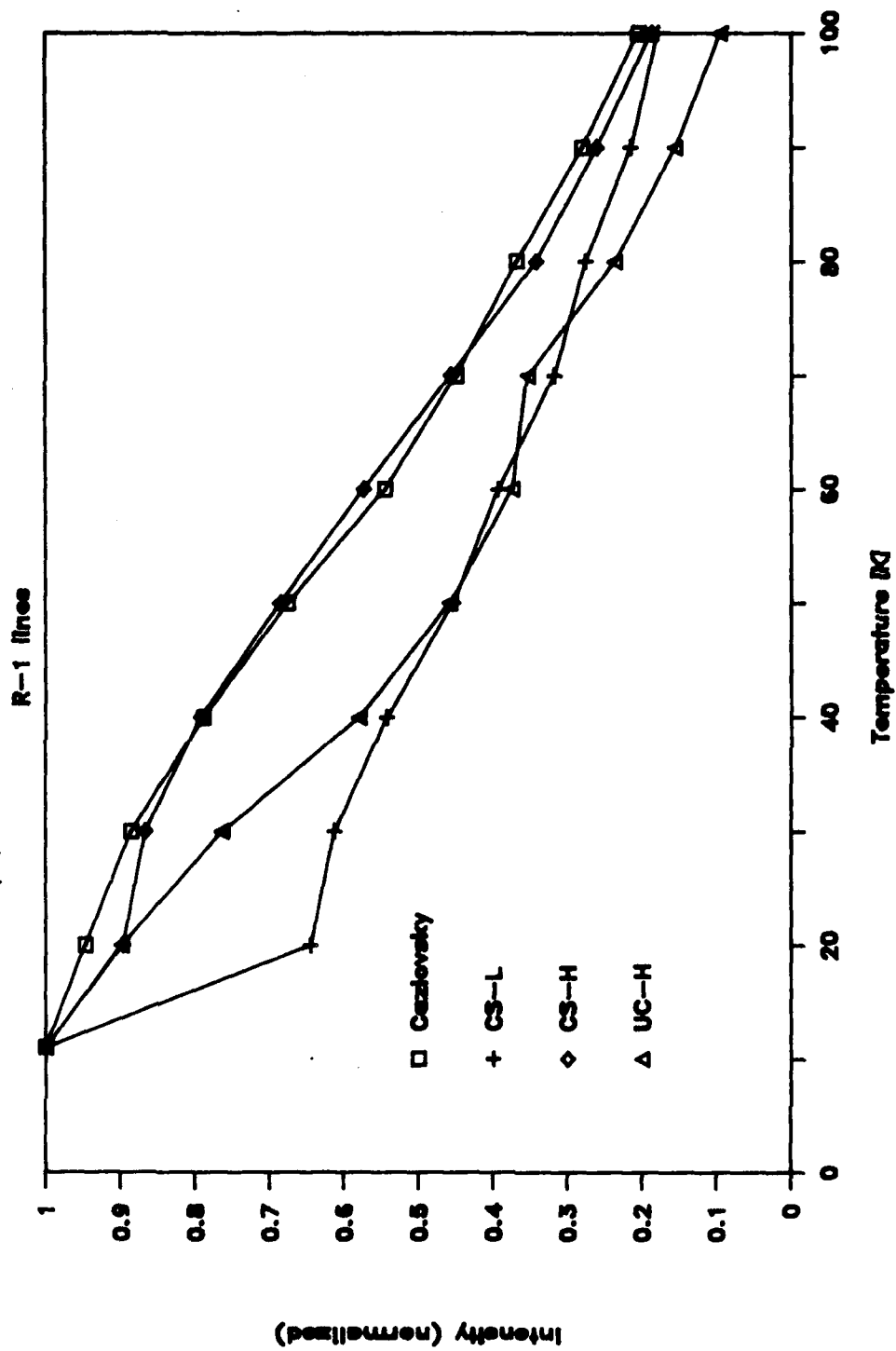


Figure 8. Integrated intensity of Ti^{3+} :sapphire R₁ line fluorescence.

LeCroy input impedance. Then the load switch was inserted at the oscilloscope amplifier input. The load switch was adjusted to achieve maximum signal without distorting the time dependence of the signal. Making the input load too large caused the RC time constant of the input circuit to become larger than the fluorescence lifetime yielding a lifetime longer than the true one.

A plot of fluorescence intensity versus time for sample CS-H is shown in Figure 9. Each data point represents the summed output of 1000 shots with the PMT baseline signal subtracted out. The large noise oscillations at the start of the pulse are due to pump laser electromagnetic interference. Lifetimes were determined by calculating a least squares fit to the natural log of the signal intensity vs. time. After the excitation pulse the Ti^{3+} ions are expected to relax back to their ground-state with a single exponential decay, i.e.

$$I(t) = I_0 \exp(-t/\tau) . \quad [1.2]$$

Taking the natural log of both sides yields

$$\ln (I(t)) = -t/\tau + \ln (I_0) \quad [1.3]$$

which is the same as the equation for a straight line:

$$y = m \cdot x + b . \quad [1.4]$$

Figure 10 is a log plot of the same data and the linearity of the plot shows that the fluorescence decay is well represented by a single exponential. In fact, none of the Ti:sapphire crystals investigated showed any significant variation from single exponential decay.

Figure 11 is a plot of lifetime as a function temperature for Ti:sapphire. The lifetime remained constant at about 4.3 μs below 250 K. But at higher temperatures the lifetime began to

Ti:sapphire Fluorescence

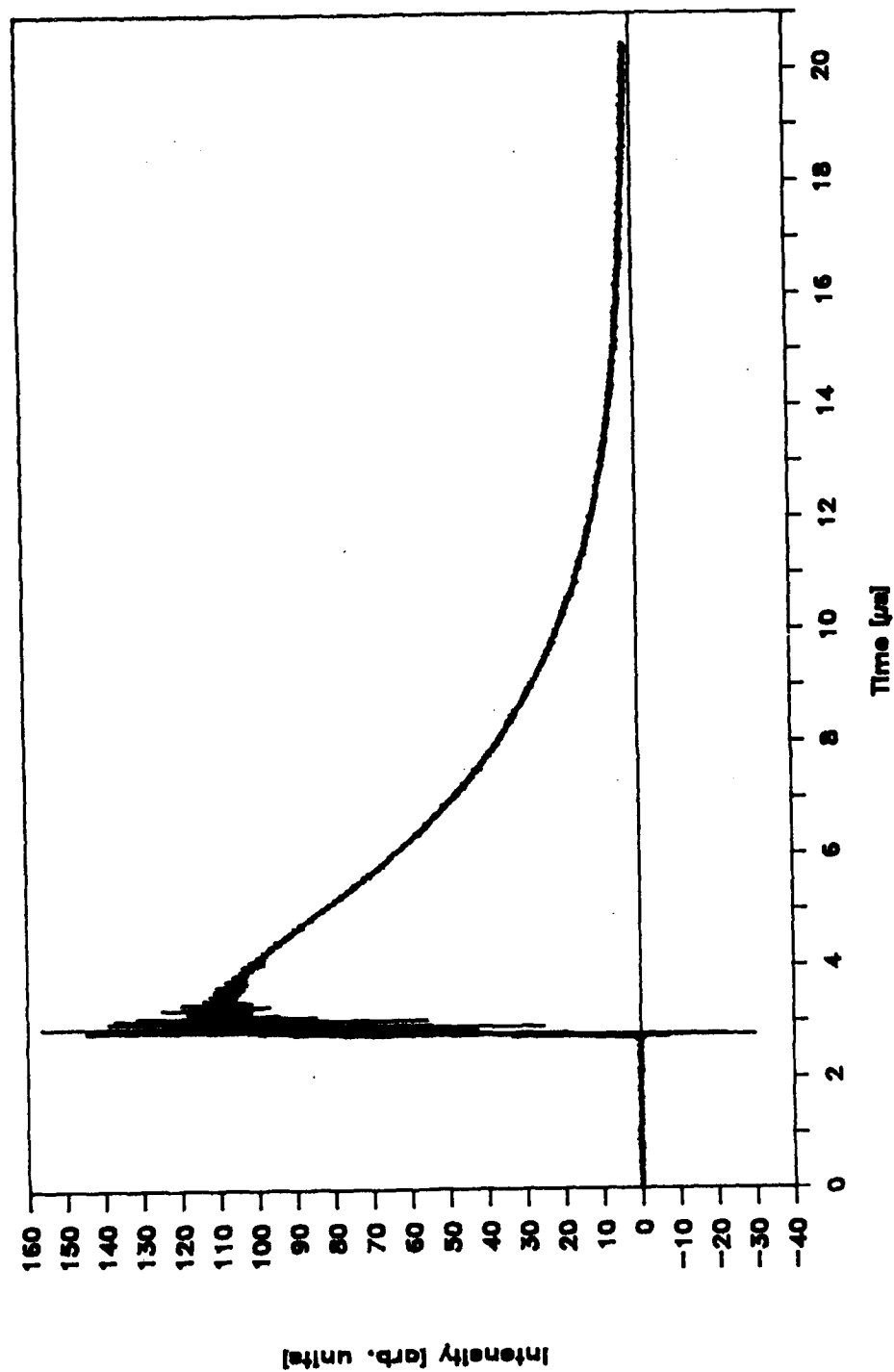


Figure 9. Time dependence of Ti^{3+} :sapphire fluorescence when pumped by 532 nm, 10 ns pulses at room temperature. The large noise spikes at the beginning of the pulse are due to electromagnetic interference from the pump laser.

Ti:sapphire Fluorescence

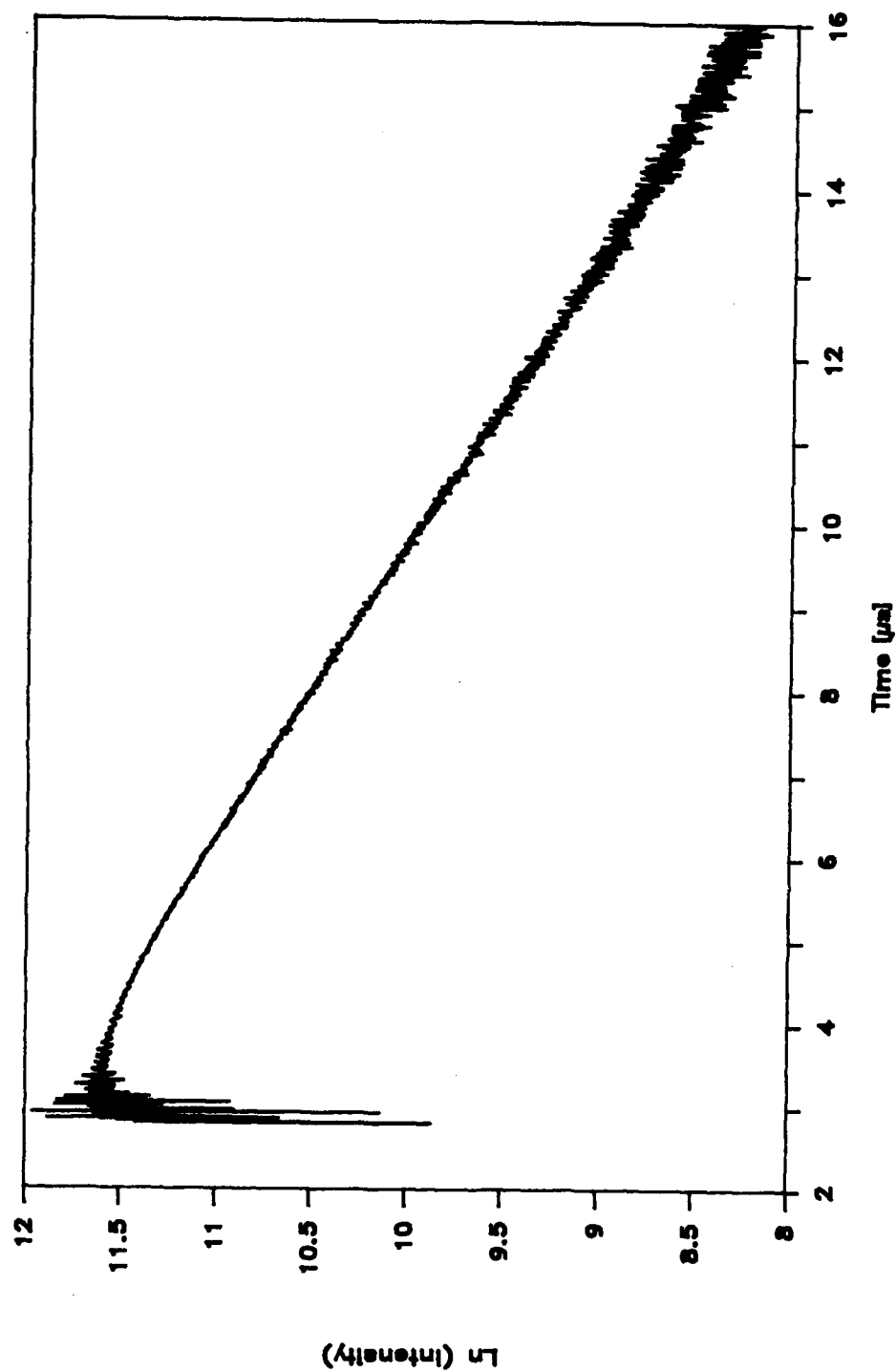


Figure 10. Logarithmic plot of the Ti^{3+} :sapphire fluorescence data shown in Figure 9.

Ti:sapphire Fluorescence Lifetime

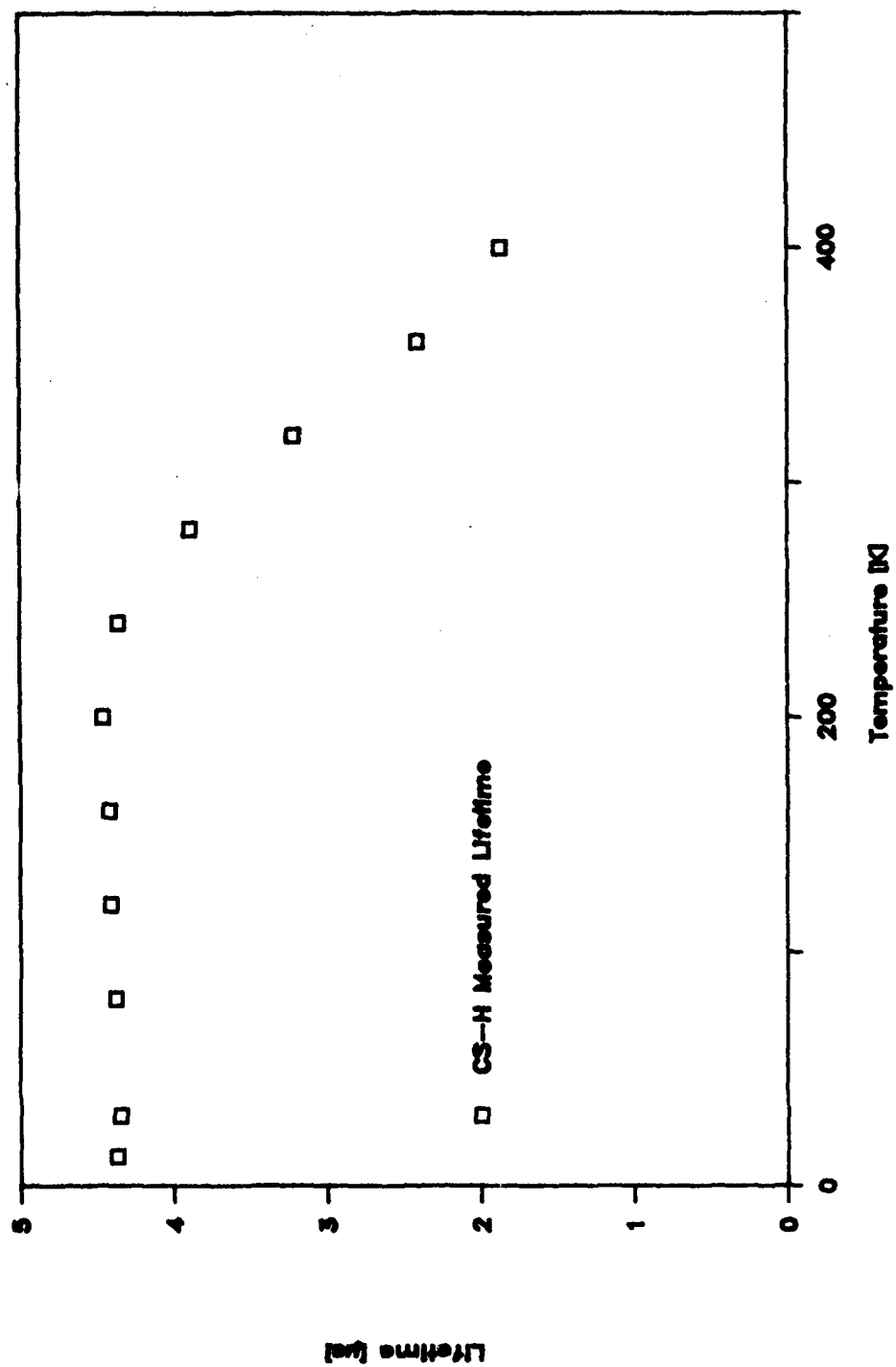


Figure 11. Ti³⁺:sapphire lifetime as a function of temperature.

decrease. This behavior indicates that another relaxation path became available when temperature rose above 250 K.

Quantum Efficiency

Figure 3 has already shown that Ti:sapphire fluorescence decreases with increasing temperature. The intensity of the cw pumped fluorescence integrated over wavelength and polarization is proportional to the radiative relaxation rate. Since absorption does not change significantly with temperature, the integrated intensity is proportional to the quantum efficiency. Also, assuming the quantum efficiency at $T = 10$ K is 100% then

$$\eta(T) = \frac{\sum_p \int I_p(\lambda, T) d\lambda}{\sum_p \int I_p(\lambda, 10) d\lambda} \quad [1.5]$$

Figure 12 is a plot of equation 1.5 and shows how the quantum efficiency begins to decrease significantly as the temperature rises above 250 K. Nonradiative relaxation begins to occur and becomes quite pronounced at 400 K. Mechanisms for such a phenomenon will be discussed below in Section 4.

Ti:sapphire Fluorescence Intensity

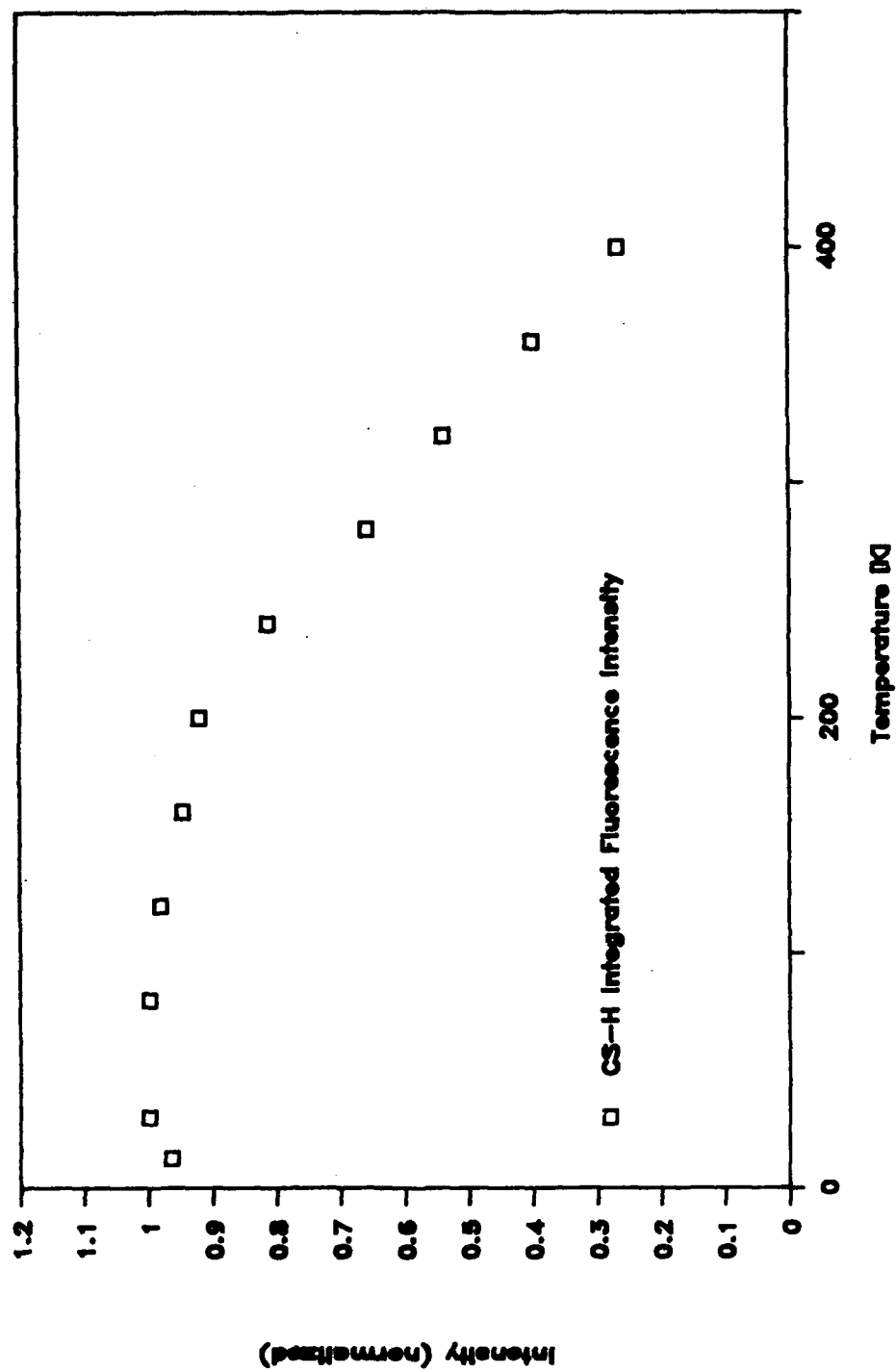


Figure 12. Ti³⁺:sapphire integrated fluorescence intensity.

SECTION 2

Other Ti^{3+} Doped Materials

Ti^{3+} ions in sapphire are capable of lasing over a broadband, continuously tunable wavelength range. Since it is the d electron of the Ti^{3+} ion interacting with the host lattice which provides tunability, the possibility of doping other hosts deserves consideration. Other hosts will provide different crystal fields which may change spectroscopic characteristics of the Ti^{3+} ions such as absorption bands, fluorescence bands, and fluorescence lifetime. For this reason several new host materials doped with Ti^{3+} ions were investigated.

$Ti^{3+}:YAlO_3$

In contrast to the rhombohedral symmetry of sapphire (Al_2O_3), $YAlO_3$ has orthorhombic symmetry. Therefore $YAlO_3$ has three distinct crystal axes (a, b, and c) rather than just two (a and c). Also, the site symmetry at the Al^{3+} site (where Ti^{3+} ions will substitute) is C_1 in $YAlO_3$ rather than C_{3v} in sapphire. The inversion symmetry in $YAlO_3$ should result in a longer Ti^{3+} radiative lifetime since electric dipole transitions are forbidden for this symmetry.

Samples of $Ti^{3+}:YAlO_3$ grown at Airtron and MIT Lincoln Lab were cut and polished for spectroscopic measurements. The absorption spectrum of Figure 13 (Airtron sample 2.5 cm long) shows $Ti^{3+}:YAlO_3$ to have a two peak absorption similar to Ti^{3+} :sapphire but at shorter wavelengths. Also, the absorption did not significantly depend on field orientation as it did in sapphire. The shift of the peaks to shorter wavelengths indicates that the crystal field in $YAlO_3$ is larger than it is in

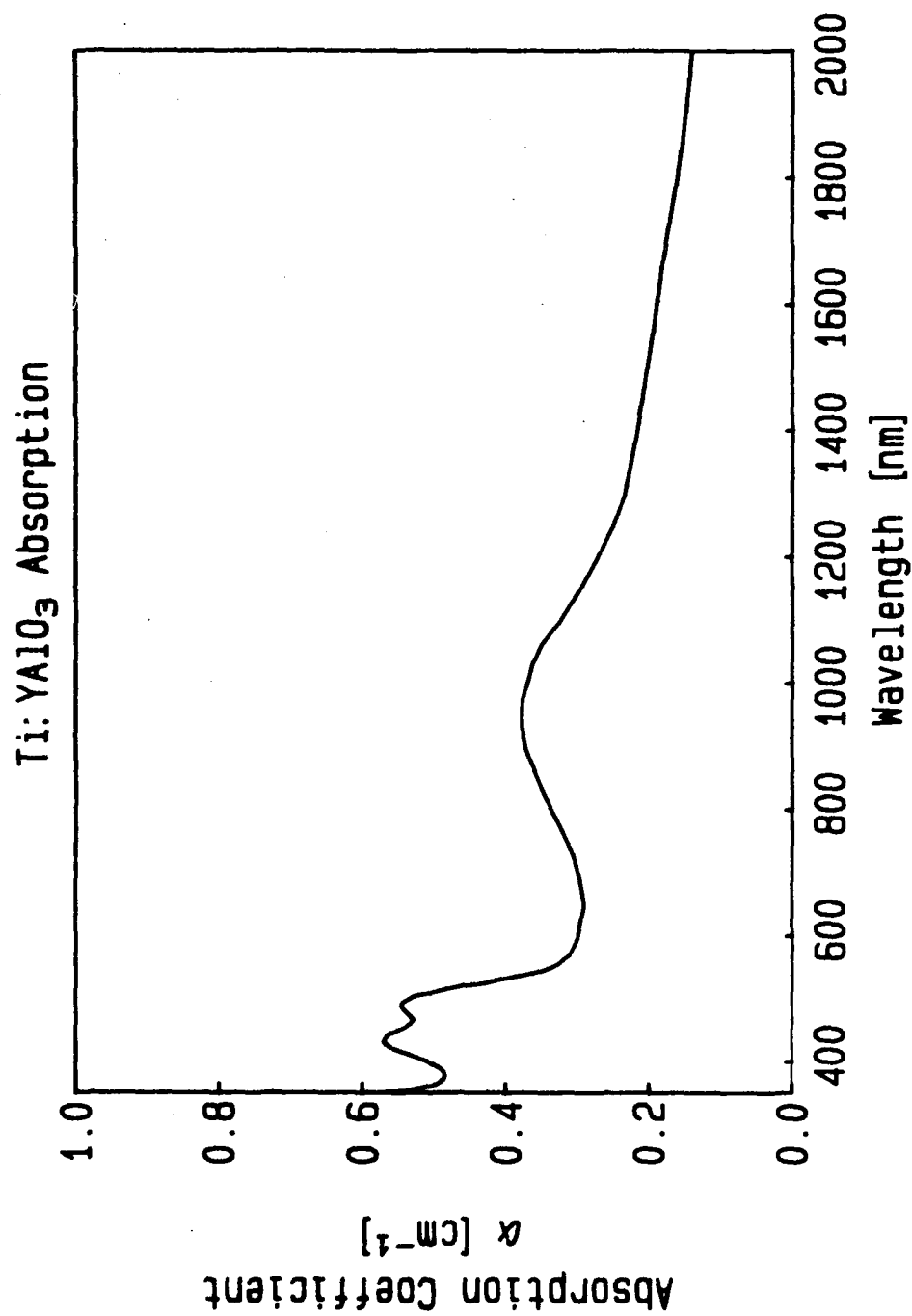


Figure 13. Ti³⁺:YAlO₃ absorption at room temperature.

Ti:sapphire. This differs from the behavior of Cr^{3+} ions in Al_2O_3 and YAlO_3 ¹¹ where the absorption peaks were at similar wavelengths in the two materials. The broadband peak, centered near 900 nm, appears to be similar to the Ti^{3+} - Ti^{4+} pair absorption observed in sapphire but much larger. The long sloping baseline is probably related to the large scattering loss in this sample which was easily observed when transmitting a HeNe laser beam through the sample.

The polarized fluorescence spectra of $\text{Ti}:\text{YAlO}_3$ shown in Figure 14 were also shifted to shorter wavelengths. In contrast to Ti^{3+} :sapphire, the three $\text{Ti}^{3+}:\text{YAlO}_3$ crystal axes differed only slightly in fluorescence intensity, peak position, and bandwidth; i.e., the distortion from cubic symmetry is small in $\text{Ti}^{3+}:\text{YAlO}_3$. Peak wavelengths for E11a, E11b, and E11c were 602, 613 and 610 nm at 11 K. Only one clearly identifiable zero-phonon line at 540 nm was observed in $\text{Ti}:\text{YAlO}_3$ at low temperatures (see inset of Figure 14a). The weaker lines near 545 nm could be the other two zero-phonon lines or they could also be single-phonon emission. If the splitting of the triply degenerate ${}^2\text{T}_2$ ground state is less than the zero-phonon linewidth then only one zero-phonon line would be seen. The linewidth of the 540-nm line as a function of temperature was similar to that observed for sapphire. But the $\text{Ti}^{3+}:\text{YAlO}_3$ 540-nm line was very broad; the linewidth was similar in magnitude to UC-H, the heavily doped sapphire sample. The lines near 545 nm could not be observed above 20 K because of the rapid growth and shift of the broadband emission to shorter wavelengths with increasing temperature.

A comparison of the $\text{Ti}^{3+}:\text{YAlO}_3$ fluorescence at 11 K (Figure 14a and 300 K (Figure 14b) shows that the broadband emission does increase with temperature. Locations of the half-maximum positions for all three crystal axes are shown in Figure 15. Linewidth [FWHM] of the broadband fluorescence vs. temperature for each of the polarizations of the $\text{Ti}^{3+}:\text{YAlO}_3$ sample is shown in Figure 16. As in sapphire, the short

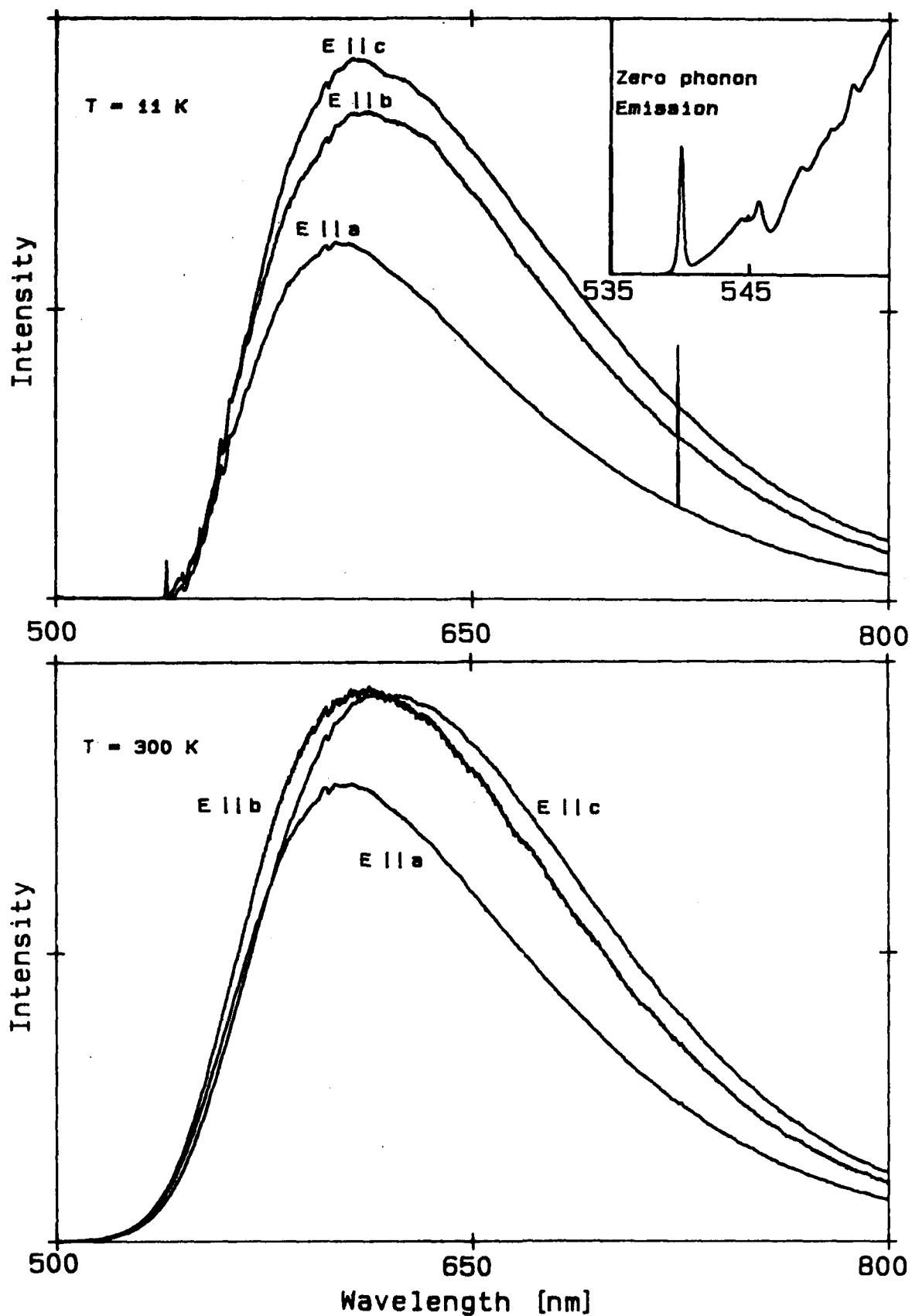


Figure 14. Polarized $\text{Ti}^{3+}:\text{YAlO}_3$ fluorescence (a) at 11 K and (b) at 300 K. Zero-phonon emission at 540 nm is shown in the inset.

Ti:YAlO Linewidth

FWHM Positions

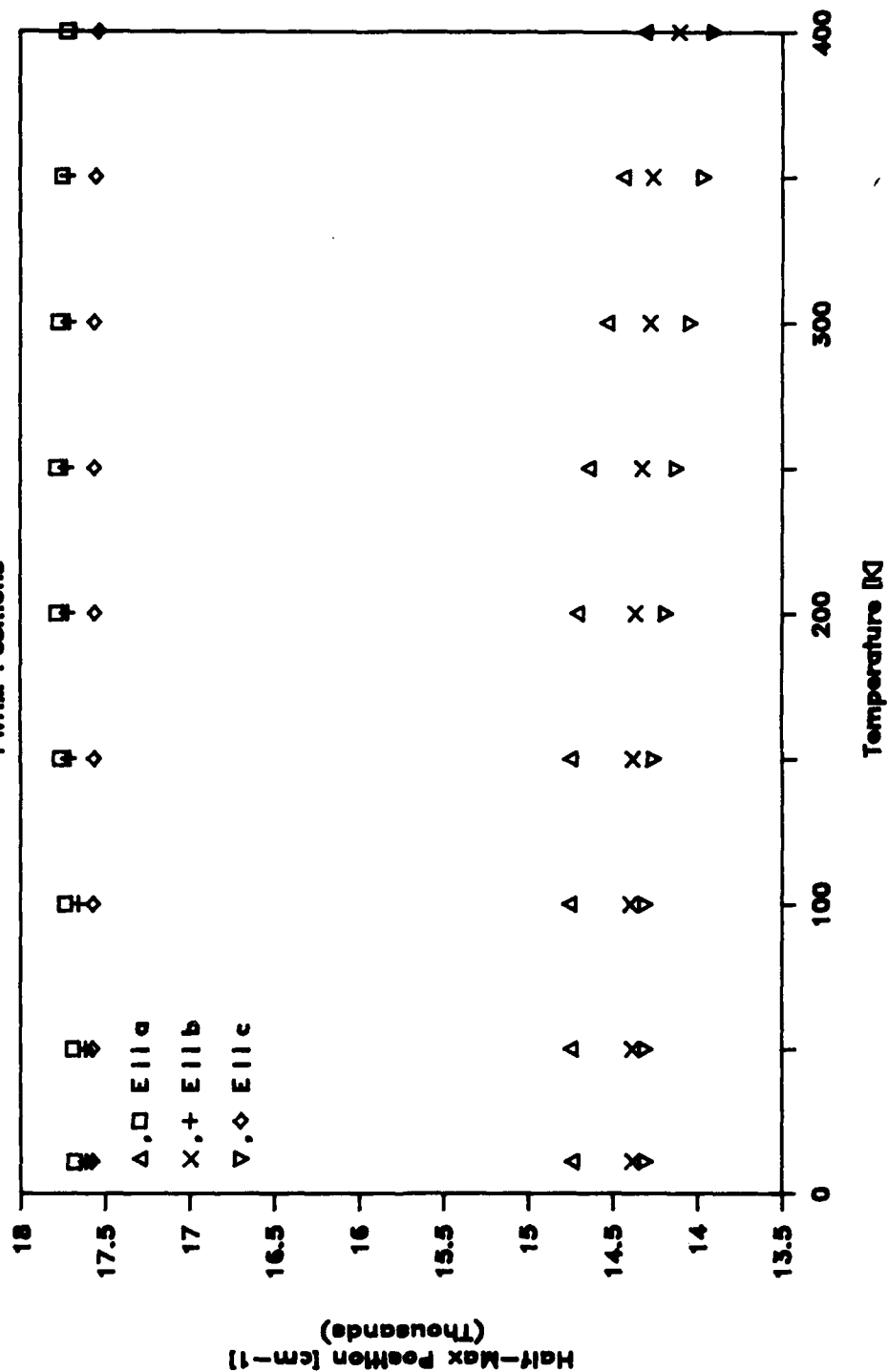


Figure 15. Half-maximum intensity positions of $\text{Ti}^{3+}:\text{YAlO}_3$ broadband fluorescence.

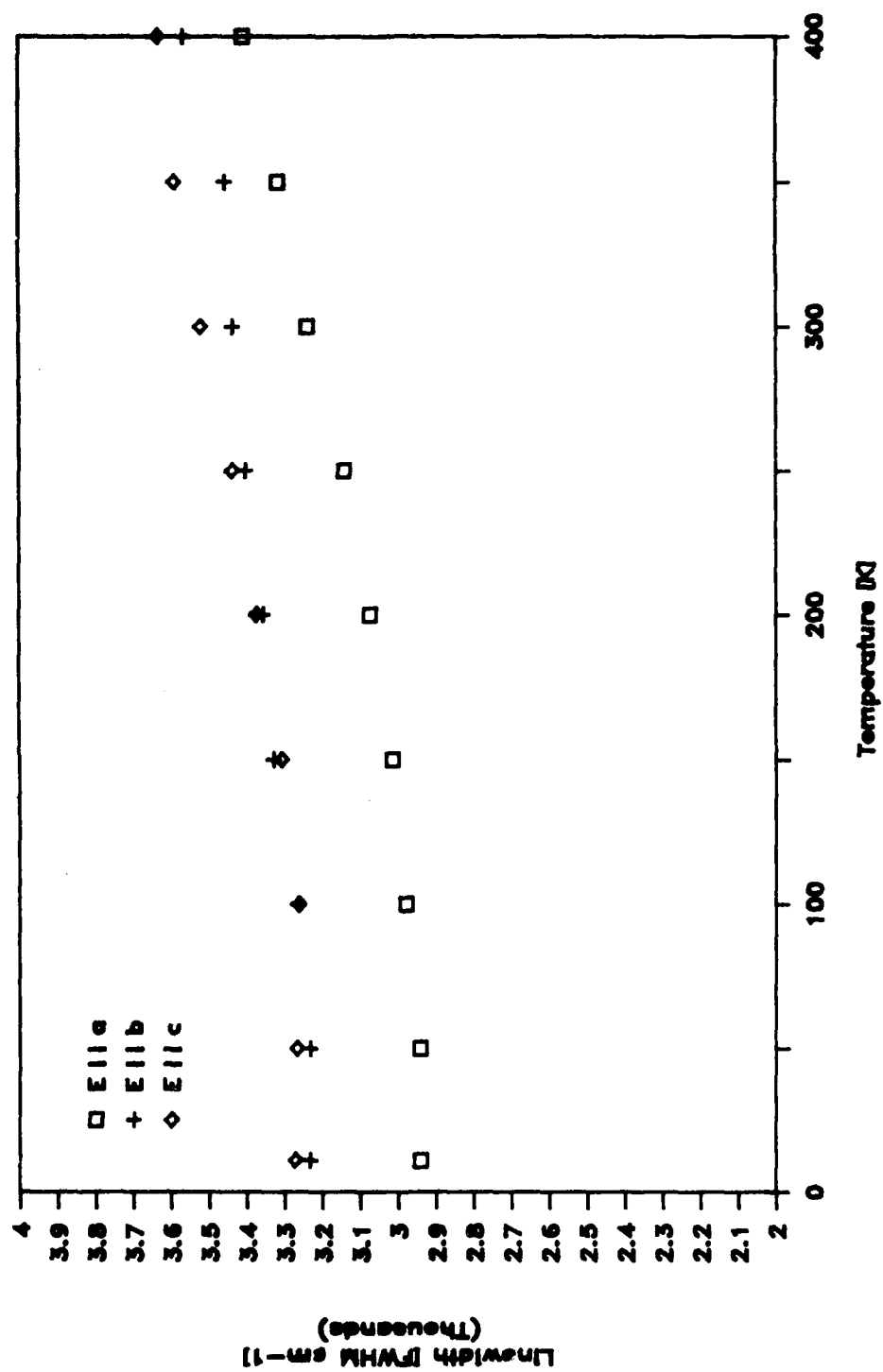


Figure 16. $\text{Ti}^{3+}:\text{YAlO}_3$ broadband fluorescence linewidth.

wavelength half-maximum position changed little and the long wavelength half-maximum position increased with temperature.

Fluorescence lifetime measurements (see Figure 17) were recorded in the same manner as the Ti:sapphire measurements. They show that Ti:YAlO₃ has a longer lifetime and that although lifetime does decrease with temperature it does not display the dramatic drop with temperature that is observed with Ti:sapphire. In addition, integrated fluorescence intensity (also shown in Figure 17) does not change significantly with temperature in Ti:YAlO₃ until the temperature is above room temperature. This may indicate that Ti:YAlO₃ quantum efficiency remains near unity even at elevated temperatures. The larger crystal field in Ti:YAlO₃ appears to prevent nonradiative loss.

Attempts to observe lasing of Ti:YAlO₃ in a collaborative effort with MIT Lincoln Lab¹² and by others¹³ were unsuccessful. In fact, Moulton noticed net loss when a sample was pumped by an argon ion laser. Two crystals of Ti³⁺:YAlO₃ grown by Litton Airtron were examined here in a single pass gain experiment to confirm Moulton's results. A focused argon ion beam of up to 2 W was chopped at 10 Hz and directed into a 2.5 cm long Ti³⁺:YAlO₃ crystal. At the same time a HeNe probe beam at 632.8 nm was colinearly focused into the sample and detected with a silicon detector (See Figure 18).

Even before application of the pump beam, the probe beam was attenuated more than the expected reflection losses indicating that scattering and ground-state absorption were present; this confirms the interpretation of the absorption spectrum data of Figure 13. In contrast to Ti:sapphire, annealing experiments at MIT Lincoln Labs were not able to significantly reduce the size of this peak.

The time dependence of the probe signal was a complicated function of time and pump power. The observed changes in signal did not have lifetimes characteristic of the Ti³⁺ fluorescence lifetime. Rather, most effects occurred in time intervals

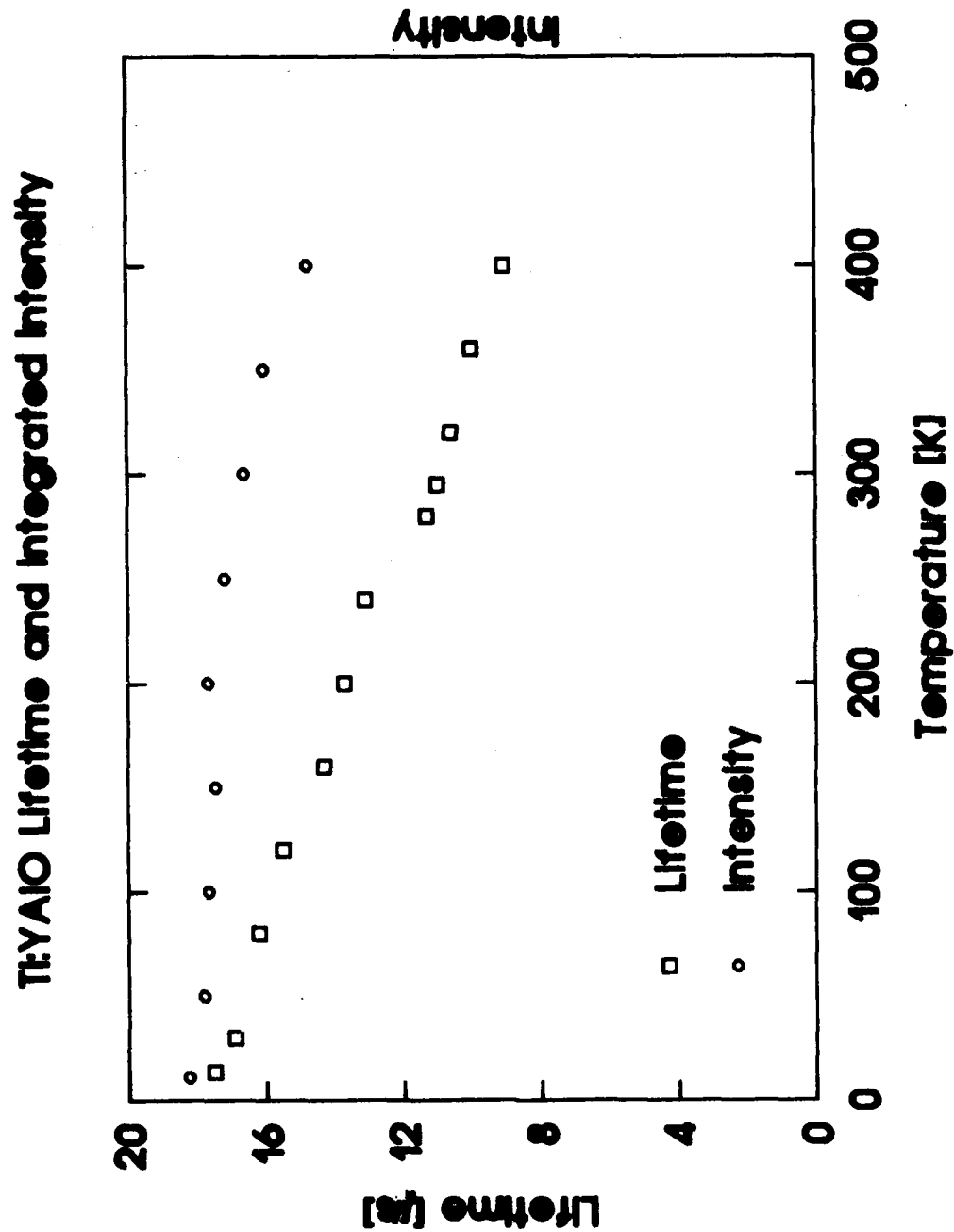


Figure 17. Ti³⁺:YAlO₃ fluorescence lifetime and integrated intensity vs. temperature.

Single Pass Gain Experiment

Ti:YAlO₃

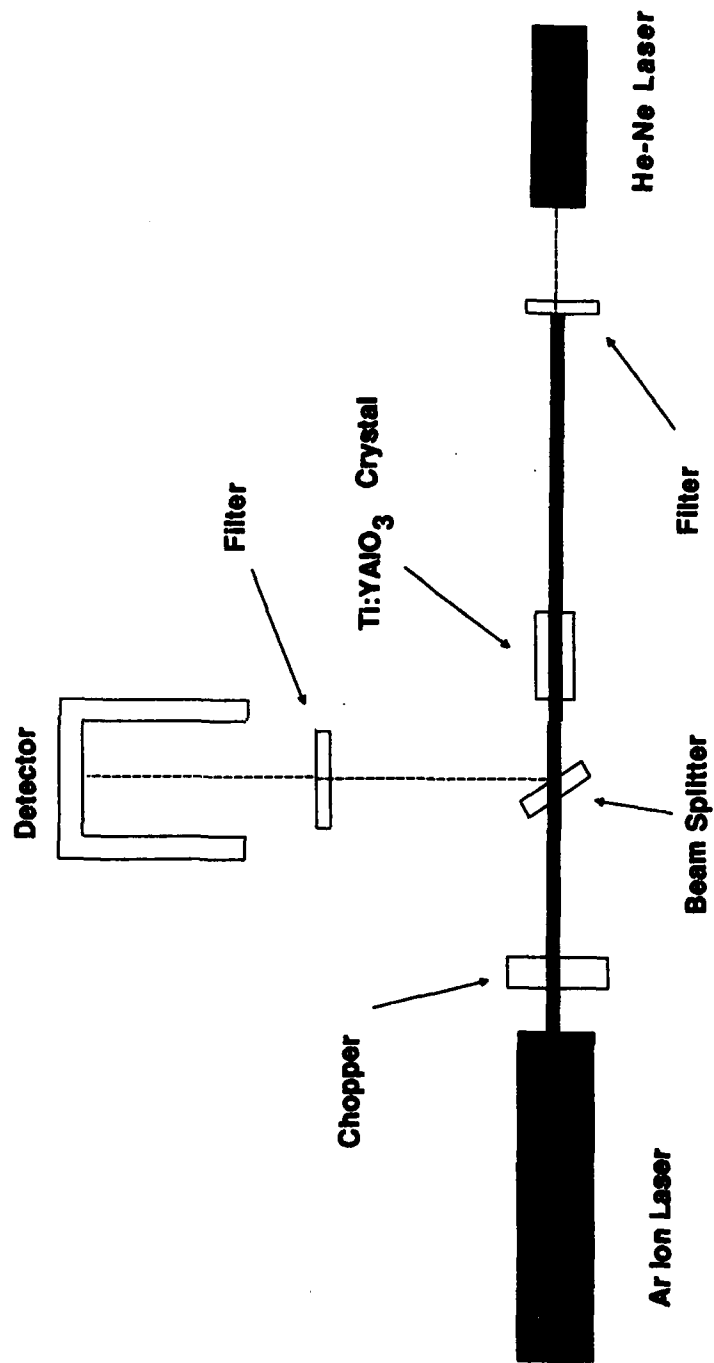


Figure 18. Experimental arrangement to measure single-pass gain in Ti₃₊:YAlO₃.

greater than 1 ms with some effects taking minutes to appear. Both increases and decreases in probe beam transmission were observed. Such effects are typically attributed to color centers which are being created and destroyed by the pump beam.

Efficient lasing of $\text{Ti}^{3+}:\text{YAlO}_3$ will require further development of the growth technique. Color centers were also a problem with early growth of $\text{Nd}^{3+}:\text{YAlO}_3$ so the problem was solved in a related case. Growth in a controlled atmosphere, nitrogen or reducing, has been suggested as a possible solution. Recently, stimulated emission from a thin plate (3.5 mm) of $\text{Ti}:\text{YAlO}_3$ was reported by Perner¹⁴ so with further work to reduce the anomalous absorption, efficient lasing should be possible.

$\text{Ti}^{3+}:\text{YAG}$

Two samples of Ti^{3+} doped yttrium aluminum garnet (YAG) were supplied by Union Carbide for analysis. Yttrium aluminum garnet is cubic with octahedral symmetry at the aluminum site where Ti^{3+} substitution takes place. The other Al^{3+} site has tetrahedral symmetry.

The absorption spectrum of the more heavily doped $\text{Ti}^{3+}:\text{YAG}$ sample is shown in Figure 19. The double peak Ti^{3+} absorption was again present but at longer wavelengths, 505 and 585 nm, than in sapphire. $\text{Ti}^{3+}:\text{YAG}$ is expected to have a smaller crystal field and thus absorption and emission are expected to be shifted to longer wavelengths. There is little evidence of a broadband absorption peak in the 800-nm region indicating that $\text{Ti}:\text{YAG}$ should not have the anomalous absorption problem of $\text{Ti}:\text{YAlO}_3$.

Like the absorption peaks, the fluorescence of $\text{Ti}^{3+}:\text{YAG}$ was shifted to longer wavelengths with a maximum at 766 nm (Figure 20). At low temperatures, zero-phonon lines were observed at 650.6, 651.4, and 653.3 nm. The zero-phonon lines were too close together to make accurate linewidth measurements. Room temperature (300 K) fluorescence was found to be much lower

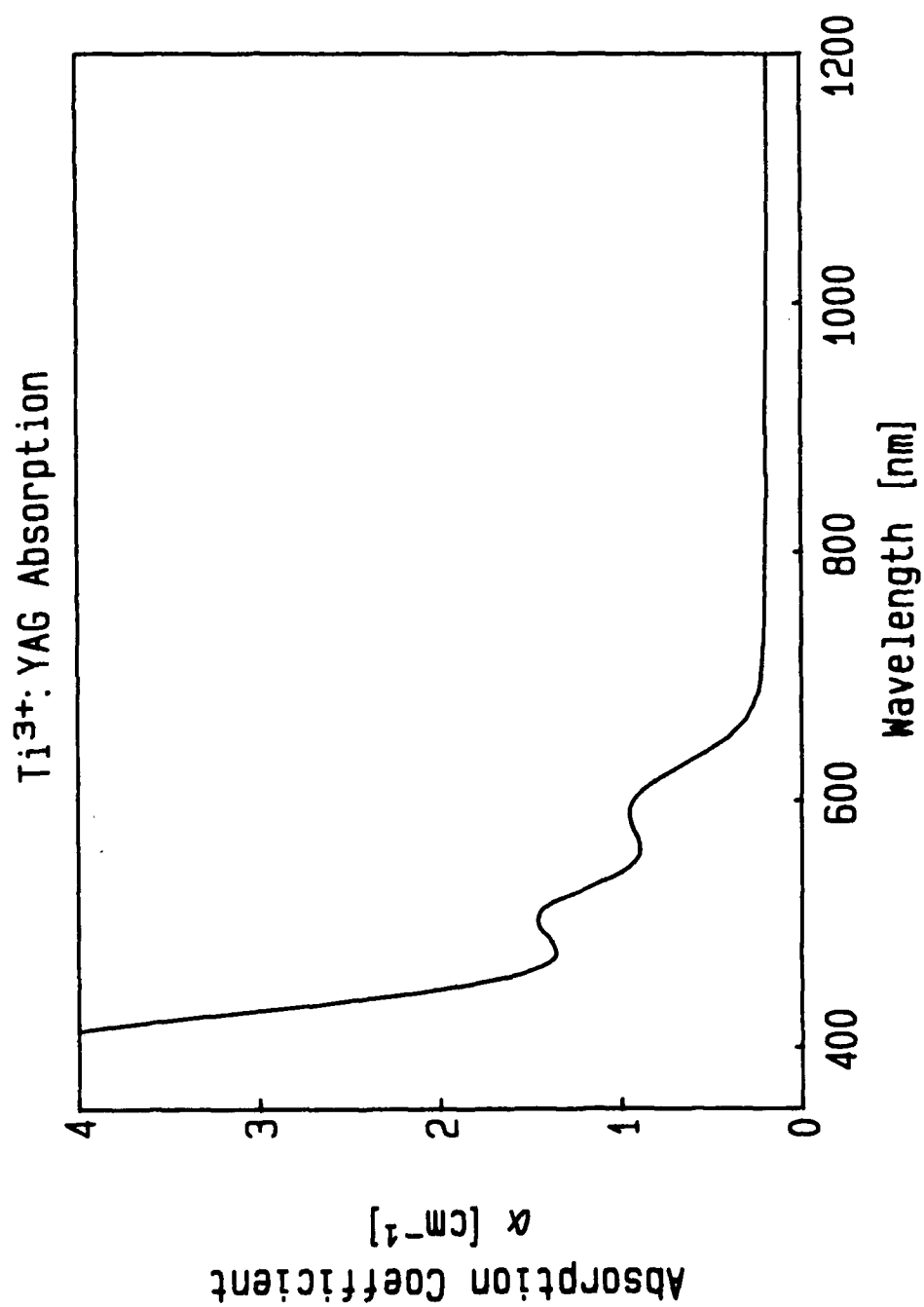


Figure 19. Ti³⁺:YAG absorption at room temperature.

Ti:YAG Fluorescence

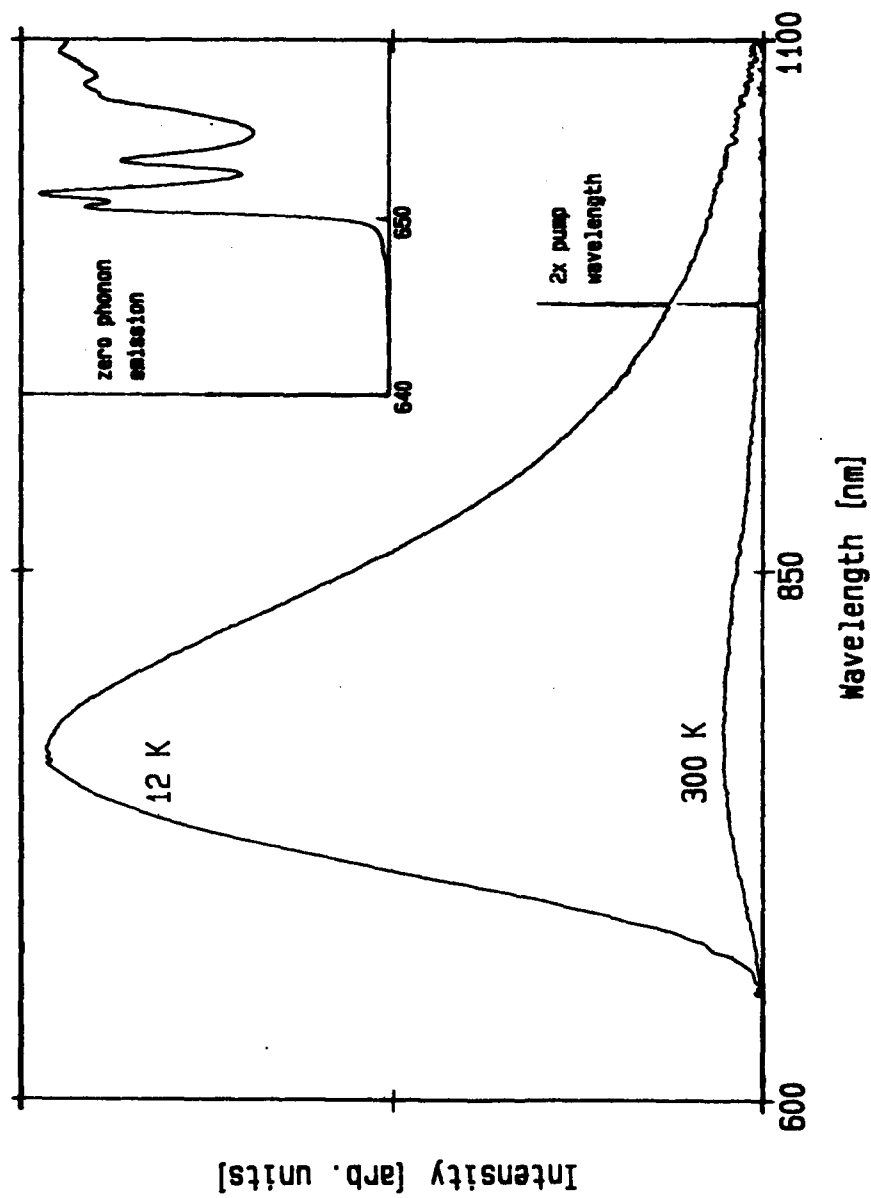


Figure 20. Ti³⁺:YAG fluorescence at 12 and 300 K. Zero-phonon emission in the 650 - 655 nm region is shown in the inset.

in intensity than the 12 K spectrum. A plot of the integrated fluorescence intensity versus temperature is shown in Figure 21. Integrated intensity began to decrease in magnitude at temperatures above 100 K. The fluorescence lifetime (also shown in Figure 21) followed a similar trend indicating that nonradiative loss begins at much lower temperatures in Ti^{3+} :YAG. The Ti :YAG lifetime was measured to be 48 μs at 11 K. This lifetime, much longer than the Ti :sapphire lifetime, is caused by the presence of inversion symmetry in the YAG crystal. But the lifetime quenches rapidly with increasing temperature indicating that nonradiative relaxation begins to occur at temperatures well below room temperature. The rapid quenching with temperature makes laser operation at room temperature highly unlikely. There was no significant difference in lifetime between the lightly and heavily doped Ti^{3+} :YAG samples. As a follow-on to this effort, some measurements of single pass gain and possibly lasing will be attempted at low temperatures (77 K).

Ti^{3+} :GSGG

A small service contract was negotiated and signed with Litton Airtron to grow spectroscopic and laser samples of Ti^{3+} doped GSGG (gadolinium-scandium-gallium garnet) if possible. Samples grown had a pale yellow color and an almost featureless, gradually decreasing transmission with decreasing wavelength. In the first two samples, fluorescence was weak and did not seem to correlate with Ti^{3+} concentration. Broadband fluorescence was observed in the red and near-IR regions but it had an unusually long lifetime of 110 μs . Finally, when the low-temperature fluorescence was measured at 11 K and compared to Cr^{3+} :GSGG fluorescence, the nearly identical spectra made it clear that the observed fluorescence in the " Ti^{3+} :GSGG" samples was due to Cr^{3+} impurities.

The Airtron approach to growing Ti^{3+} :GSGG was to initially

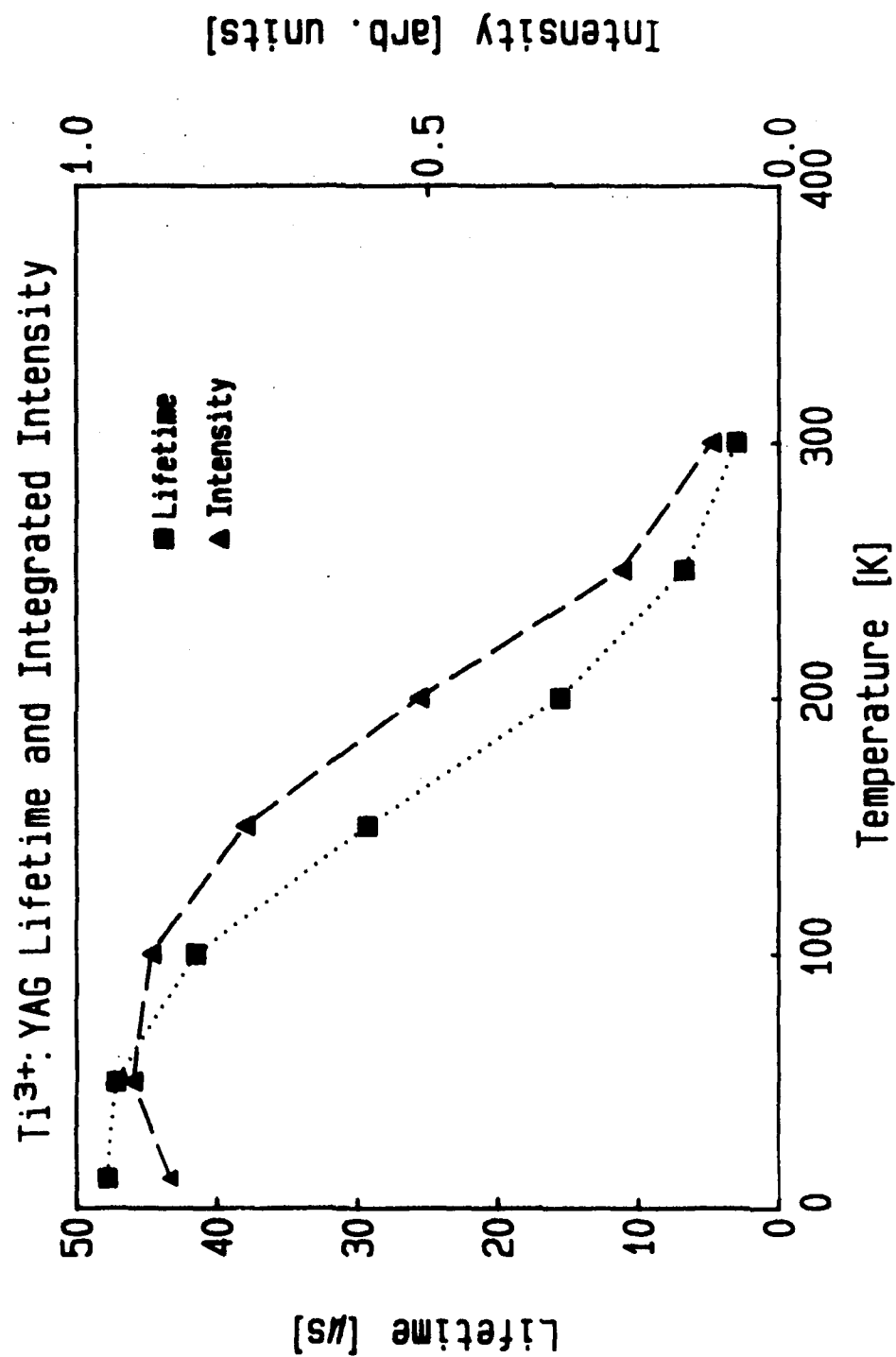


Figure 21. $\text{Ti}^{3+}:\text{YAG}$ fluorescence lifetime and integrated intensity vs. temperature.

use an oxidizing atmosphere during growth to prevent volatilization of gallium. Then an annealing step was employed to reduce titanium incorporated as Ti^{4+} to Ti^{3+} by heating the sample in a reducing atmosphere. Chemical analysis of boules grown indicated that titanium was present but there was no spectroscopic evidence of Ti^{3+} ions. Once incorporated into the GSGG lattice titanium appears to be immune to any attempts to change its valence state. Growth of Ti^{3+} :GSGG was discontinued.

Ti^{3+} :GSAG

A program to grow spectroscopic samples of Ti^{3+} doped gadolinium-scandium-aluminum garnet (GSAG) was initiated with Union Carbide. This garnet host was chosen because crystals could be grown in neutral or reducing atmospheres; volatilization or change in oxidation state of gallium makes growth of GSGG in an oxidizing atmosphere necessary. Samples of Ti^{3+} :GSAG were grown in a 2" diameter by 2" high crucible. The initial sample was doped with 1 at% Ti and was pale yellow in color. The absorption spectrum showed weak absorption in the 500-600 nm region and strong absorption at 450 nm. Further investigation of this and other samples¹⁵ showed that two ions were responsible for the observed optical properties. The absorption peak at 450 nm and correlated yellow fluorescence in the 500-650 nm region were due to the presence of Ce^{3+} contamination. The two broadband absorption peaks at 520 nm and 620 nm were identified as Ti^{3+} absorption (see Figure 22). Broadband emission from 690 nm to beyond 1150 nm and peaked at 840 nm was also observed (see Figure 23). Excitation spectrum measurements showed that the absorption peaks at 520 and 620 nm were directly related to the 840-nm emission peak. Even with relatively high doping levels of titanium (up to 3 at%) the absorption was quite weak when compared to Ti:sapphire. Either only a small fraction of the titanium was being incorporated or much of the titanium

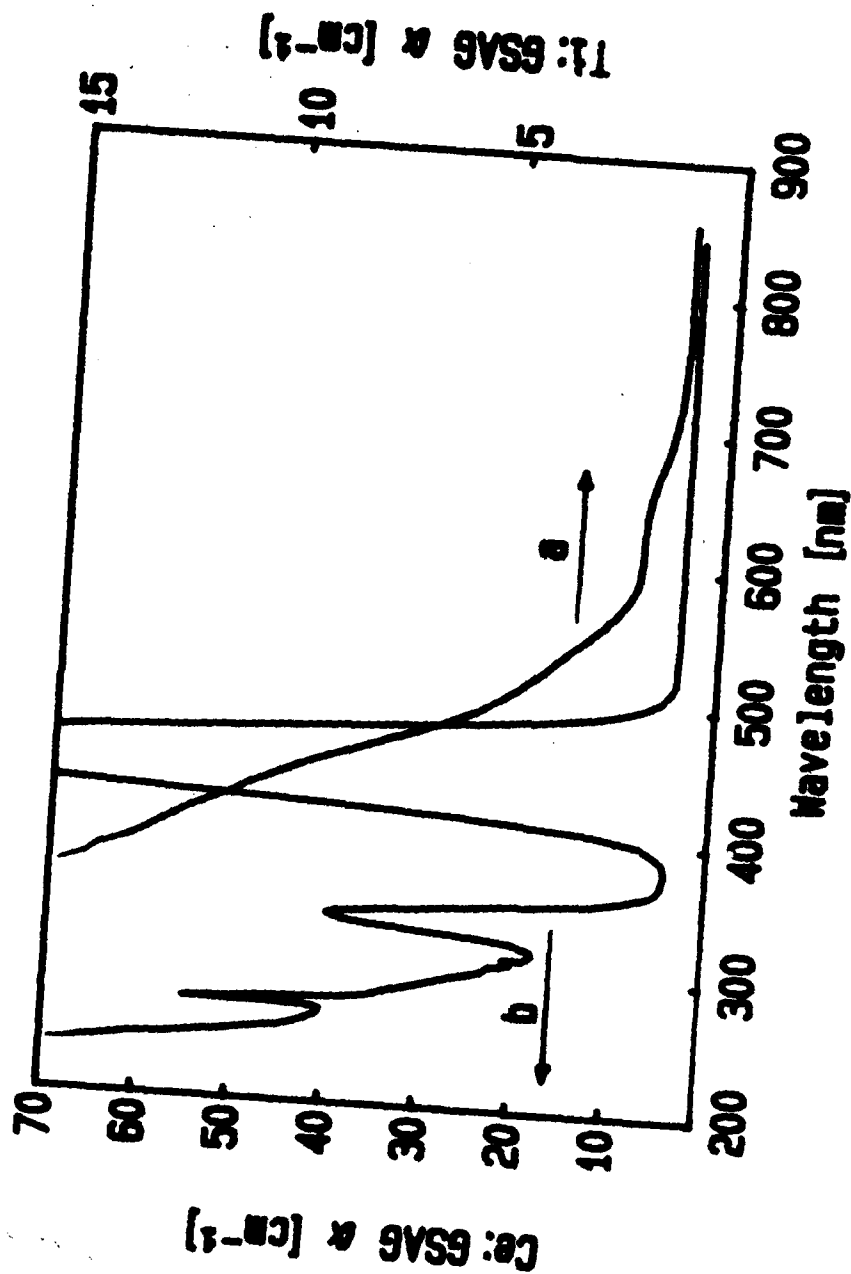


Figure 22. Absorption at room temperature by (a) a Ti^{3+} :GSAG crystal and by (b) a Ce^{3+} :GSAG crystal. The presence of a peak at 450 nm in sample (a) indicates that some Ce^{3+} impurity ions are present. The weak features at 520 and 620 nm are Ti^{3+} absorption.

Ti:GSAG Fluorescence

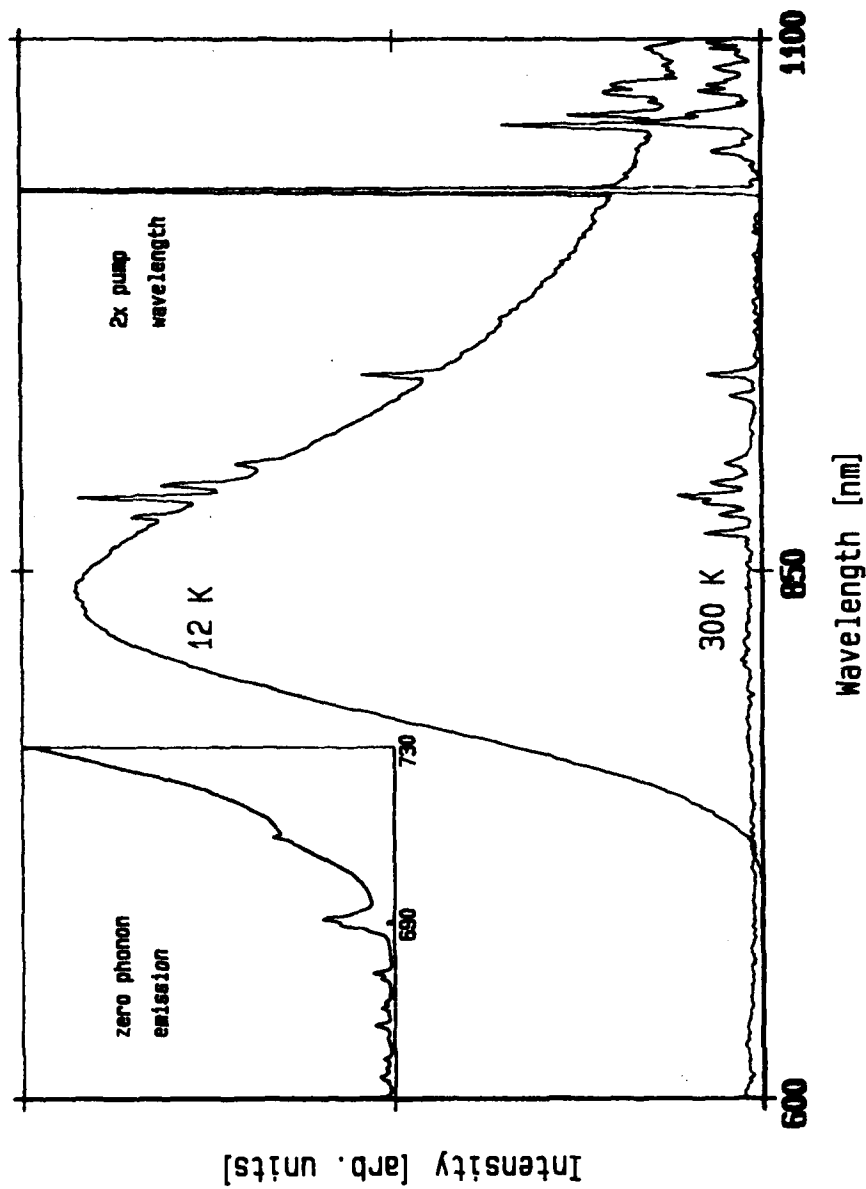


Figure 23. Ti^{3+} :GSAG fluorescence at 12 and 300 K. Zero-phonon emission in the 690 nm region is shown in the inset.

incorporated into the crystal was Ti^{4+} rather than Ti^{3+} .

The sharp peaks in the 850-900 nm region and another group in the 1000-1100 nm region are clearly not related to the $\text{Ti}:\text{GSAG}$ emission since they do not decrease in magnitude like the broadband peak does when going to higher (room) temperatures. Peaks in both regions were identified as fluorescence of Nd^{3+} impurities.

The inset of Figure 23 shows the emission of the short wavelength side of the $\text{Ti}:\text{GSAG}$ sample. The features near 690 nm were tentatively identified as one or more zero-phonon lines since linewidths had a temperature dependence similar to that observed in other Ti^{3+} doped materials.

Fluorescence lifetime measurements are shown in Figure 24. Although the lifetime (5.5 μs) was greater than the $\text{Ti}:\text{sapphire}$ lifetime at 11 K, it decreased rapidly above 50 K. The integrated fluorescence intensity also decreased rapidly as temperature increased (also shown in Figure 24). At room temperature, the fluorescence emission was almost totally quenched by nonradiative relaxation.

Further work is being done to investigate the feasibility of lasing Ti^{3+} ions in GSAG . Although cryogenic cooling would be necessary for efficient lasing, the broadband tuning range possible extends farther into the infrared than with $\text{Ti}:\text{sapphire}$ making this material of interest in a number of applications such as fibers and frequency doubling to 455 nm.

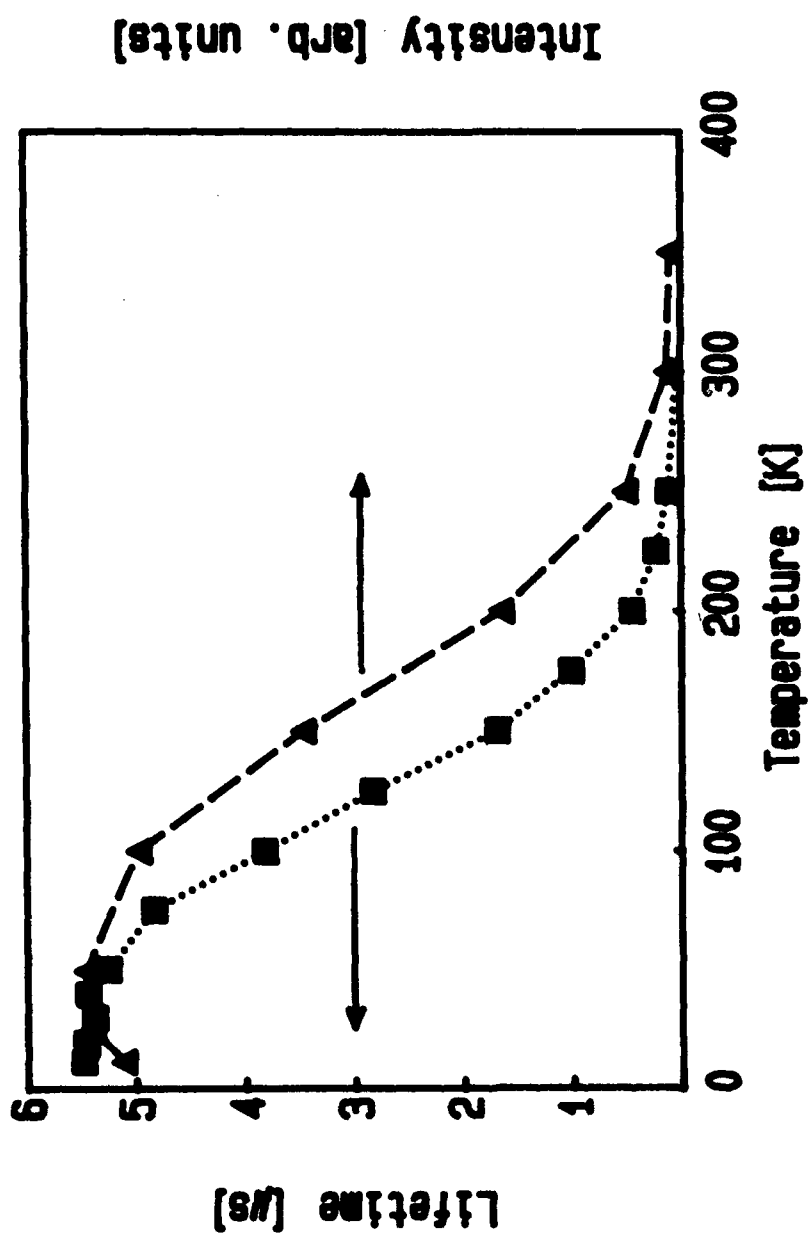


Figure 24. Ti^{3+} :GSAG fluorescence lifetime and integrated intensity vs. temperature.

SECTION 3

Theoretical Review of Ti^{3+} Spectroscopic Properties

The Vibronic Hamiltonian

In a crystal, each ion is subject to an electric field originating from the surrounding ions. This crystal field removes the spherical symmetry of a free ion and splits the electronic orbital degeneracy outside the closed shell since the ion's electrons will prefer to avoid regions where electronic density of the surrounding ions is greatest. For transition metal ions with d-orbital electrons (such as Ti^{3+} and Cr^{3+}) the effect of the crystal field is large. In contrast, the crystal field effect is small for lanthanide ions with f-orbital electrons (such as Nd^{3+}) because the f electrons are shielded by outer-lying s and p electrons. Thus, transition metal ions have electron orbital splittings which are quite sensitive to the crystal symmetry and component ions of their host lattice while lanthanide ions are relatively insensitive.

Tanabe and Sugano¹⁶ have calculated the crystal field effects on all d^n ions in octahedral symmetry. In the case of Ti^{3+} , there is one 3d electron outside filled argon and 4s shells. In octahedral symmetry, there are six equidistant negative ions positioned on the x, y and z axes. The five d orbitals (d_{x^2} , $d_{x^2-y^2}$, d_{xy} , d_{xz} and d_{yz}) are split into two groups. The d_{xy} , d_{xz} and d_{yz} orbitals have their electron density maxima directed between the negative ions but the d_{x^2} and $d_{x^2-y^2}$ are directed straight at the negative ions. Thus d orbitals are split into two types, e (d_{x^2} and $d_{x^2-y^2}$) and t_2 (d_{xy} , d_{xz} and d_{yz}), with the splitting directly proportional to the crystal field strength (see Figure 25). If the crystal symmetry is less than octahedral, then further splitting of the d orbitals occurs.

Crystal Field Splitting of d Orbital

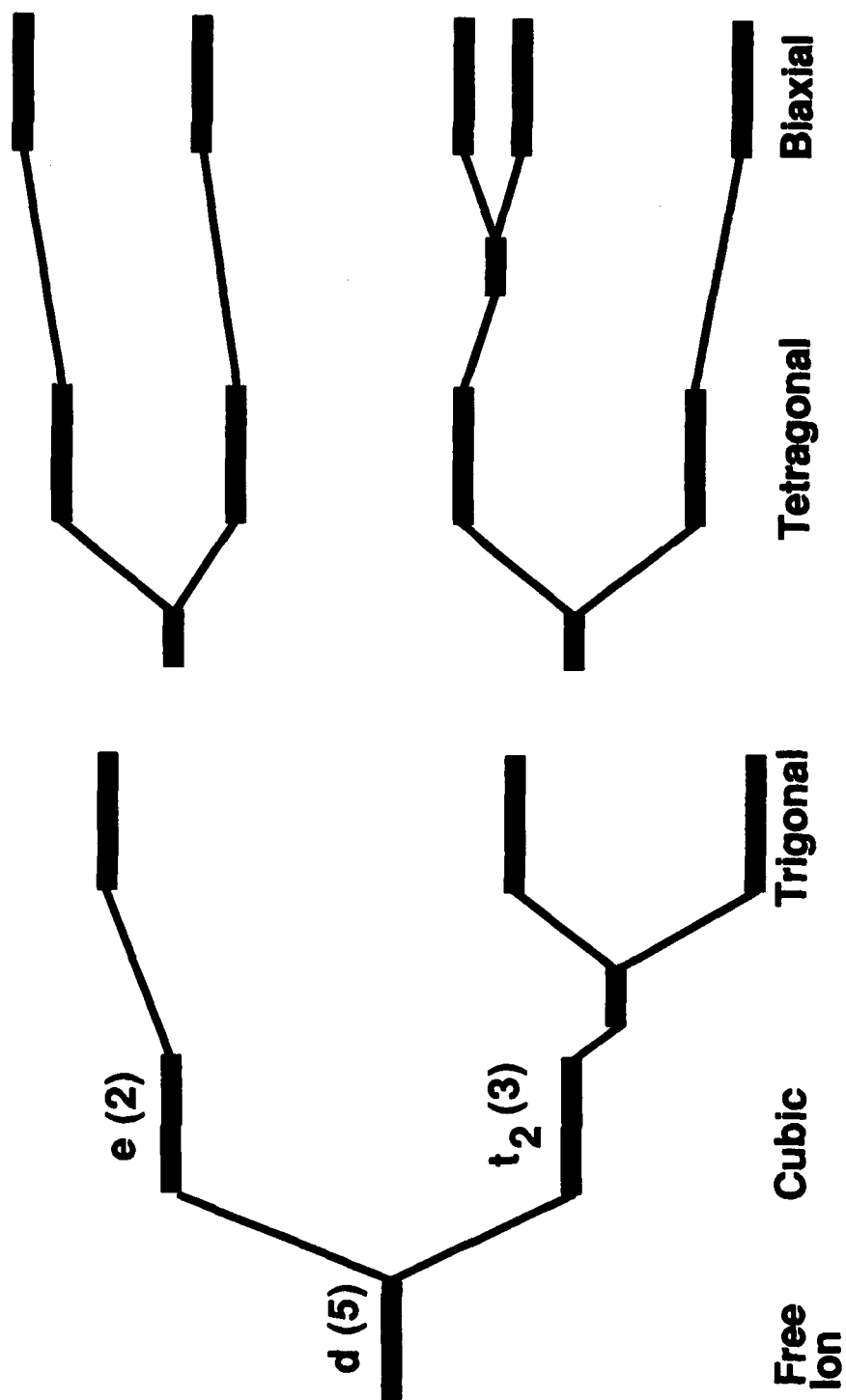


Figure 25. Splitting of a d orbital under crystal fields of successively lower symmetry.

Figure 25 also shows the effects of trigonal and tetrahedral symmetries. Trigonal symmetry (the symmetry present in Al_2O_3) splits the triply degenerate t_2 level into an upper doublet and a ground-state singlet but does not break the degeneracy of the doubly degenerate e level. Further reduction in crystal symmetry (such as adding a biaxial symmetry component) ultimately removes all degeneracy resulting in five singlet levels.

Up to this point, motion of the ionic nuclei in the crystal has not been considered. The potential seen by an electron in some crystalline framework has a static and a dynamic part.

$$V(q, Q) = V_0(q) + \sum_k (\delta V / \delta Q_k) Q_k + \text{higher order terms} \quad [3.1]$$

where q is the electronic position, Q_k is the k -th normal coordinate of a central cation surrounded by six nearest neighbor anions, V_0 is the static potential, and we assume that the dynamic part of the potential can be expanded in powers of Q . In the harmonic approximation we may ignore higher order terms and use only the first two terms of eq. 3.1. The nuclear Hamiltonian reduces to a sum of independent harmonic oscillators, one for each normal mode k , i.e.,

$$H_{\text{nuc}} = \frac{1}{2} \sum_k [P_k^2 / \mu_k + \mu_k \omega_k^2 Q_k^2] \quad [3.2]$$

and

$$E_n(n_1 \dots n_k \dots) = \sum_k \hbar \omega_k (n_k + 1/2) \quad [3.3]$$

$$n_k = 0, 1, 2, \dots$$

where P_k is the conjugate momentum operator, μ_k is the effective mass, and ω_k is the frequency of the k th normal mode. Strictly

speaking, a crystalline solid does not have the normal modes of an isolated molecule but to the extent that nearest-neighbor interactions dominate, using the normal modes as definitions of the Q_k coordinates is a valid approximation.

The Hamiltonian for the active electrons (i.e., electrons which are not in closed shells) has a static part, when $Q_k = 0$, and an active part which is the second term of equation 3.1. Using first order perturbation theory, the effective electronic Hamiltonian can be written

$$H_{ij} = E_i \delta_{ij} + \sum_k \bar{h}_{ij}(k) Q_k \quad [3.4]$$

where

$$\bar{h}_{ij}(k) = \langle i | \delta V / \delta Q_k | j \rangle \quad [3.5]$$

is a $g \times g$ matrix and g is the degeneracy of the electronic level. Combining equations 3.2 and 3.4 gives the first-order Hamiltonian for the whole system, both electrons and nuclei. The eigenfunctions of this combined Hamiltonian are a vibronic wave function ψ . In the absence of any crystal field, $h_{ij} = 0$, and ψ is a product of the electronic and nuclear wavefunctions (the Born-Oppenheimer approximation). But the introduction of a crystal field results in a vibrational-electronic (vibronic) interaction making the electronic wavefunctions and energies no longer independent of the nuclear wavefunctions.

Configuration-Coordinate Model

A useful aid in understanding vibronic interactions is the configuration-coordinate model.^{17 18 19} Consider an ion with two nondegenerate states. Group theory arguments can easily show that only a totally symmetric distortion can produce a first-order shift in a nondegenerate level.²⁰ Thus the discussion is confined to the totally symmetric "breathing" mode of the system

and $Q = Q_1$ is a measure of the deviation of the mean nearest-neighbor separation from its equilibrium value. The energy of the ground electronic state, because of the vibrational interaction, has a quadratic dependence on Q , i.e.,

$$E_1 = \frac{1}{2}\mu\omega^2 Q^2 \quad [3.6]$$

The upper electronic state has a similar energy curve but the separation between states contains a term linear in Q so the minimum of the upper parabola will be at finite $Q = Q_0$. The difference in position in energy minimum for the two different energy levels is intuitive when we remember that the higher energy wavefunction has a different symmetry and thus has a different equilibrium position for the surrounding ions.

$$E_2 = E_0 + \frac{1}{2}\mu'\omega'^2(Q - Q_0^2) \quad [3.7]$$

In Figure 26, equations 3.6 and 3.7 are shown in a configuration coordinate diagram. The ordinate is energy and the abscissa Q represents the deviation of the mean nearest-neighbor separation from the ground-state equilibrium value. The harmonic oscillator force constant has also been assumed to be the same for both levels, i.e., $\mu\omega^2 = \mu'\omega'^2$ which means that there is zero quadratic coupling.

The absorption and fluorescence spectra of transition metal ions are aptly explained by the configuration coordinate model. Possible transitions between the two electronic states are represented in Figure 26 by vertical lines based on the Franck-Condon principle^{21 22} which states that electronic transitions occur rapidly relative to nuclear motion. The broadband nature of both the absorption and fluorescence is due to differences in equilibrium position of the ground and excited states. Even at 0° K zero-point motion spreads the wave function in a Gaussian manner allowing a distribution of transitions with different energies.

The basic operation of a vibronic laser as a four-level laser is also shown in Figure 26. Excitation can be either broadband

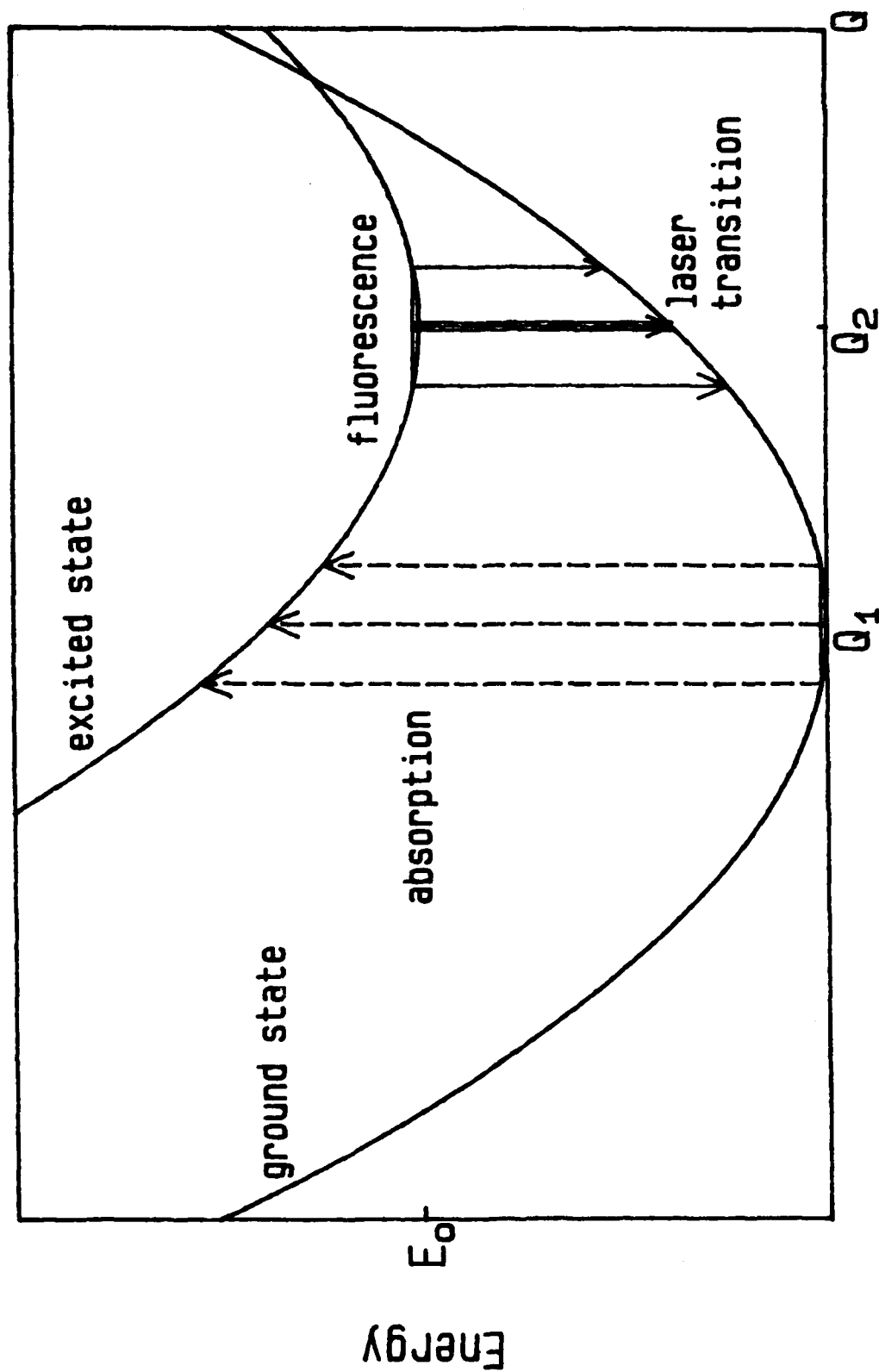


Figure 26. Generalized configuration coordinate diagram for a transition metal ion with two vibrationally coupled energy levels. The excited state is also Stokes shifted.

(flashlamp pumping) or narrow-band (laser pumping). Once excited the electron then rapidly relaxes to the lower vibrational levels of the excited state by emitting phonons to the lattice. Stimulated emission can then occur at any of the fluorescence wavelengths provided losses are overcome and some mechanism for wavelength selection is used. Fluorescence or laser emission returns the ion to its ground electronic state but in a vibrationally excited state. Again phonons are rapidly emitted to the lattice returning the ion to its ground state.

Jahn-Teller Effect on Ti^{3+} Ions

Up to this point degeneracy of a particular energy level has not been considered. However, the Jahn-Teller theorem²³ states that any complex occupying an energy level with electronic degeneracy is unstable against a distortion which removes the degeneracy to first order. The instability arises because even though the center of gravity of the level remains constant, a linear splitting of the level must result in a state with lower energy than the unsplit level. The distortion is opposed by crystal field forces and thus a new position of equilibrium is reached which has lower local symmetry. Interestingly, Sturge²⁰ makes the point that a distortion that removes electronic degeneracy must itself be degenerate so there will be more than one position of equilibrium with equal energy. Thus the original electronic degeneracy is replaced with a more complicated vibronic degeneracy. As will be shown below, Ti^{3+} ions are a good example of this effect.

Ti^{3+} ions in an octahedral field have a triply degenerate ground state ($2T_2$) and a doubly degenerate excited state ($2E$). Because interpretation of the optical properties of Ti^{3+} ions depends on Jahn-Teller effects, a theoretical review of Jahn-Teller splittings is given below. A more thorough and rigorous discussion of the Jahn-Teller effect is given by Sturge.²⁰

As shown in Table 2, the distortions of an octahedron can be analyzed into 15 normal modes. The odd parity distortions are not of interest because we are considering a centrosymmetric system. A group theoretical proof of the Jahn-Teller theorem requires that the irreducible representation of the distortion (Γ_d) must be contained in the symmetric direct product [Γ^2] if the matrix element of equation 3.5 is not to vanish; Γ is the irreducible representation of the energy level under consideration.

The Jahn-Teller Effect in the 2E Doubly Degenerate State

For the doubly degenerate 2E level, [E^2] = $A_1 + E$. Thus the τ_{2g} distortions do not split the level. The α_g distortion is totally symmetric and can only shift the 2E energy, not split the level. Only the doubly degenerate e_g remains to be considered. The irreducible representations of the doubly degenerate 2E level are:

$$\Gamma_2 = \begin{bmatrix} 0 & 1 \\ 1 & 0 \end{bmatrix}, \quad \Gamma_3 = \begin{bmatrix} -1 & 0 \\ 0 & 1 \end{bmatrix} \quad (3.8)$$

so using eqs. 3.4 and 3.5 and the Wigner-Eckart theorem

$$H_{ij} = -Ap \begin{bmatrix} -Q_3 & Q_2 \\ Q_2 & Q_3 \end{bmatrix} + \frac{1}{2} \mu \omega_E^2 p^2 + T_E \quad (3.9)$$

where T_E is the nuclear kinetic energy and A is a measure of the strength of the Jahn-Teller coupling. Converting to polar coordinates, i.e., $Q_3 = p \cos \theta$, $Q_2 = p \sin \theta$, yields:

$$H_{ij} = -Ap \begin{bmatrix} -\cos \theta & \sin \theta \\ \sin \theta & \cos \theta \end{bmatrix} + \frac{1}{2} \mu \omega_E^2 p^2 + T_E \quad (3.10)$$

The determinant of the matrix in eq. 3.10 is the product of the eigenvalues so the energies are

$$E_{\pm} = \pm Ap + \frac{1}{2} \mu \omega_E^2 p^2 + T_E \quad (3.11)$$

Thus, the potential energy surface is double valued and

Table 2
Normal Mode Coordinates for the Octrahedral XY_6 Complex

<u>Mode</u>	<u>Symmetry</u>	<u>Coordinates</u>
Q ₁	α_{1g}	$(x_1 - x_4 + y_2 - y_5 + z_3 - z_6)/\sqrt{6}$
Q ₂	ϵ_g	$(x_1 - x_4 - y_2 + y_5)/2$
Q ₃	ϵ_g	$(2z_3 - 2z_6 - x_1 + x_4 - y_2 + y_5)/2\sqrt{3}$
Q ₄	τ_{2g}	$(z_2 - z_5 + y_3 - y_6)/2$
Q ₅	τ_{2g}	$(x_3 - x_6 + z_1 - z_4)/2$
Q ₆	τ_{2g}	$(y_1 - y_4 + x_2 - x_5)/2$
Q ₇	τ_{1u}	$(x_2 + x_3 + x_5 + x_6)/2$
Q ₈	τ_{1u}	$(y_1 + y_3 + y_4 + y_6)/2$
Q ₉	τ_{1u}	$(z_1 + z_2 + z_4 + z_5)/2$
Q ₁₀	τ_{1u}	$(x_1 + x_4)/\sqrt{2}$
Q ₁₁	τ_{1u}	$(y_2 + y_5)/\sqrt{2}$
Q ₁₂	τ_{1u}	$(z_3 + z_6)/\sqrt{2}$
Q ₁₃	τ_{2u}	$(x_2 + x_5 - x_3 - x_6)/2$
Q ₁₄	τ_{2u}	$(y_3 + y_6 - y_1 - y_4)/2$
Q ₁₅	τ_{2u}	$(z_1 + z_4 - z_2 - z_5)/2$

In odd parity modes the central ion is held fixed rather than the center of mass.

cylindrically symmetric. The surface consists of a parabola offset from the cylinder axis and then swept about the axis as shown in the top part of Figure 27. The form is commonly known as the Mexican hat. The energy surface minimum occurs at a radius

$$p_{\min} = |A|/\mu\omega_e^2 \quad [3.12]$$

and the difference in energy at p_{\min} and $p = 0$ is

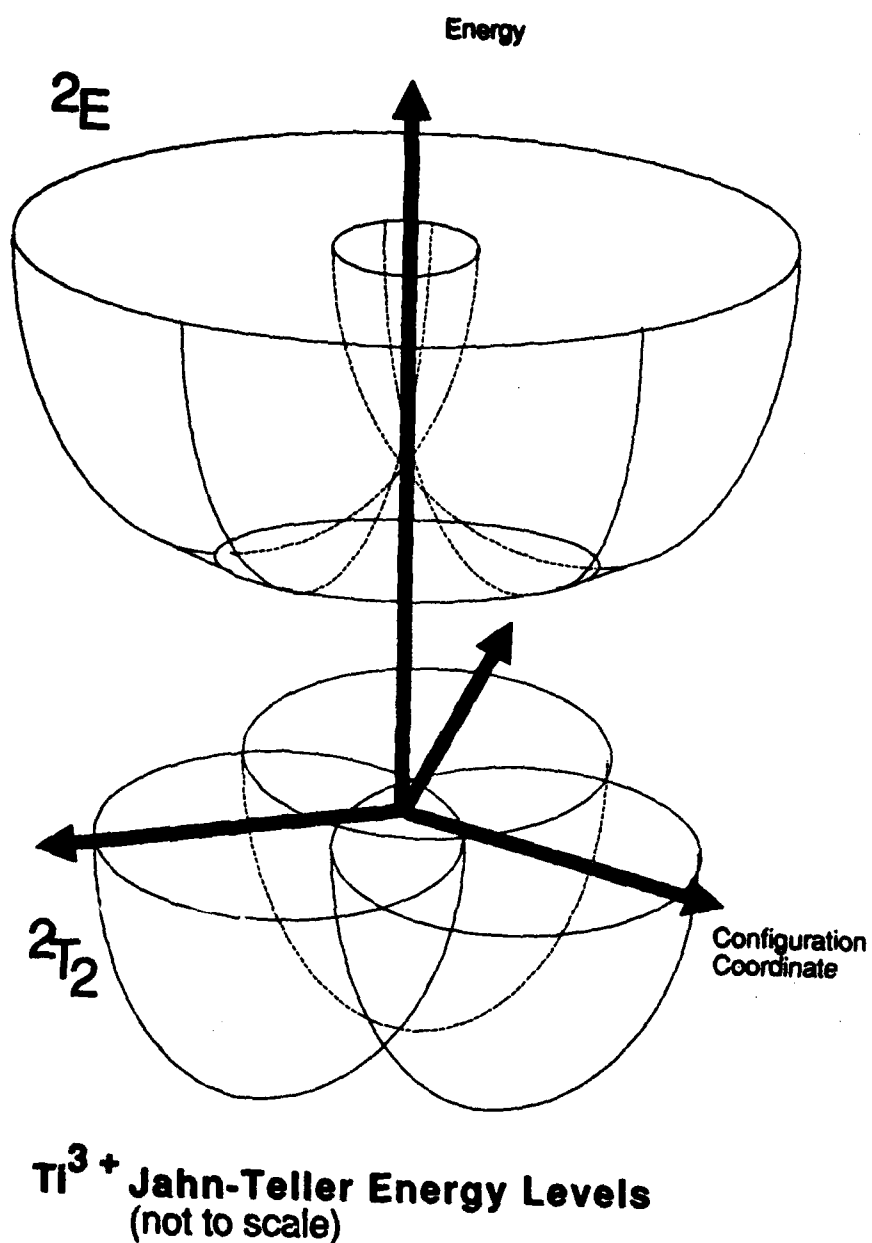


Figure 27. Ti^{3+} Jahn-Teller distorted potential energy surfaces. The energy separation of the two levels and the 2T_2 spread in paraboloid minima are exaggerated for clarity.

$$E(0) - E(\rho_{\min}) = A^2/2\mu\omega_{\epsilon}^2 = E_{JT} \quad [3.13]$$

which is called the Jahn-Teller energy.

The Jahn-Teller Effect in the $2T_2$ Triply Degenerate State

The $Ti^{3+} T_2$ ground-state level has $[T_2]^2 = A_1 + E + T_1 + T_2$ and thus there can be coupling to α_{1g} , ϵ_g and τ_{2g} vibrations. Again, the α_{1g} vibration will not split the level. In octahedral coordination of transition metal ions, the ϵ vibrations couple much more strongly than the τ_{2g} vibrations so the latter can be ignored or at least treated as a perturbation. If we also neglect spin-orbit coupling and anharmonicity, the Hamiltonian of eqs. 3.4 and 3.5 becomes

$$H = A \begin{bmatrix} -q_1 & 0 & 0 \\ 0 & -q_2 & 0 \\ 0 & 0 & -q_3 \end{bmatrix} + \frac{1}{2} \mu\omega_{\epsilon}^2 (q_2^2 + q_3^2) + T_{\epsilon} \quad [3.14]$$

where we have used a real basis set for the T term and defined q_1 , q_2 and q_3 to be nonorthogonal symmetry coordinates equally spaced in the Q_2, Q_3 plane. In this representation the Hamiltonian is diagonal. The q 's are defined as

$$q_1 = -\frac{1}{2} Q_3 + \frac{1}{2}\sqrt{3} Q_2 \quad [3.15a]$$

$$q_2 = -\frac{1}{2} Q_3 - \frac{1}{2}\sqrt{3} Q_2 \quad [3.15b]$$

$$q_3 = Q_3 \quad [3.15c]$$

The energy potential surface thus consists of three separate paraboloids each displaced along a q_i axis by ρ_{\min} and downward by a Jahn-Teller energy E_{JT} where ρ_{\min} and E_{JT} have the same definitions as in eqs. 3.12 and 3.13. A plot of the three potential surfaces is shown in the bottom part of Figure 27.

Macfarlane et al.²⁴ have then taken the next step of reintroducing spin-orbit effects, trigonal distortion, and configurational interaction with the $2E$ level as perturbations. The result is that, in general, the three paraboloids no longer

have equal minima but are split in energy.

Ti³⁺ Optical Properties

Because of the Jahn-Teller splitting of the 2E level, the absorption spectrum of a Ti^{3+} ion will have two broadband peaks, one corresponding to the lower and the other to the upper 2E potential curve (see Figure 28). The splitting of the 2T_2 triplet is a small perturbation and can usually be ignored for discussions of Ti^{3+} optical properties except for discussions of zero-phonon transitions. Also, the double peak absorption feature does not depend on the Jahn-Teller splitting of the lower level. Even if the lower level is nondegenerate and centered at the origin, the three-dimensional nature of the paraboloids would result in a double absorption peak. This is shown as follows: For a ground-state vibrational wave function,

$$\psi = \alpha^{1/2} \exp[-\alpha^2 \rho^2 / 2] , \quad [3.16]$$

the probability distribution is

$$p(\rho) d\rho = 2\alpha^2 \rho \exp[-\alpha^2 \rho^2] . \quad [3.17]$$

This has its maximum at $1/(\alpha\sqrt{2})$, not at $\rho = 0$. Inclusion of ground-state Jahn-Teller splitting would change the location of the probability distribution maximum. The presence of Jahn-Teller splitting of the 2T_2 ground state as well as other perturbations would not be observable in the absorption spectrum since they would only tend to further broaden the already broadband absorption peaks.

Emission (fluorescence) is expected to be a single broadband peak represented by transitions from the lowest vibrational levels of the Mexican hat minimum to the three ground-state paraboloids. Although the upper level has cylindrical symmetry, the ground state does not due to both Jahn-Teller splitting and other perturbations. This asymmetry contributes to the broadness of the transition and has some important consequences

Ti:sapphire Energy Levels Cross-section View

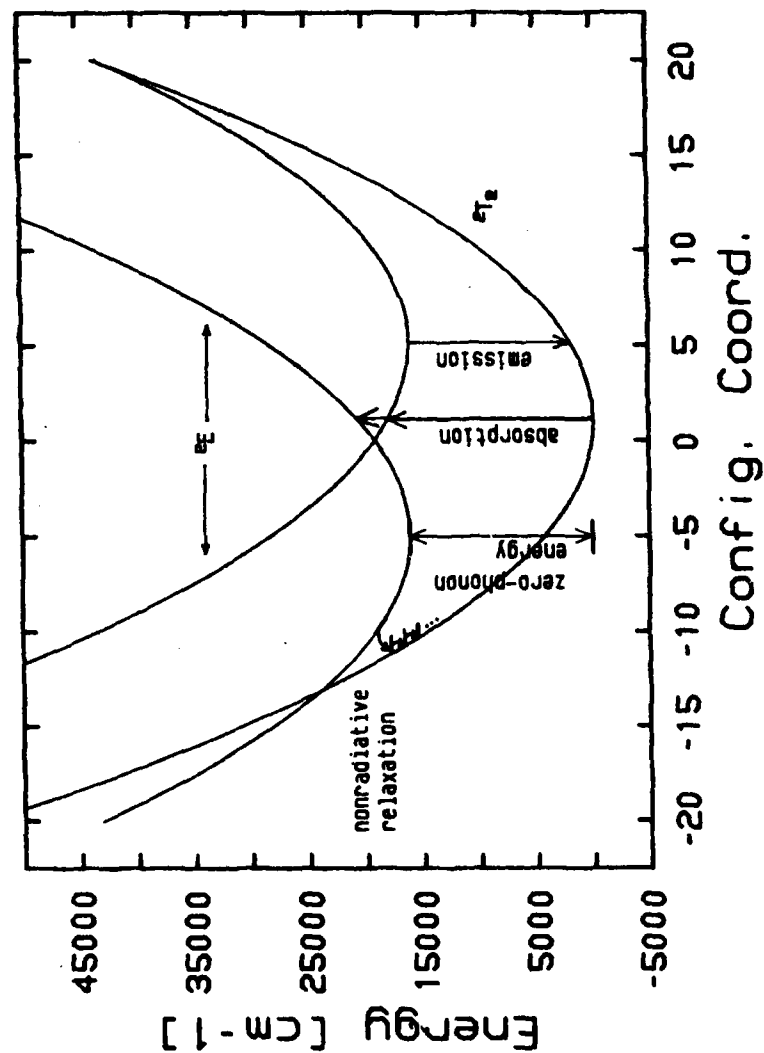


Figure 28. Cross-sectional view of one of the $2T_2$ parabolooids along its centroid and the corresponding slice through the excited $2E$ level. This figure is to scale for the model calculations of Section 4.

concerning the probability of nonradiative transitions. This topic will be discussed further in Section 4.

The quantum mechanical wavefunctions extend beyond the classical potential curves and this can result in a finite probability of direct zero-phonon transitions between the 2E and 2T_2 states. Such transitions, both in absorption and emission, will be very sharp since they do not involve coupling to the lattice. In general, three peaks will be split by perturbations discussed above. However, the zero-phonon intensities are expected to be quite small and could easily be obscured by the broadband multi-phonon transitions.

SECTION 4

Comparison of Ti^{3+} Spectroscopic Properties in Different Hosts

Ti^{3+} Energy Levels

The theoretical description of energy levels and optical transitions in Ti^{3+} ions given in Section 3 is valid for any crystalline host. The specific values required to fit the theoretical model will vary from host to host. The spectroscopic measurements described in Sections 1 and 2 can be used to investigate the effects which different hosts can have on Ti^{3+} optical properties.

The ${}^2\text{E}$ excited levels and the ${}^2\text{T}_2$ ground-state levels have energy surfaces described by:

$$V_e(\rho) = E_{\text{CF}} \pm A\rho + \frac{1}{2}\mu\omega^2\rho^2 \quad [4.1a]$$

$$V_g(\vec{\rho}) = \frac{1}{2}\mu\omega^2(\vec{\rho} - \vec{\rho}_a)^2 + E_i - E_{\text{JT}}^T \quad [4.1b]$$

where

E_{CF} = crystal field splitting

E_{JT}^T = Jahn-Teller energy (positive) of the ${}^2\text{T}_2$ state

A = Jahn-Teller coupling strength

$\vec{\rho}_a$ = location of maximum probability density for one of the ${}^2\text{T}_2$ paraboloids

E_i = the splitting energy of the three ${}^2\text{T}_2$ levels with the lowest set at zero

Absorption involves transitions from the ${}^2\text{T}_2$ paraboloid ground states to the ${}^2\text{E}$ excited states. Based on equations 4.1a and 4.1b the two broadband absorption peaks have model energies of:

$$E_1^a = E_{CF} + E_{JT}^T - A\rho_a + \frac{1}{2}\mu\omega^2\rho_a^2 - E_i \quad [4.2a]$$

$$E_2^a = E_{CF} + E_{JT}^T + A\rho_a + \frac{1}{2}\mu\omega^2\rho_a^2 - E_i \quad [4.2b]$$

Thus the difference in energy of the two absorption peaks is

$$\Delta E \equiv E_2^a - E_1^a = 2A\rho_a \quad [4.3]$$

If we define

$$E_0 \equiv E_{CF} + E_{JT}^T - E_i \quad [4.4]$$

then the sum of the absorption peak energies is

$$T \equiv E_1^a + E_2^a = 2E_0 + \frac{1}{2}\mu\omega^2\rho_a^2 \quad [4.5]$$

Physically, E_0 is simply the energy difference between the bottom of a $2T_2$ paraboloid and the $2E$ energy at $\rho = 0$.

Theoretically, zero-phonon absorption should take place as narrow peaks at an energy smaller than the broadband absorption peaks. But at room temperature the zero-phonon peaks were too broad and too weak to be observed. However, sharp but weak zero-phonon transitions were observed in fluorescence experiments at low temperatures. These emission transitions obviously have the same energy as the zero-phonon absorption transitions. In terms of the above equations, the zero-phonon energy can be written as

$$E_z = E_0 - E_{JT}^E = E_0 - A^2/2\mu\omega^2 \quad [4.6]$$

where the second term on the right hand side is the $2E$ Jahn-Teller energy. Using equations 4.3 - 4.6, the Jahn-Teller energy can be calculated in terms of experimentally measured parameters, i.e.,

$$E_{JT}^E = \left\{ T - 2E_z + [(2E_z - T)^2 - \Delta E^2]^{1/2} \right\} / 4 \quad [4.7]$$

We can then use eqs. 4.3 - 4.6 to calculate E_0 , $A\rho_a$ and $\mu\omega^2\rho_a^2$. The scaling of ρ is arbitrary so it is permissible to set $\rho_a = 1$.

Information on the $2T_2$ parabolooids can be gleaned from fluorescence peak information. Fluorescence emission takes place at $\rho = \rho_e$, the configuration coordinate of the $2E$ Mexican hat minimum. The energy of the $2E$ level at this radius is

$$V_e(\rho_e) = E_0 - E_{JT}^E \quad [4.8]$$

The fluorescence transitions are vertical transitions from the Jahn-Teller distorted minimum to the three $2T_2$ parabolooids. For the paraboloid offset from the origin along the x coordinate axis, the energy surface can be written as

$$V_g(\rho_x, \rho_y) = \frac{1}{2}\mu\omega^2[(\rho_x - \rho_a)^2 + \rho_y^2] + E_i \quad [4.9]$$

where the strength of the bottom parabolooids is assumed to be the same as the excited-state ones ($\mu\omega^2$ is the same for both sets of levels, a reasonable assumption in most cases). For $\rho = \rho_e$ (the emission peak) and angle θ in configuration coordinate space,

$$\rho_x = \rho_e \cos \theta \quad [4.10a]$$

$$\rho_y = \rho_e \sin \theta \quad [4.10b]$$

and if we define γ such that $\rho_e = \gamma\rho_a$ then eq. 4.9 becomes

$$V_g(\rho_e) = \frac{1}{2}\mu\omega^2\rho_a^2[\gamma^2 - 2\gamma \cos \theta + 1] + E_i \quad [4.11]$$

The fluorescence transition energy is eq. 4.8 - eq. 4.11 or

$$E_e = E_0 - E_{JT}^E - \frac{1}{2}\mu\omega^2\rho_a^2[\gamma^2 - 2\gamma \cos \theta + 1] - E_i \quad [4.12]$$

Since we are only interested in the peak of the emission here, the average E_e may be used, i.e.,

$$\bar{E}_e = E_0 - E_{JT}^E - \frac{1}{2}\mu\omega^2\rho_a^2[\gamma^2 + 1] - \bar{E}_i \quad [4.13]$$

or

$$\gamma^2 = 2 \left[E_0 - \bar{E}_e - E_{JT}^E - \bar{E}_i \right] \div \mu\omega^2 + 1 \quad [4.14]$$

Once γ is known, A and the Jahn-Teller energy for the $2T_2$ state

can also be calculated.

The results of measurements and calculations are shown in Table 3 for the different host materials studied. In the case of GSAG, identification of the zero-phonon lines is somewhat tentative although use of a feature observed at 691 nm appears to give reasonable results.

A progression of crystal field strength (E_{CF}) correlates with the energies of absorption and emission peaks from strongest to weakest in the four crystals studied. The order is as listed in Table 3: $YAlO_3$, Al_2O_3 , YAG, and GSAG. With one exception, this is the same crystal field strength order seen in these crystals when doped with Cr^{3+} ions (see Table 4). The exception is that the crystal field for Cr^{3+} is about the same in $YAlO_3$ and Al_2O_3 but with Ti^{3+} ions, the crystal field is much higher in $YAlO_3$ than in Al_2O_3 . One possible reason may be the difference in ionic radii of the two dopants. Ti^{3+} is slightly larger than Cr^{3+} and the Ti^{3+} electronic energies should be more sensitive to the locations of surrounding oxygen ions.

The Jahn-Teller energy of the 2E excited state is apparently not directly related to crystal field strength; even the value A is not correlated to field strength. The Jahn-Teller energy is at about 3000 cm^{-1} in all four host materials. The Jahn-Teller energy of the 2T_2 level is much smaller than that of the 2E level and it too does not correlate directly with crystal field. In one sense this can be expected since the matrix element A is proportional to $\delta V/\delta p$ and not V . In a second order calculation of the ground-state Jahn-Teller energy, Macfarlane et al.²⁴ found this energy to be 200 cm^{-1} in $Ti^{3+}:Al_2O_3$. The first order calculations of Table 3 are reasonably consistent with that. Table 3 also agrees well with the sapphire and YAG Jahn-Teller calculations of Albers.²⁵

Table 3
Ti³⁺ Spectroscopy Calculations

	YALO	Sapphire	YAG	GSAG
<hr/>				
Absorption Peak (nm)	435	485	505	520
Absorption Peak (cm ⁻¹)	22989	20619	19802	19231
Absorption Peak (nm)	490	550	585	620
Absorption Peak (cm ⁻¹)	20408	18182	17094	16129
Zero-phonon Peak (nm)	540	617	650	691
Zero-phonon Peak (cm ⁻¹)	18519	16207	15385	14472
Emission Peak (nm)	610	745	766	840
Emission Peak (cm ⁻¹)	16393	13423	13055	11905
Total Energy (T)	43397	38800	36896	35360
Absorption Energy Dif (DE)	2580	2437	2708	3102
<hr/>				
T-2*(zero phonon energy)	6360	6385	6127	6416
Jahn-Teller Energy (2E)	3043	3072	2906	3008
Crystal Field + Pert (E ₀)	21562	19279	18290	17480
Ap _a	1290	1218	1354	1551
μw ² p _a ²	273	242	315	400
<hr/>				
γ	4.07	4.86	3.94	3.72
A'	317	251	343	417
Jahn-Teller Energy (2T ₂)	184	130	187	217
<hr/>				
P _C (crossover min.)	-13.7	-13.0	-10.8	-8.9
Crossover Energy	29557	23950	22110	19428
ΔE	11038	7743	6726	4956

Sapphire and YAG include E₁ ground state splittings for crossover calculations. All energies are in cm⁻¹.

Table 4
Cr³⁺ Absorption Peaks

YAlO ₃	410 nm	555 nm	ref a
Al ₂ O ₃	410 nm	560 nm	ref b
YAG	430 nm	590 nm	ref c
GSAG	450 nm	630 nm	ref d

- a. M. J. Weber and T. E. Varitimos, J. of Appl. Phys. 45, 810 (1974).
- b. D. S. McClure, J. Chem. Phys. 36, 2757 (1962).
- c. M. J. Weber, editor, Handbook of Laser Science and Technology, Vol I, p. 38 (1982).
- d. J. Drube, B. Struve and G. Huber, Optics Commun. 50, 45 (1984).

The fundamental vibration constant, $\mu\omega^2$, is the smallest in sapphire and significantly larger in the other crystals. In fact, Ti:sapphire is consistently different from the other materials in terms of A, A' and both Jahn-Teller energies. Ti:sapphire may be unique because of its strongly uniaxial crystal structure. In contrast, YAG and GSAG are garnets which are isotropic. YAlO₃ is technically biaxial but the three unique sides of the crystal unit cell differ by very small amounts. Thus sapphire is the only material which has large asymmetry in its crystal structure and optical properties. This asymmetry is not accounted for in the theory developed in Section 3 because we began with the assumption of octahedral symmetry at the Ti³⁺ substitution site.

Thermal Dependence of Lifetime

Up to this point temperature dependence of Ti³⁺ spectroscopic properties has not been considered. However, the results of Sections 1 and 2 show that fluorescence intensity and fluorescence lifetime depend on temperature. In general,

lifetime can be described in terms of three different relaxation processes. The total relaxation rate can be written as

$$W_{\text{Total}} = W_{\text{rad}} + W_{\text{vib}} + W_{\text{nonrad}} \quad [4.15]$$

$$\text{with } \tau_{\text{eff}} = W_{\text{Total}}^{-1} \quad [4.16]$$

Here τ_{eff} is the measured lifetime due to the three relaxation processes listed in equation 4.15. W_{rad} is a pure radiative relaxation rate which is temperature independent. W_{vib} is a phonon assisted relaxation process where photon emission occurs in conjunction with creation or annihilation of phonons (lattice vibrations). W_{vib} is expected to depend on temperature and in the case where the phonon-electron interaction is dominated by phonons of only one frequency ω_p , W_{vib} is given by²⁶

$$\begin{aligned} W_{\text{vib}} &= \frac{1}{\tau_{\text{vib}}} \times \left\{ \frac{1+r}{1-r} \right\} = \frac{1}{\tau_{\text{vib}}} \times \coth[\hbar\omega_p/2kT] \quad [4.17] \\ &= \frac{1}{\tau_{\text{vib}}} \langle 2m + 1 \rangle \end{aligned}$$

where τ_{vib} is a constant independent of temperature and $r = \exp[-\hbar\omega_p/kT]$, the Boltzmann factor.

Equation 4.17 was derived from a harmonic oscillator model. The three representations can be shown to be equivalent as follows: For a harmonic oscillator potential, the probability of the m -th level, with energy $m\hbar\omega_p$, being populated is proportional to $\exp[-m\hbar\omega_p/kT] \equiv r^m$. The sum over all levels must equal one so

$$\sum_{m=0}^{\infty} c \cdot r^m = c/(1-r) = 1. \quad [4.18]$$

Thus, $c = 1 - r$.

The expectation value of m , the average vibrational level population, is

$$\langle m \rangle \equiv \sum_{m=0}^{\infty} m(1-r)r^m = r/(1-r). \quad [4.19]$$

Similarly,

$$\langle m + 1 \rangle \equiv \sum_{m=0}^{\infty} (m+1)(1-r)r^m = 1/(1 - r) \quad [4.20]$$

$$\langle 2m + 1 \rangle \equiv \sum_{m=0}^{\infty} (2m+1)(1-r)r^m = (1 + r)/(1 - r). \quad [4.21]$$

Also,

$$\begin{aligned} (1 + r)/(1 - r) &= \{1 + \exp[-\hbar\omega/kT]\}/\{1 - \exp[-\hbar\omega/kT]\} \\ &= \frac{\exp[\hbar\omega/2kT] + \exp[-\hbar\omega/2kT]}{\exp[\hbar\omega/2kT] - \exp[-\hbar\omega/2kT]} \\ &= \coth[\hbar\omega/2kT] \end{aligned}$$

where the p subscript has been dropped.

Nonradiative relaxation involves transitions to the ground state via creation and annihilation of phonons without photon emission. In an early model, nonradiative transitions were pictured as taking place at the crossover point of the ground-state and excited-state parabolas. The nonradiative relaxation was described by a rate constant N and an activation energy E_c which was the energy difference between the excited-state parabola minimum and the crossover point. As temperature increased the thermal population at the crossover energy would increase making nonradiative relaxation more probable. The process is described by Mott's activation energy formula²⁷

$$W_{\text{nonrad}} = N \exp [-E_c/kT] \quad [4.22]$$

One effect of temperature will be to populate higher vibrational levels of the ground-state and excited-state parabolas. The result should be small temperature dependent increases in width of the broadband absorption and fluorescence lines primarily toward lower energies (or longer wavelengths). This may also result in small increases in the radiative relaxation rate.

In addition, population of higher excited-state vibrational levels increases the probability of direct transitions from the excited-state parabola to the ground-state parabola without the

emission of a photon, i.e., nonradiative relaxation. The crossover energy of the $2T_2$ paraboloids and the $2E$ Mexican hat can be calculated by finding the energy at which $V_e = V_g$. Equations 4.1a and 4.1b show that the excited states have cylindrical symmetry about $p=0$ but the three ground-state paraboloids do not. For the paraboloid displaced along the p_x axis (which can be chosen in that manner) the crossover point is symmetric about p_y but not about p_x . The minimum and maximum crossover points occur along the p_x axis so we may set $p_y = 0$, $\theta = 0$ to find them. Making eq. 4.1b scalar and equating equations 4.1a and 4.1b yields

$$\frac{1}{2}\mu\omega^2(p_c - p_a)^2 + E_i - E_{JT}^T = E_{CF} \pm Ap_c + \frac{1}{2}\mu\omega^2 p_c^2 \quad [4.23]$$

$$p_c = \frac{E_o - \frac{1}{2}\mu\omega^2 p_a^2}{-\mu\omega^2 p_a \mp A} \quad [4.24]$$

where E_o is defined by equation 4.4. The minimum energy level crossover occurs at negative p_x when the negative sign is chosen for A in equation 4.24. This is illustrated in Figure 29. Table 3 shows the p_c values calculated using eq. 4.24; it also shows the crossover energy at $p = p_c$ and ΔE . The ΔE energy is the difference between the crossover energy and the excited-state energy minimum. It is expected to be closely related to E_c of eq. 4.22. The value of ΔE decreases in the same way that crystal field does in the $YAlO - GSAG$ series. This is in qualitative agreement with experiment. However, ΔE is too high. An empirical fit of eq. 4.22 to $Ti:sapphire$ lifetime data yields a value of 1600 cm^{-1} for E_c compared to a calculated value of 7743 cm^{-1} (see Table 3). This discrepancy can qualitatively be explained by observing that we are considering a classical activation energy in the Mott model. It is also possible for tunneling to occur from the excited state to the ground state at energies below the crossover energy. This effectively reduces the "activation energy" to some smaller value.

Ti:sapphire Energy Levels Cross-section View

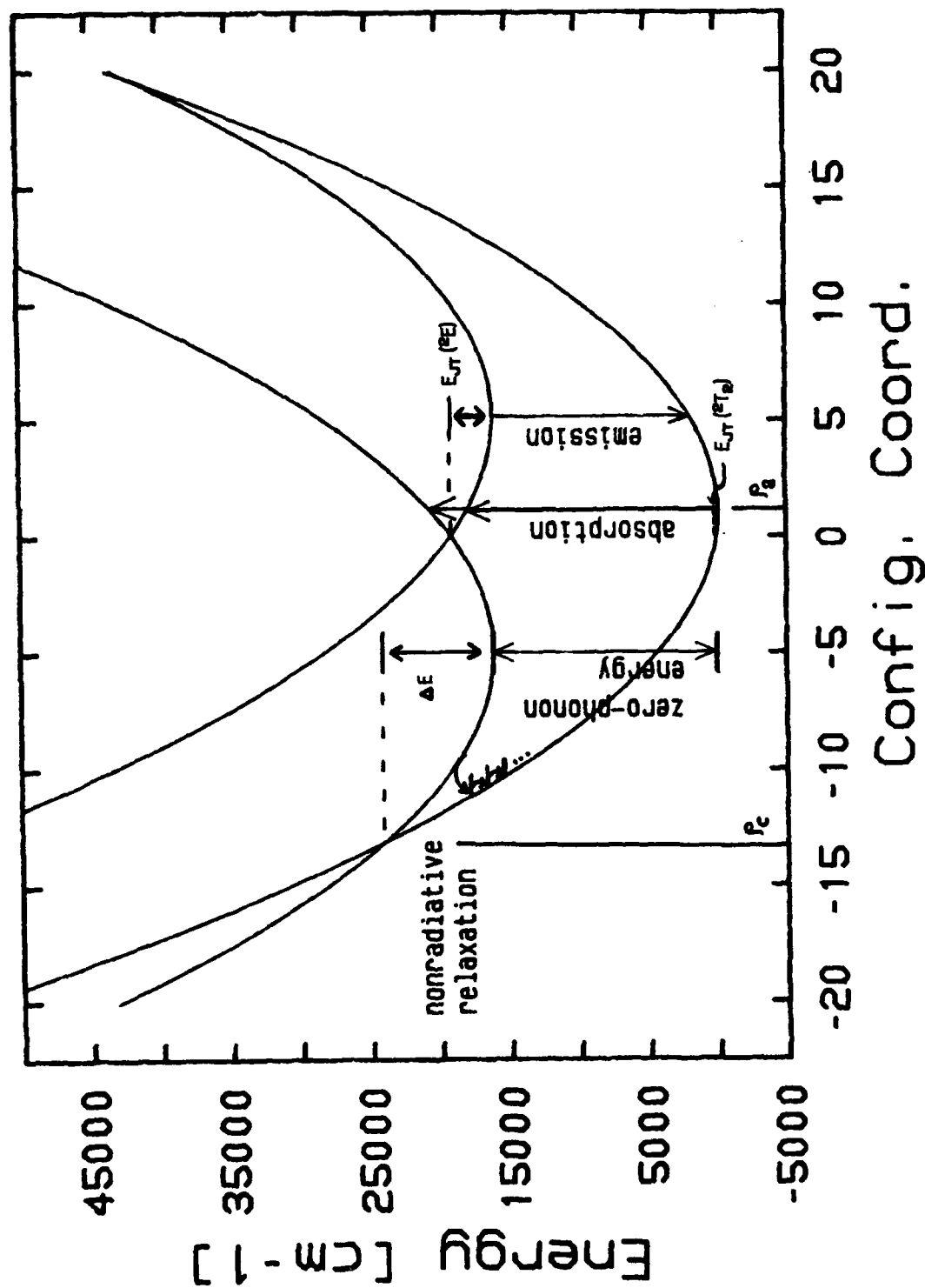


Figure 29. Illustration of configuration coordinate model parameters.

A more general and complete model of nonradiative relaxation using the single-configuration-coordinate model has been developed by Struck and Fonger²⁸. Their model calculates the nonradiative transition rate between a given pair of ground-state and excited-state harmonic oscillator levels (in other words the overlap of the wavefunctions) and then sums over all possible pairs. This approach is analogous to considering multiple activation energies rather than just one. The nonradiative transition probability, assuming equal force constants for excited and ground-state parabolas, can be shown to be

$$P_p = \exp[-S\langle 2m+1 \rangle] \sum_{j=0}^{\infty} \frac{(S\langle m \rangle)^j (S\langle m+1 \rangle)^{p+j}}{j!(p+j)!} \quad [4.25]$$

where $\langle m \rangle$, $\langle m+1 \rangle$, and $\langle 2m+1 \rangle$ are defined in eqs. 4.19-4.21, S is the Stokes shift such that $S\hbar\omega = 1/2\mu\omega^2(p_a - p_e)^2$ and p is a quantum number such that $p\hbar\omega = E_{zp}$. The total nonradiative transition rate is NP_p where N is a term typically on the order of 10^{13} s^{-1} and depends on the electronic part of the wavefunction overlap. Thus eq. 4.15 can be written as

$$W_{\text{Total}} = 1/\tau_{\text{rad}} + 1/\tau_{\text{vib}} \langle 2m+1 \rangle + N \cdot \exp[-S\langle 2m+1 \rangle] \sum_{j=0}^{\infty} \frac{(S\langle m \rangle)^j (S\langle m+1 \rangle)^{p+j}}{j!(p+j)!} \quad [4.26]$$

Eq. 4.26 was used to fit experimental lifetime results for Ti^{3+} ions in the four host materials studied. Values adjusted to fit the experimental results were S , $\hbar\omega$, N , τ_{rad} and τ_{vib} . Once $\hbar\omega$ was chosen, p was defined based on the zero-phonon energy.

Table 5 shows the fitting parameters used for the four different hosts and Figures 30 - 33 are plots of experimental and calculated results. Model parameters were easily adjusted to fit experimental results with all four crystal hosts. Calculated curves were found to be quite sensitive to phonon energy with 1% changes making clearly noticeable differences in calculated curve

Table 5
Titanium Lifetime Modeling

	Ti:YA10	Ti:sapph	Ti:YAG	Ti:GSAG
Zero phonon Energy (cm ⁻¹)	18519	16207	15385	14472
phonon energy (cm ⁻¹)	345	400	390	320
p, phonon quantum #	53	40	39	45
Stokes shift, S	9.5	11.1	11.2	11.5
τ_{vib} (s) see eq. 4.26	1.65E-5	large	2.30E-4	3.00E-4
τ_{rad} (s) see eq. 4.26	large	4.50E-6	large	large
N (Hz) see eq. 4.26	5.0E14	1.8E14	3.3E14	4.0E18
radiative rate at 10 K	6.06E4	2.22E5	4.35E3	3.33E3
radiative rate at 300 K	8.93E4	2.22E5	5.93E3	5.15E3
nonradiative rate at 10 K	8.12E-3	2.17E3	1.84E4	1.83E5
nonradiative rate at 300 K	1.13E1	4.97E4	4.14E5	4.97E7
10 K quantum efficiency (%)	100.0	99.0	19.1	1.79
300 K quantum efficiency (%)	100.0	81.7	1.4	0.01

all rates are in Hz

shapes. Changes in S and N had to be almost in the 10% range to exhibit similar changes. The two lifetimes, τ_{rad} and τ_{vib} (in combination with N), basically scaled the calculations to real time.

The fitted S values in Table 5 can also be compared to S values calculated from fluorescence emission data since

$$S = \ln \left\{ \frac{\int I_{\text{bb}}(\lambda) d\lambda}{\int I_{\text{zp}}(\lambda) d\lambda} \right\} \quad [4.27]$$

where I_{bb} is the broadband fluorescence intensity and I_{zp} is the zero-phonon fluorescence intensity. Intensities at ~10 K were used for both bands and I_{zp} was calculated for only the highest energy zero-phonon line in the YAG and sapphire cases where more than one line was observed. PMT results were used for I_{zp} integrated intensity measurements because of the high sensitivity available and Si photodiode results were used for I_{bb} because of the better sensitivity to long wavelengths. The two measurements were then calibrated to each other at some common wavelength. The results are shown in Table 6. These values are in good agreement with those shown in Table 5.

Table 6
Integrated Intensity S Values

YAlO ₃	sapphire	YAG	GSAG
S = 9.0	10.0	9.6	11.1

In Ti:YAlO₃, the change in lifetime is due almost exclusively to an increase in the radiative transition rate, the $\langle 2m + 1 \rangle$ term. The nonradiative transition rate is extremely low due to the large crystal field. Calculations indicate that nonradiative transitions should become significant at temperatures above 400 K. Experiments above 400 K would be useful to confirm this.

Ti:YAlO Lifetime

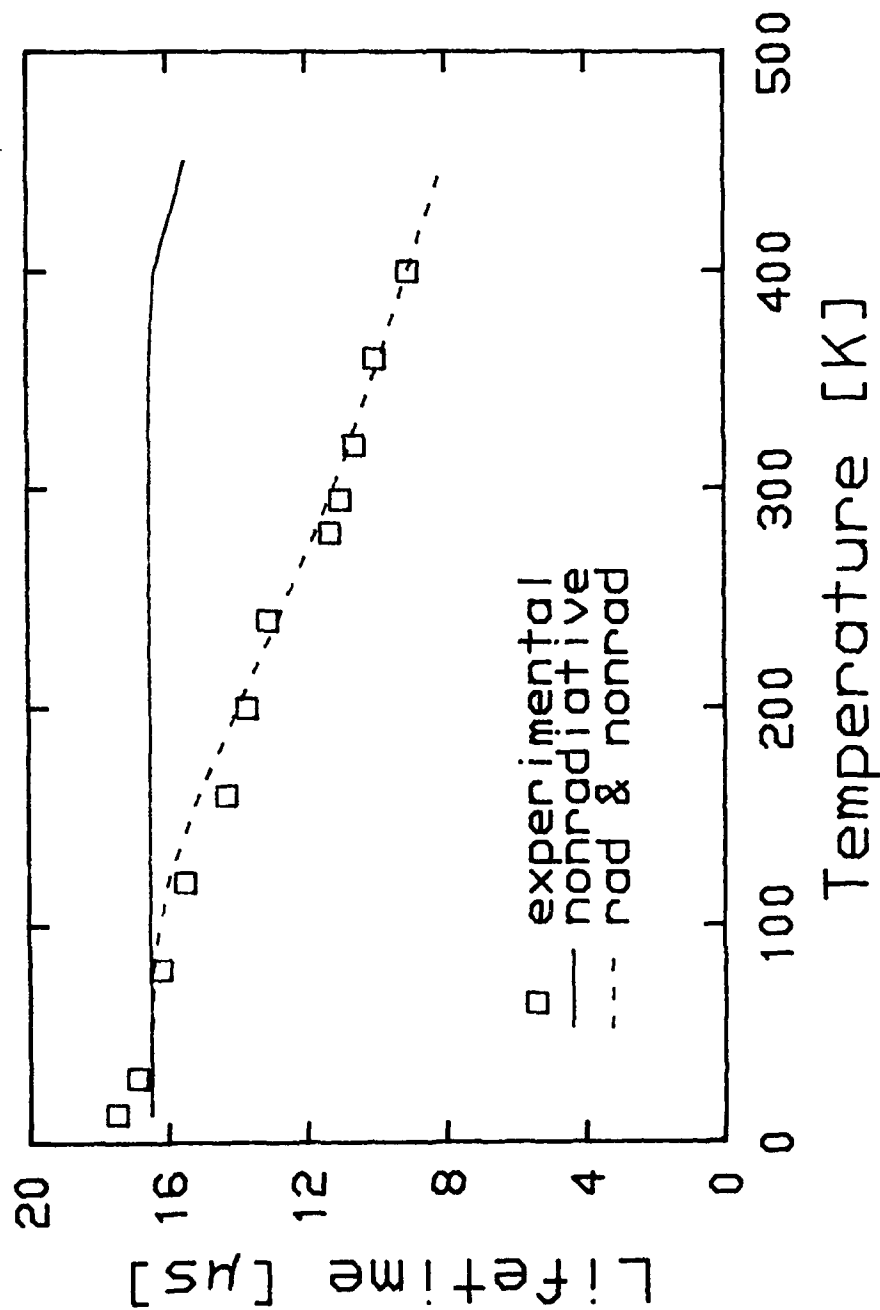


Figure 30. Model fit of $Ti^{3+}:YAlO_3$ fluorescence lifetime.

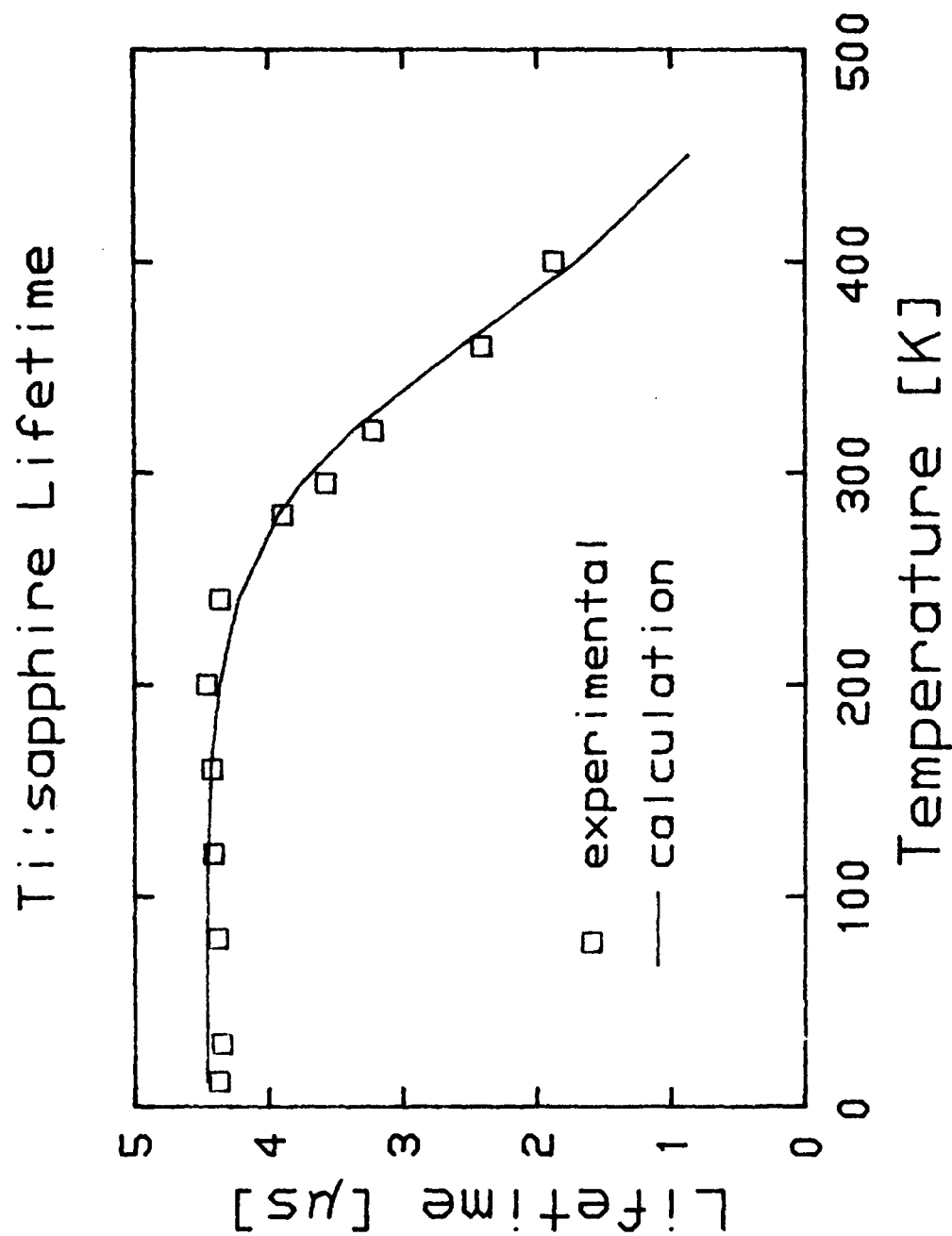


Figure 31. Model fit of Ti^{3+} :sapphire fluorescence lifetime.

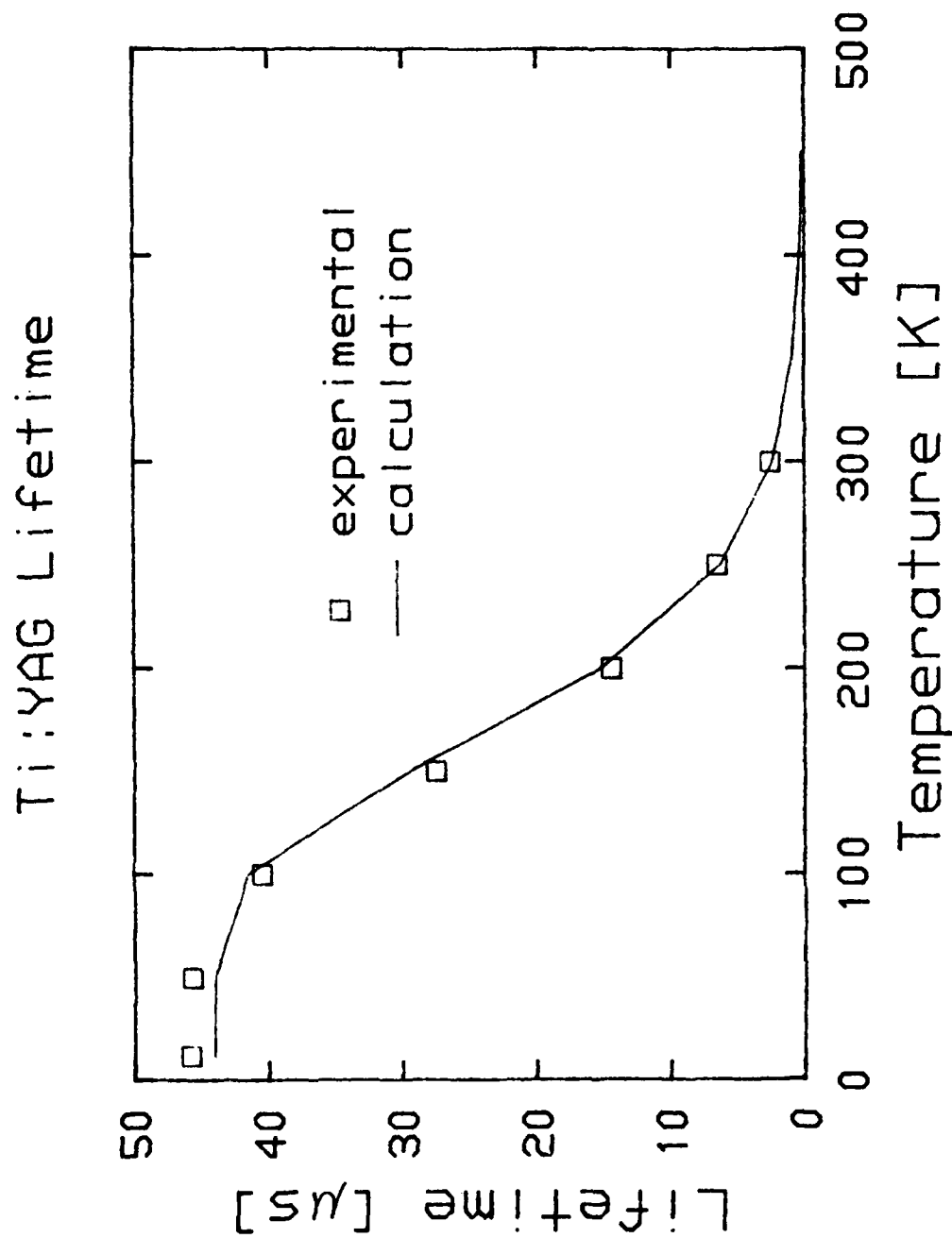


Figure 32. Model fit of Ti^{3+} :YAG fluorescence lifetime.

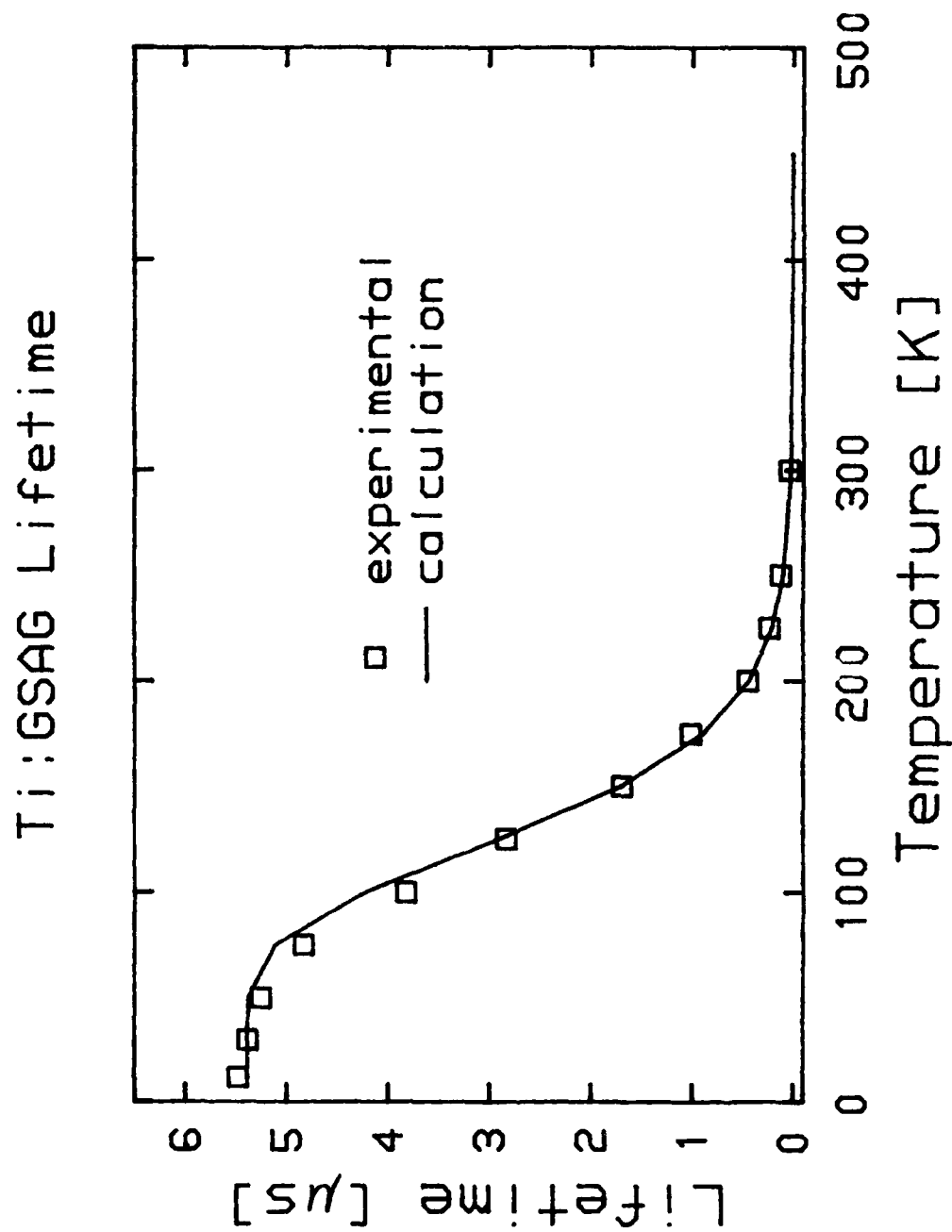


Figure 33. Model fit of Ti^{3+} :GSAG fluorescence lifetime.

Ti:sapphire has a smaller crystal field splitting than Ti:YAlO₃ and thus nonradiative transitions become more significant in this host material. At 10 K the nonradiative rate is more than 10⁵ times that of Ti:YAlO₃ and is 1% of the Ti:sapphire radiative rate. At room temperature the nonradiative rate increases by a factor of 23 resulting in a calculated fluorescence quantum efficiency of 82%. This agrees well with reported measurements of 70-80%. The fit to Ti:sapphire data shown in Figure 31 assumes that there is negligible change in vibrational relaxation rate. Fits were also done assuming large τ_{rad} and temperature dependent τ_{vib} . Very little difference was observed in the two types of fit with the one shown in Table 5 agreeing slightly better at temperatures where the decrease in lifetime begins.

The best fit for Ti:YAG τ_{rad} was achieved by using a very large τ_{rad} so that the radiative rate was dominated by the τ_{vib} term. Fits exchanging the roles of the two terms were not as good. The Ti:YAG fit follows the crystal field trend; the lower crystal field results in increased nonradiative rate compared to Ti:sapphire. But the radiative rate at low temperatures is also lower. A plausible explanation is that the octahedral crystal symmetry (with inversion symmetry) of YAG results in a longer radiative lifetime. The increased nonradiative rate and decreased radiative rate result in the important conclusion that even at low temperatures there is not 100% quantum efficiency. Table 5 shows a 19% quantum efficiency for Ti:YAG. This may explain why Ti:YAG fluorescence always seemed weaker than Ti:sapphire fluorescence. At room temperature the nonradiative transition rate is dominant with quantum efficiencies less than 2%. These low quantum efficiencies have not yet been confirmed experimentally but may explain why lasing in Ti:YAG has not yet been demonstrated.

The calculated lifetime curve for Ti:GSAG used a value for N much larger than in the other three hosts. Calculations using N

on the order of 5×10^{14} left the model curve shifted too far to the right. A physical explanation for the need to increase N by four orders of magnitude is not available. The value used for the vibrational lifetime was somewhat arbitrary. Using 30 μ s rather than 300 μ s resulted in a fit only marginally poorer. This means that the calculated quantum efficiency listed in Table 5 is not accurately determined by the model fit. But even using 30 μ s results in a calculated quantum efficiency less than Ti:YAG. Thus successful laser operation of Ti:GSAG, even at liquid helium temperatures, does not look promising.

There is a clear trend in the modeling results that as crystal field decreases the nonradiative rate increases. This results in (1) a decrease in quantum efficiency with decreasing crystal field and (2) a decrease in the temperature at which the nonradiative rate equals the radiative rate with decreasing crystal field. Thus Ti^{3+} doped host materials with crystal fields equal to or less than YAG are not good laser prospects, particularly for room temperature operation. In contrast, hosts with crystal fields greater than or equal to Ti:sapphire look like good prospects for efficient Ti^{3+} lasing.

SECTION 5

Laser Performance of Ti^{3+} Doped Sapphire

Ti^{3+} doped sapphire was first demonstrated to be a broadband tunable laser material by P. Moulton⁴ in 1982. However, crystal quality has continued to be a problem with this laser material. Scattering centers and spurious absorption in the spectral region where lasing is expected were found to reduce the lasing performance of many early Ti:sapphire crystals. To assess the state of the art in Ti:sapphire growth, laser crystals were procured from two crystal growth facilities, Union Carbide and Crystal Systems, in the first half of 1985. A crystal 48 mm long by 5 mm in diameter with Brewster angle ends was cut from a boule grown by the Czochralski (CZ) method. Crystal growth and fabrication were done by Union Carbide. The crystal had a nominal doping level of 0.1 wt% titanium. Another crystal was grown by Crystal Systems, Inc. using the Heat Exchanger Method (HEM); it also had Brewster angle ends but was 35 mm long and 7 mm in diameter. The Ti^{3+} doping level in the HEM crystal was calculated to be 0.03 wt% based on the relative absorption at 532 nm in the two crystals.

Laser performance of the CZ and HEM crystals was measured under identical optical pumping and laser resonator conditions. Figure 34 is a diagram of the experimental setup. The crystals were pumped at 532 nm with 10 ns, frequency doubled pulses from a Q-switched Nd:YAG laser. A 254 mm convex lens focused the pump beam onto the Ti:sapphire laser crystal. Actually, the crystal was placed slightly in front of the pump beam waist to provide a more effective overlap of the resonator mode volume with the pump beam diameter. The input mirror was flat-flat and coated to be transmissive (> 85%) at 532 nm but highly reflective (> 99%) in the 730-810 nm region. The output mirror was 50% reflective

Ti³⁺:sapphire Laser Diagram

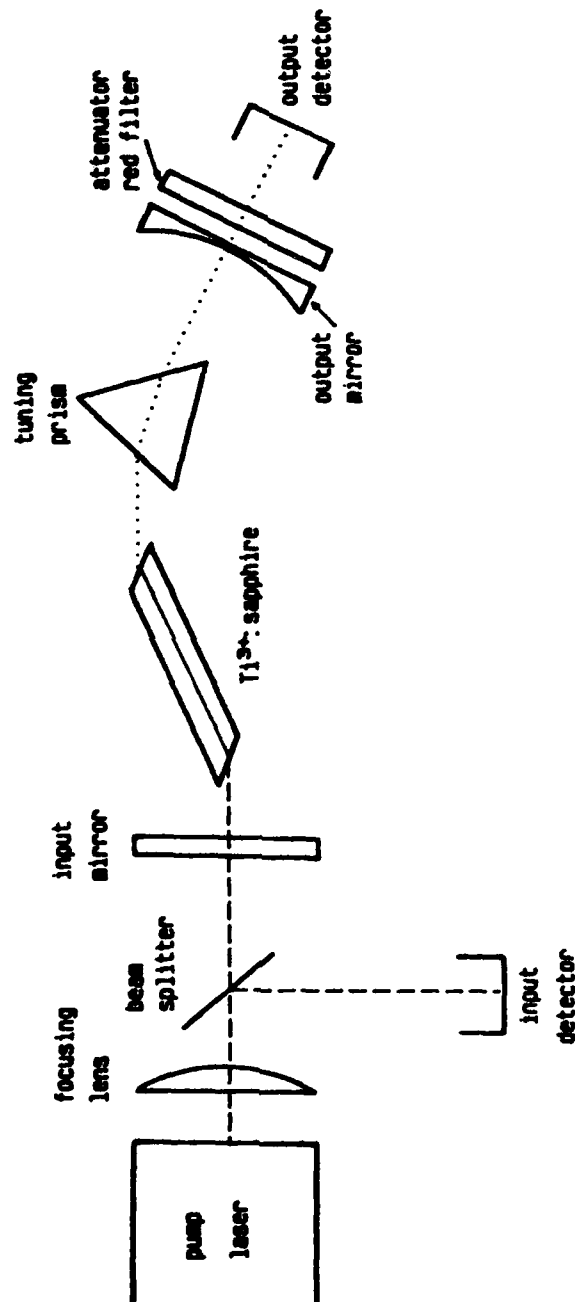


Figure 34. Experimental apparatus used to measure Ti³⁺:sapphire laser performance.

in the 730-810 nm region and had a 3 m radius of curvature on the resonator side; it was flat and had a broadband AR coating on the output side. In some experiments a prism was used to provide wavelength discrimination.

Input energy was measured using a pyroelectric detector to monitor the energy per pulse split off by a glass slide. The input energy detector was calibrated to the energy incident on the Ti:sapphire crystal surface. An identical detector was used to measure output energy by placing it behind a red filter used to block any unabsorbed pump radiation. Output energy per pulse vs input energy corrected for energy actually absorbed was measured and is shown in Figure 35 for both crystals. Threshold was 8 mJ for the CZ crystal and 10 mJ for the HEM crystal. The constant 0.6 mJ output shown in Figure 35 for input energy levels below threshold proved to be residual 1064 nm radiation from the pump Nd:YAG laser. Absorbed-energy slope efficiencies were 50% and 42% for the CZ and HEM crystals respectively. The HEM crystal, because of its lighter doping and shorter length, absorbed only 60% of the incident energy, whereas the CZ crystal absorbed 99% of the incident light. Quantum slope efficiency based on photons absorbed was nearly 100% for the HEM crystal and 72% for the CZ crystal.

The higher quantum efficiency of the HEM crystal was not directly related to its lower doping level. Combined absorption, reflection and scattering losses were measured by observing the pre- and post-crystal energies of 756-nm probe pulses generated by the Quantel H₂ Raman cell. The CZ crystal had a loss of 2.5%/cm and the HEM crystal had a loss of 2.2%/cm. Loss in a more heavily doped HEM-grown crystal (not tested for laser performance) was found to be 1.8%/cm. Both laser crystals were state-of-the-art for loss at that time since other crystals typically were reported to have losses greater than 3%/cm.

Figure 36 shows the tuning range (695-864 nm) for the HEM sample using a single pair of mirrors and a Brewster angle prism.

Laser Performance of Ti^{3+} :sapphire Samples

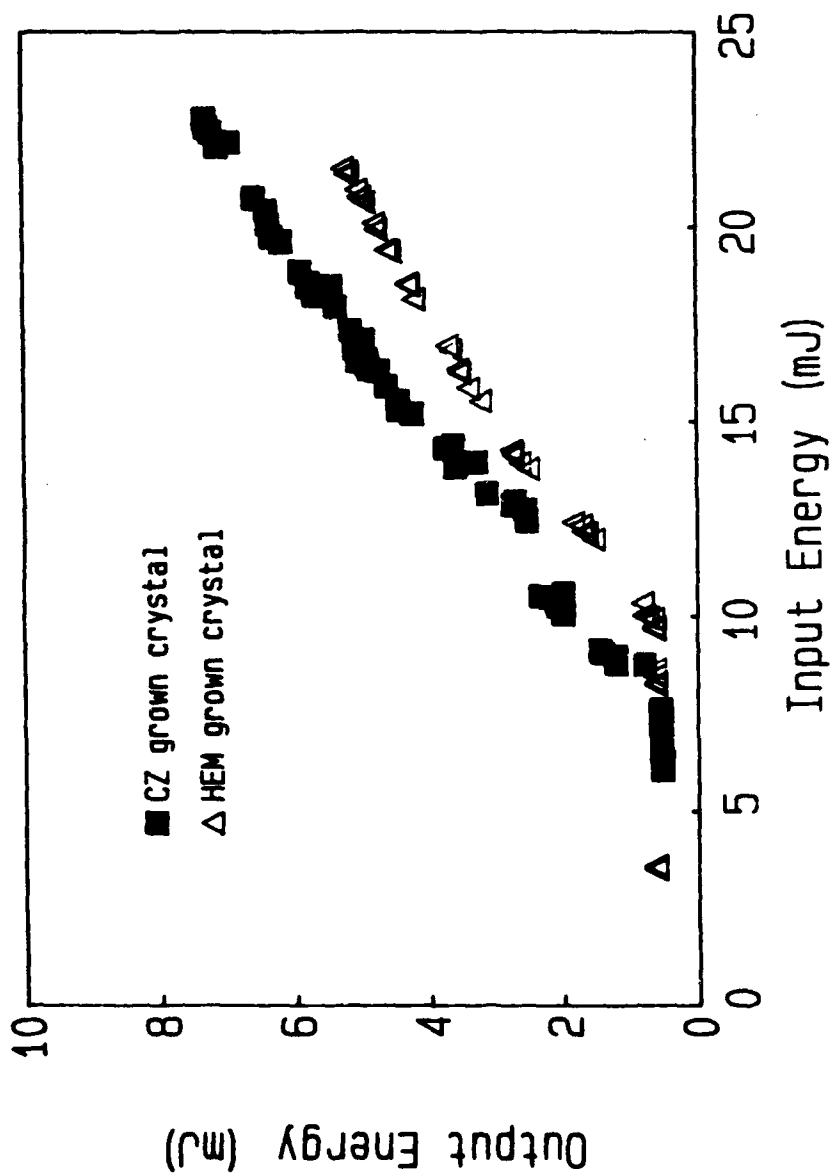


Figure 35. Ti^{3+} :sapphire laser performance when pumped with 532 nm, Q-switched pulses.

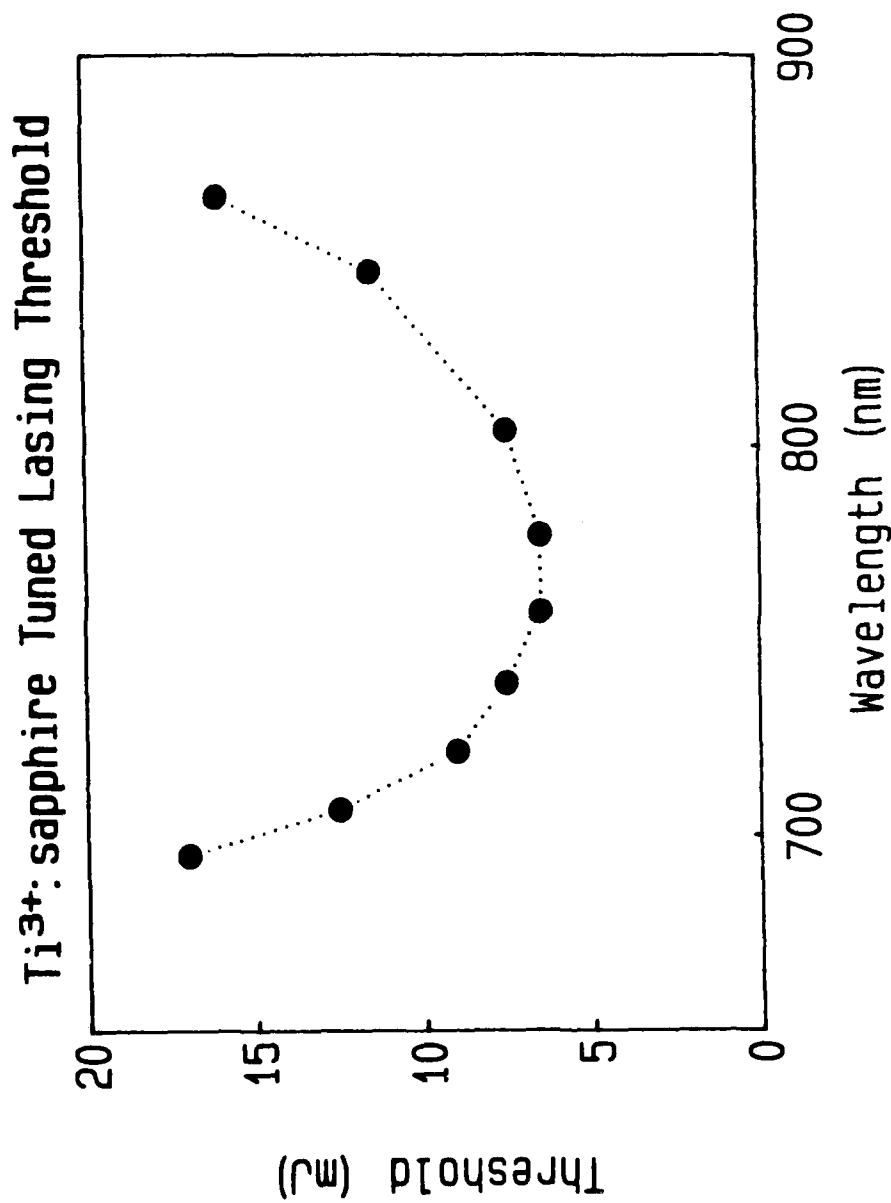


Figure 36. Ti³⁺:sapphire tuning demonstrated using a single set of mirrors.

Tuning was limited by bandwidths of the mirror coatings designed for the 730-810 nm region and surface damage of the laser crystal at input energies greater than 25 mJ. Use of a set of mirrors designed for operation in the 650-730 nm region was unsuccessful in producing output at shorter wavelengths.

Some very simple bandwidth measurements were made on the tuned and untuned laser pulses. With no wavelength selective element present, the output pulse was extremely broad in wavelength range. Output passed through a monochrometer was observable over a 40-nm range and centered near 770 nm. With the prism in the resonator the bandwidth decreased to approximately 0.5 nm. The broadband, untuned output results from the high gain present in the Ti:sapphire material and the low Q of the resonator. With a 0.5-m mirror separation the round trip time for a photon in the resonator is about 3 ns. Since the measured pulse width was less than 10 ns, no photon made more than a few round trips in the resonator. Thus the wavelength discrimination in the gain peak was poor. Including a prism added the condition that only a small wavelength band was be reflected back through the gain region of the crystal thus reducing the bandwidth.

The broadband tunability and the high conversion efficiency demonstrated in the two Ti:sapphire crystals investigated here show that Ti:sapphire is highly promising for a number of military and commercial applications. High quality material is available from two commercial sources and further improvements continue to be reported. Ready availability of laser quality material is key to further development. Further work is needed in scaling the output of this material to the 1 J/pulse level. Current laser performance is limited by damage to mirrors and crystal surfaces. Also, work on exploiting the broadband tunability of this material is just in its infancy. Ti:sapphire laser technology holds great promise and is now being developed at a number of laboratories.

SECTION 6

Cr,Nd:GSGG Lasing Performance

The idea of co-doping a neodymium laser material with another ion which could transfer absorbed energy to Nd^{3+} was suggested not long after the discovery of the Nd:YAG laser.²⁹ However, the results using Cr,Nd:YAG were disappointing. In Cr,Nd:YAG the Cr^{3+} to Nd^{3+} transfer rate was found to be slower than the Cr^{3+} relaxation rate resulting in poor energy transfer. More recently, gadolinium-scandium-gallium garnet (GSGG) co-doped with Cr^{3+} and Nd^{3+} ions was shown to have much better efficiency than Nd:YAG.⁵ The difference appears to be related to the improved overlap between the Cr^{3+} and Nd^{3+} excited state energy levels in GSGG making the energy transfer rate faster.

Cr,Nd:GSGG Spectroscopy

The absorption spectrum of Cr,Nd:GSGG shown in Figure 37 illustrates one clear advantage of using a co-dopant. The Nd^{3+} ions have very narrow absorption lines and thus absorb only a small fraction of the flashlamp emission. But the broad absorption bands of Cr^{3+} ions can efficiently absorb the broadband output of a flashlamp. Efficient transfer of Cr^{3+} excitation to Nd^{3+} ions can result in improved lasing efficiency.

The fluorescence spectrum of Figure 38 shows emission by both the Cr^{3+} and Nd^{3+} ions. The broadband emission centered at 767 nm is due to radiative relaxation from the $^4\text{T}_2$ to the $^4\text{A}_2$ levels of Cr^{3+} . The narrow dips in the Cr^{3+} emission are due to absorption at those wavelengths by Nd^{3+} ions. The sharp emission features at longer wavelengths are due to Nd^{3+} fluorescence. The Cr^{3+} emission is quite weak compared to GSGG doped only with chromium because most of the Cr^{3+} ions transfer their energy to

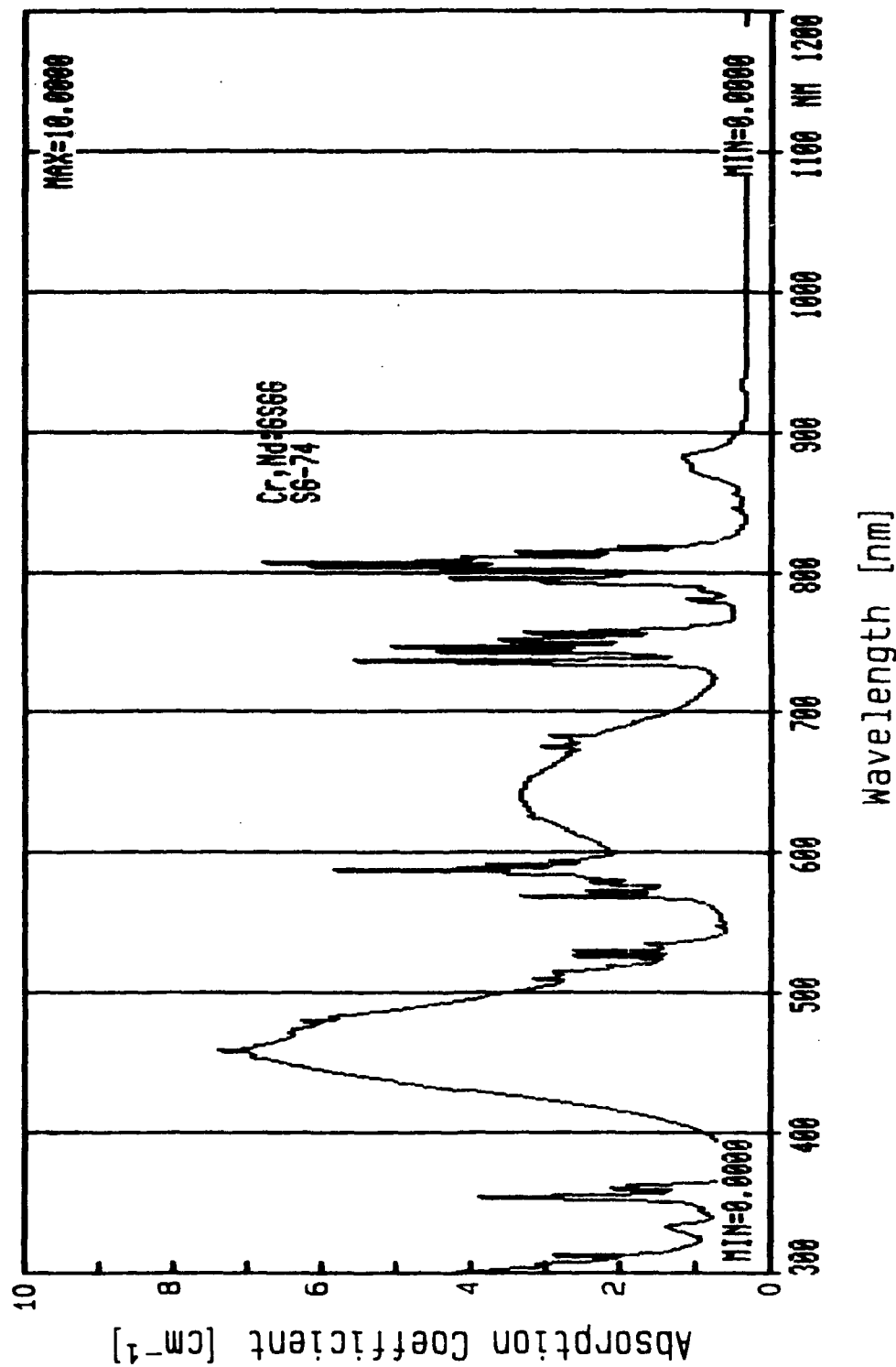


Figure 37. Cr,Nd:GSGG absorption spectrum. Broadband peaks at 460 and 640 nm are Cr³⁺ absorption; sharp peaks are Nd³⁺ absorption.

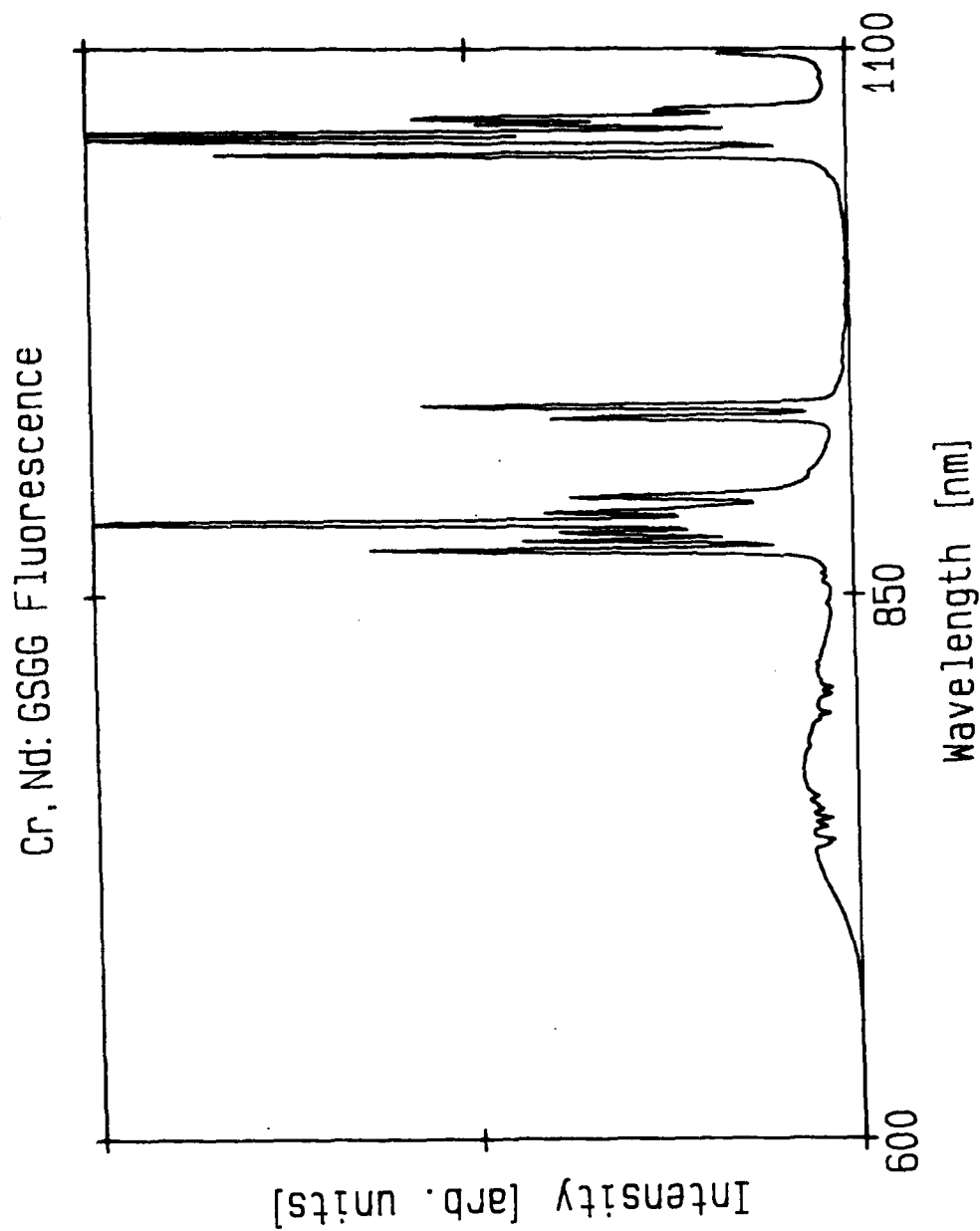


Figure 38. Cr, Nd: GSGG fluorescence at room temperature pumped by an argon ion laser at 488 nm.

Nd³⁺ ions in the co-doped crystal. Further details of Cr,Nd:GSGG spectroscopy and energy transfer kinetics were studied as part of a Masters Thesis project and will be reported elsewhere.³⁰

Long-Pulse Lasing Performance

Comparison of lasing performance was first accomplished using an on-hand, 1/4" x 3" Nd:YAG laser rod and a 5 mm x 80 mm Cr,Nd:GSGG laser rod grown by Airtron. The different rod dimensions made direct performance comparisons less than ideal but allowed setup of the experiment and collection of preliminary data. The GSGG rod had a Nd concentration of 2×10^{20} ions/cm³ and a Cr concentration of 1×10^{20} ions/cm³. Figure 39 shows laser output energy using the same resonator cavity for both rods. The resonator consisted of an HR mirror and a 90% reflectivity output mirror with a Kigre cavity holding the laser rod and flashlamp. Flowing coolant water was held at 20° C and the repetition rate was 2.5 Hz. Threshold input energy was near 1 J for both materials. Maximum output was 700 mJ/pulse for GSGG and 410 mJ/pulse for YAG with 25 J of flashlamp input energy. Cr,Nd:GSGG and Nd:YAG slope efficiencies were 3.8% and 2.2%, respectively; the GSGG:YAG ratio of slope efficiencies (1.7) agrees well with the relative efficiencies reported by Pruss et al.²

The coolant temperature was varied to see if GSGG performance changed with temperature. Measurements at 10°, 20°, and 30° C gave nearly identical results as expected. However, degradation in output was observed when returning to near-threshold energies after pumping at much higher flashlamp energies. Figure 40 shows output energy near threshold as a function of time after the GSGG rod had been pumped with high-energy (20 J) flashlamp pulses at three different temperatures. In all three cases, the output energy is less than what it was before high-energy flashlamp pumping but then the output energy

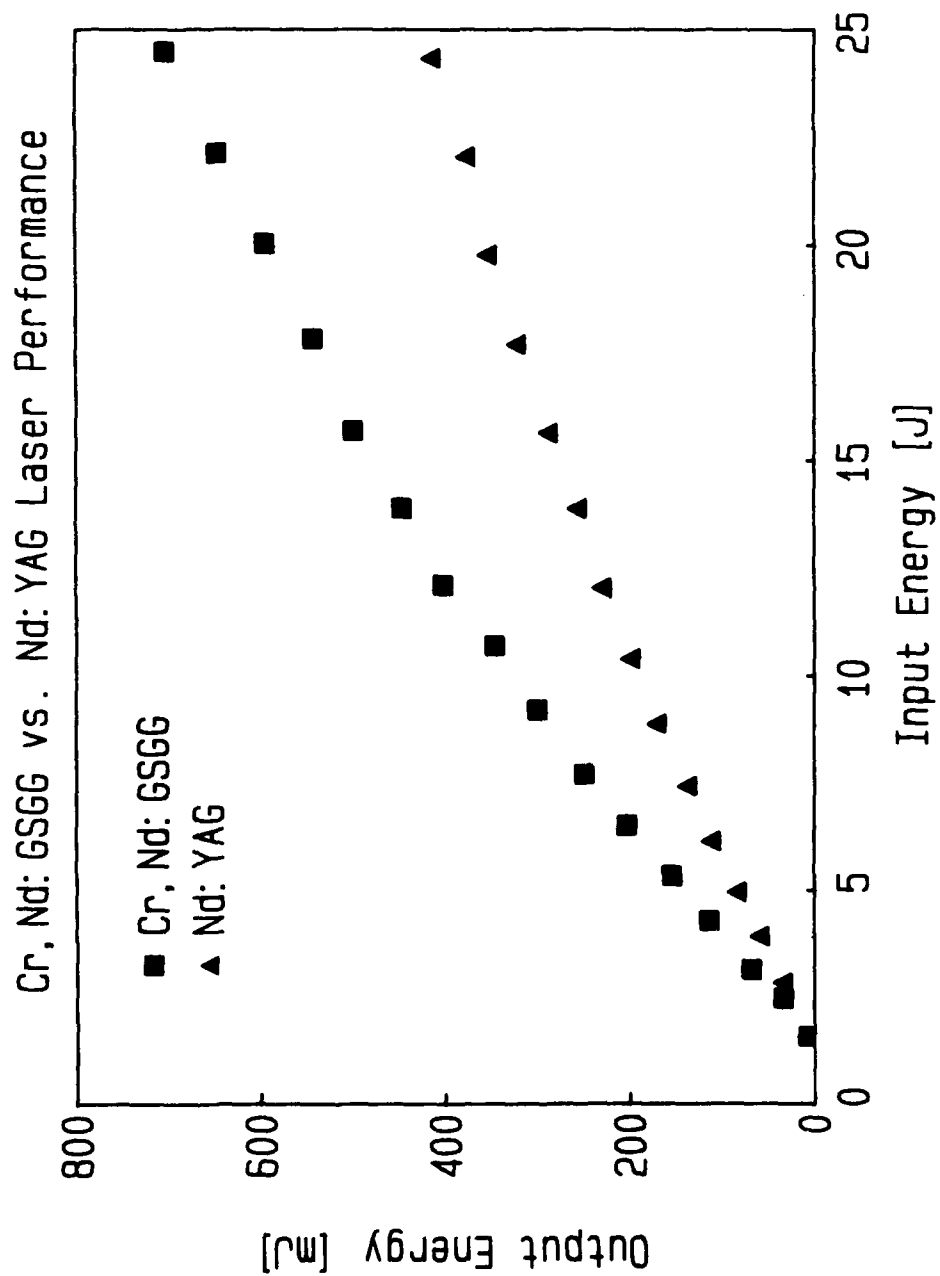


Figure 39. Laser performance of Cr,Nd:GSGG and Nd:YAG. Rod diameters were 5 mm and 1/4 inch respectively.

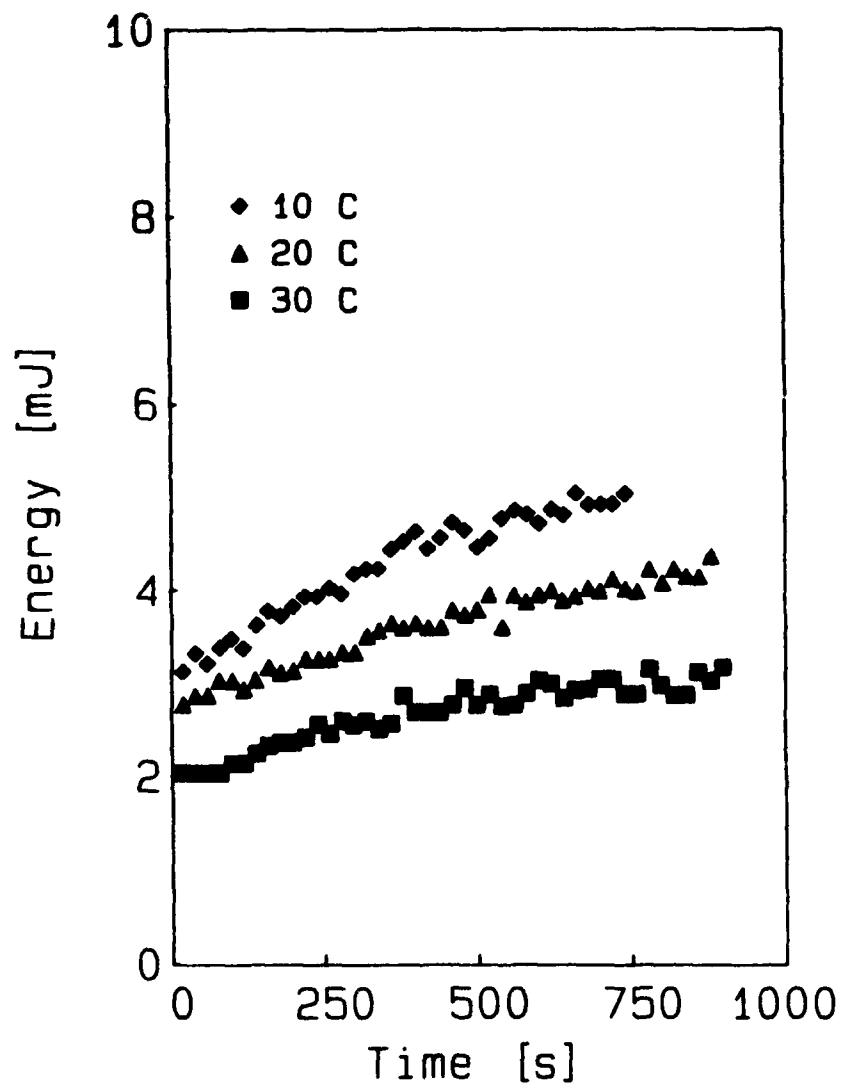


Figure 40. Long term change in laser output near threshold after pumping at high input energies.

gradually increases with time. The lifetime of this effect is quite long, 800 seconds, so thermal effects can be ruled out. A small amount of solarization may be occurring. Similar effects, but much smaller in magnitude, were observed in Nd:YAG. Thus there are indications that solarization (and subsequently poorer performance) could be a more significant problem in GSGG than it is in YAG.

Sample rods were purchased from Airtron, Allied and Materials Progress to investigate (1) material quality issues, (2) the effects of different Cr^{3+} and Nd^{3+} concentrations on laser performance in GSGG, and (3) the relative performance of equally sized YAG and GSGG laser rods, . Table 7 lists the laser rods purchased and some of their performance data.

Table 7
Laser Rod Doping Levels

Grower	$\text{Cr}^{3+} [10^{20}/\text{cm}^3]$	$\text{Nd}^{3+} [10^{20}/\text{cm}^3]$	ID	Host	Slope [%]
Airtron	2	2	SG-91-1	GSGG	8.9
Airtron	1	2	SG-74-6	GSGG	7.7
Allied	2	2	ALD-023	GSGG	8.2
					6.9*
Allied	1	1	ALD-026	GSGG	5.7
Mat Prog		2	M1770	YAG	
Mat Prog		2	M1771	YAG	4.7*

* These slope efficiencies were measured with a Q-switch crystal in the resonator but no voltage was applied.

The long-pulse laser performance of the GSGG rods is shown in Figure 41. In this case the laser resonator consisted of a flat/flat, 50% reflectivity, output mirror, a 3-m radius of curvature HR mirror and the same Kigre cavity used earlier. The two mirrors were spaced 1 m apart. Energy per pulse was measured with a Laser Precision meter and averaged over 50 pulses for each input energy plotted in Figure 41.

Laser performance was clearly sensitive to Nd^{3+} concentra-

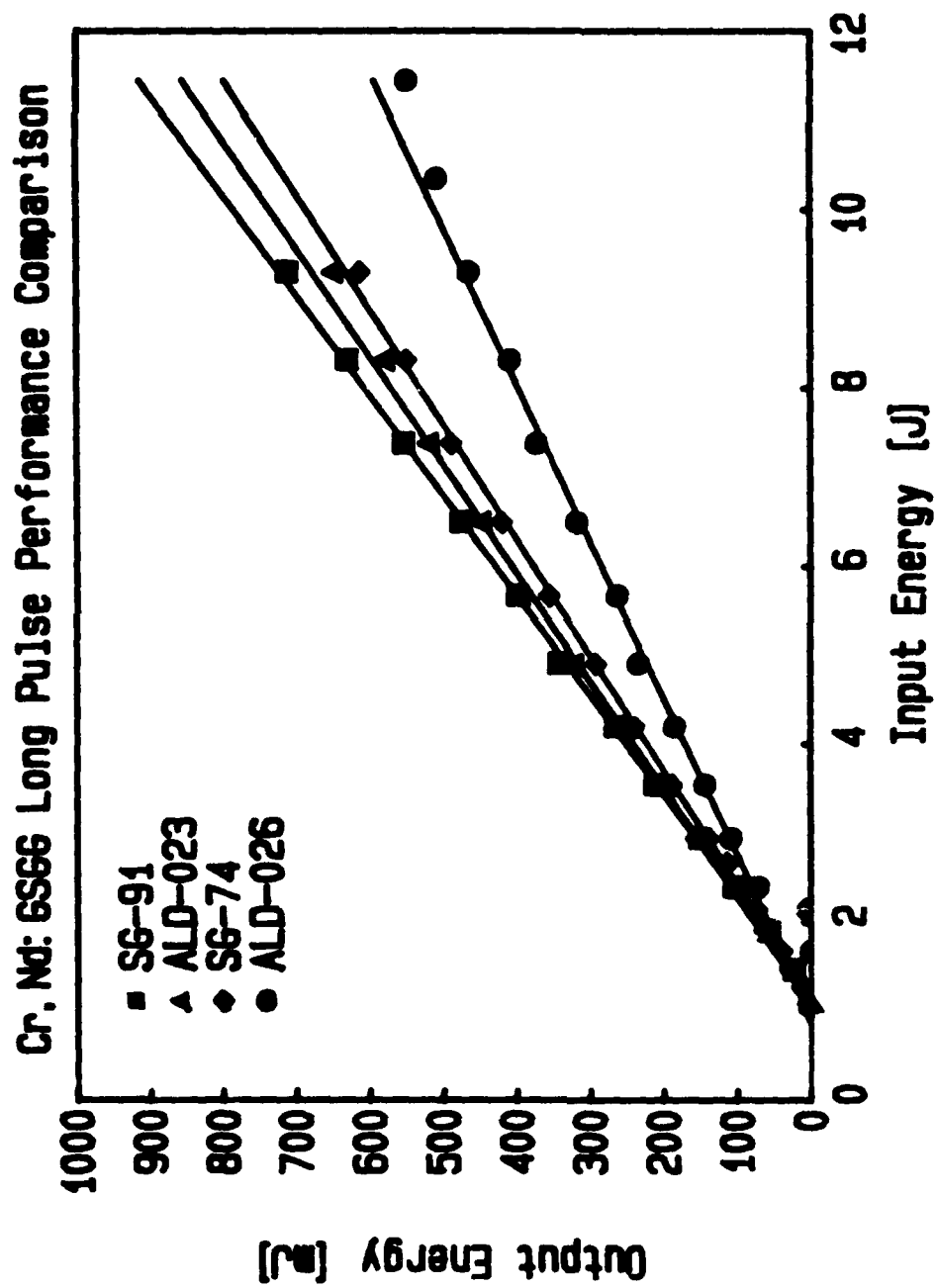


Figure 41. Cr,Nd:GSGG long-pulse laser performance.

tion; ALD-026, the GSGG rod with 1×10^{20} Nd^{3+} ions/ cm^3 (half the Nd^{3+} concentration of the other three rods) had a slope efficiency of 5.7%. The rod with the same chromium concentration but twice the Nd^{3+} concentration had a slope efficiency of 7.7%. In contrast, changing the chromium concentration by a factor of two resulted in only minor changes in performance. The difference in performance between the two rods with nominally equal dopings of Cr^{3+} (but from different sources) was similar in magnitude to the difference in performance of ALD-023 and SG-74 where the Nd^{3+} concentration was kept constant but the Cr^{3+} concentration changed by a factor of two.

Although it is clear that the 2×10^{20} ions/ cm^3 concentration level for Cr^{3+} and Nd^{3+} ions was the best combination tested, the concentration parameter space was not thoroughly investigated to find the optimum concentrations. The cost of each individual growth run and the problems of learning how to grow laser quality crystals when the doping levels are changed makes optimization a difficult and expensive task.

Q-switched Laser Performance

GSGG and YAG Q-switched laser performances were investigated by adding a Q-switch crystal (Inrad 202-092) and a thin-film polarizer to the same resonator used for the GSGG long-pulse measurements. M1771 (Nd:YAG) and ALD-023 (Cr,Nd:GSGG) were used. With the Q-switch off (but still in the resonator) and with the polarizer removed, the slope efficiencies of YAG and GSGG were 4.7% and 6.9% respectively (see Figure 42). The factor of 1.5 improvement of GSGG over YAG is less than the factor of 2 typically reported but the YAG rod manufacturer indicated that he had sent particularly "hot" laser rods with Nd^{3+} concentrations which may be slightly higher than those listed in Table 7. Certainly, 4.7% slope efficiency is quite good for Nd:YAG.

Figure 43 shows that when Q-switched, both YAG and GSGG had

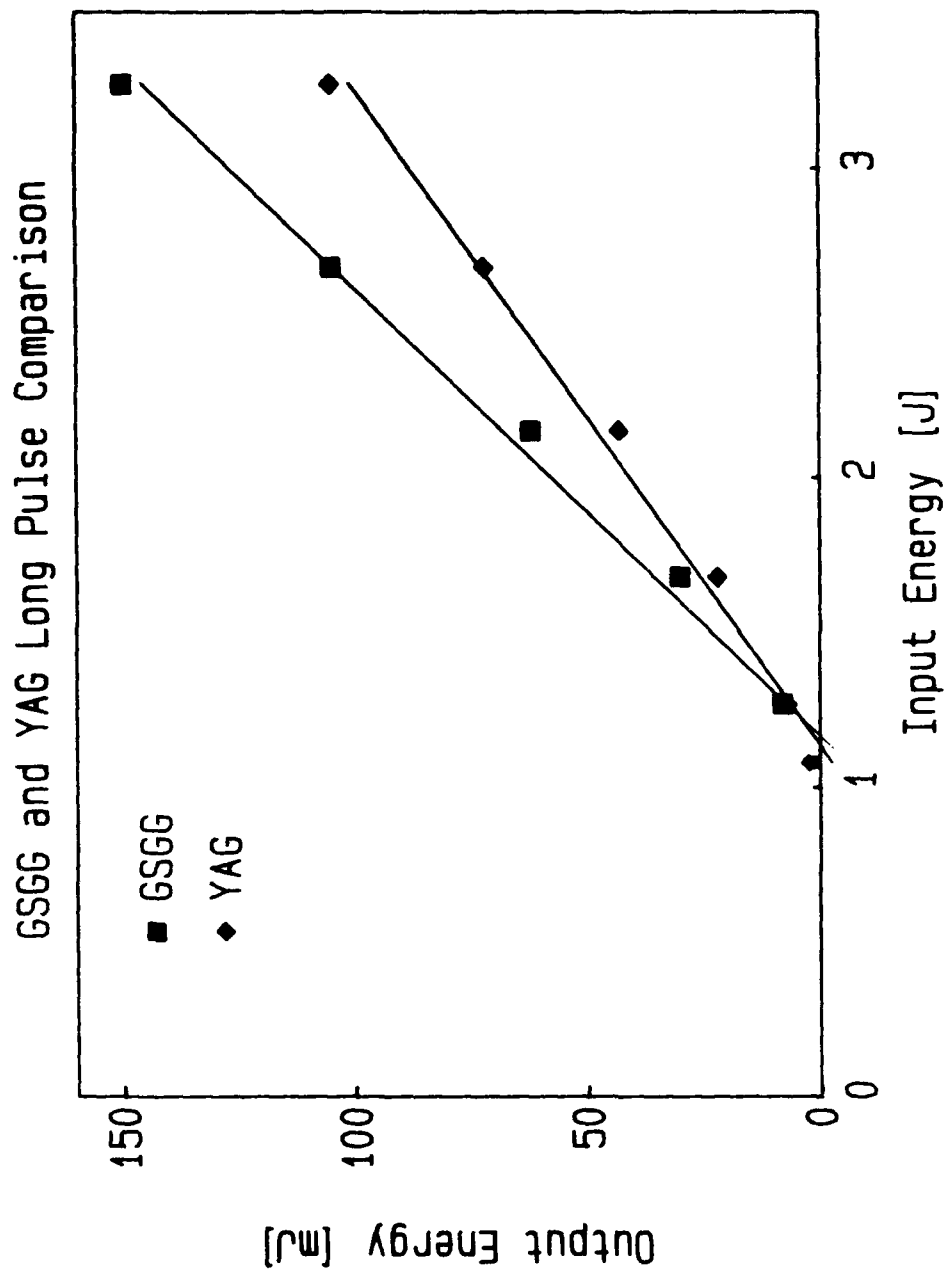


Figure 42. Cr,Nd:GS GG vs. Nd:YAG long-pulse laser performance.

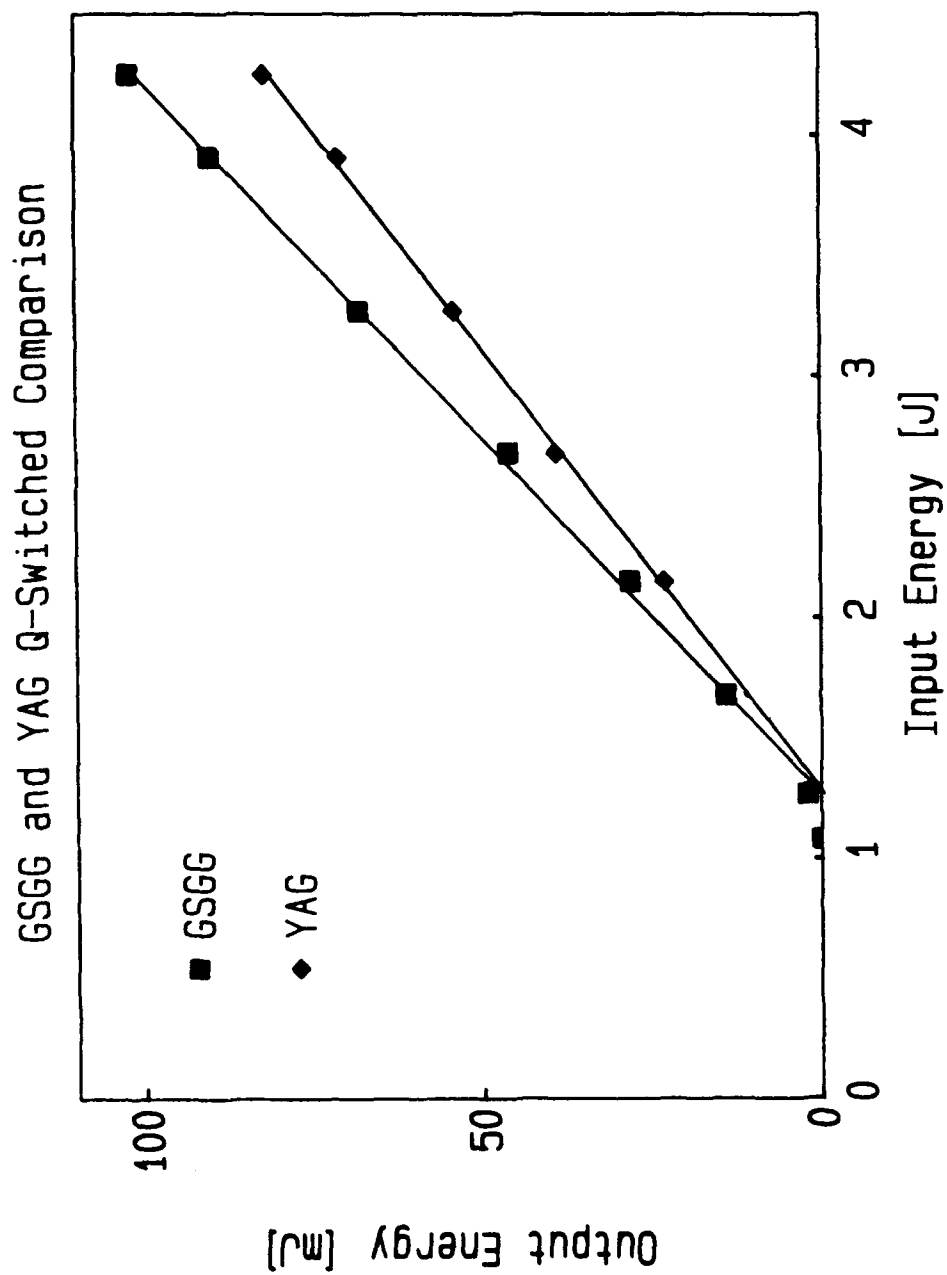


Figure 43. Cr,Nd:GSGG vs. Nd:YAG Q-switched laser performance.

reduced slope efficiencies of 2.7% and 3.4% respectively. The decrease in slope efficiency was significantly larger in GSGG $[(6.9 - 3.4)/6.9 = .51]$ than in YAG $[(4.7 - 2.7)/4.7 = .43]$. The majority of the loss appeared to be thermally induced birefringence because similar reductions in output occurred when the resonator was operated in long-pulse mode with the thin-film polarizer still in place. The larger effect in GSGG may be due to its poorer thermal conductivity.

Although beam size and divergence were not studied in detail, there was a noticeable difference in beam shape between the YAG and GSGG Q-switched pulses. Using burn paper for simple analysis, the GSGG pulses were much more elliptical in shape than the YAG pulses were. The major axis of the GSGG pulses was along the polarization axis.

Pulse widths were measured for the Q-switched pulses using a fast photodiode with 1-ns response time. Single Q-switched pulses were observed with no evidence of long-pulse leakage or later Q-switched spikes in both YAG and GSGG. At 2x threshold the full width at half maximum [FWHM] was 70 ns and at 4x threshold the FWHM pulse width narrowed to 42 ns (see Figure 44). The YAG Q-switched pulse width at about 4x threshold was 33 ns, a little shorter (see Figure 45). This is expected since YAG has a higher gain than GSGG.

In summary, Cr,Nd:GSGG can produce higher laser efficiency than Nd:YAG when optimally doped with Cr^{3+} and Nd^{3+} ions. The major improvement in efficiency (1.5 to 2 times better slope efficiency) available in GSGG will make this material attractive where power supply size and weight requirements are critical. However, Cr,Nd:GSGG is not an exact replacement for Nd:YAG. Differences in gain, thermal birefringence and thermal conductivity of the two materials require different engineering approaches when designing a laser. Particular system requirements will dictate which of the two host materials should be used.

Cr, Nd: GSGG Q-Switched Pulse Width

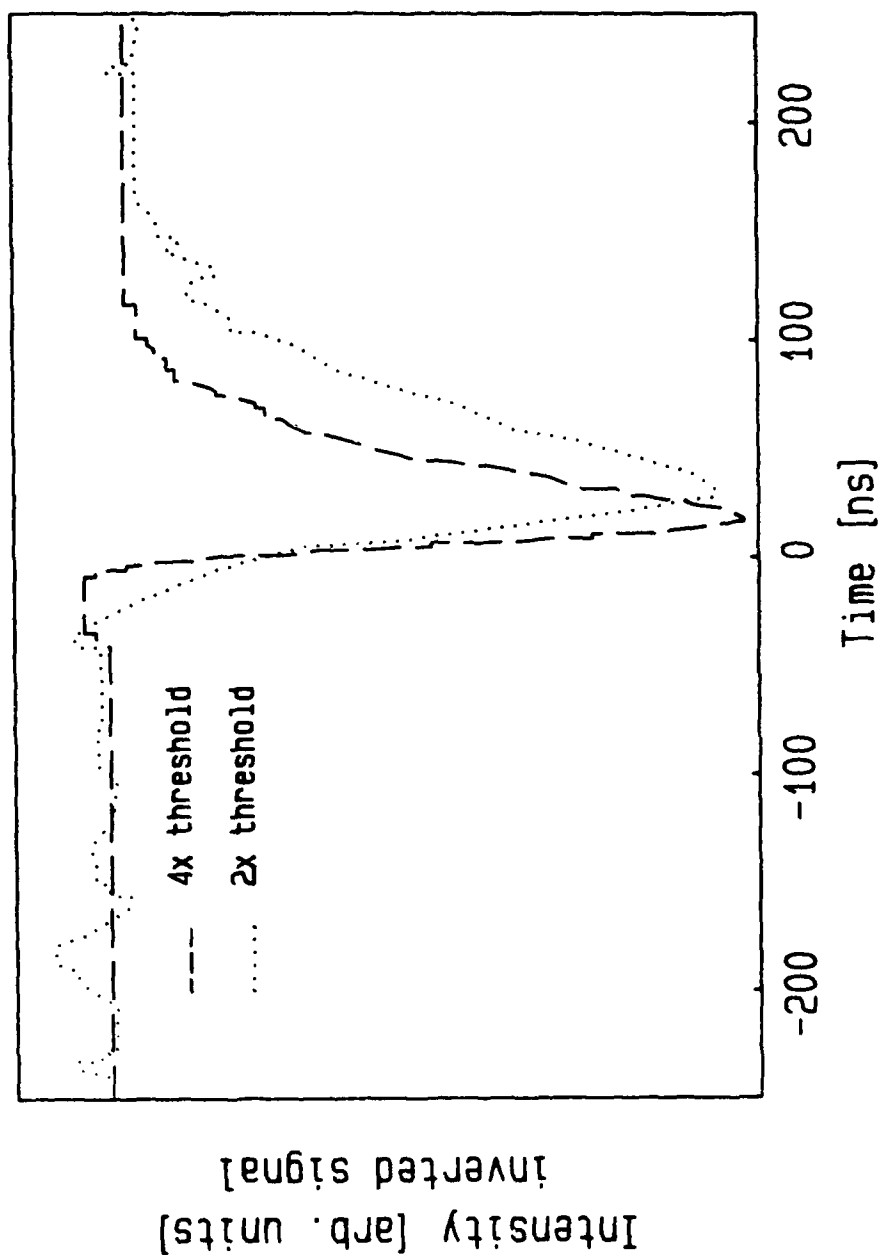


Figure 44. Cr,Nd:GSGG Q-switched pulse width for two pump energies.

Nd:YAG Q-Switched Pulse Width

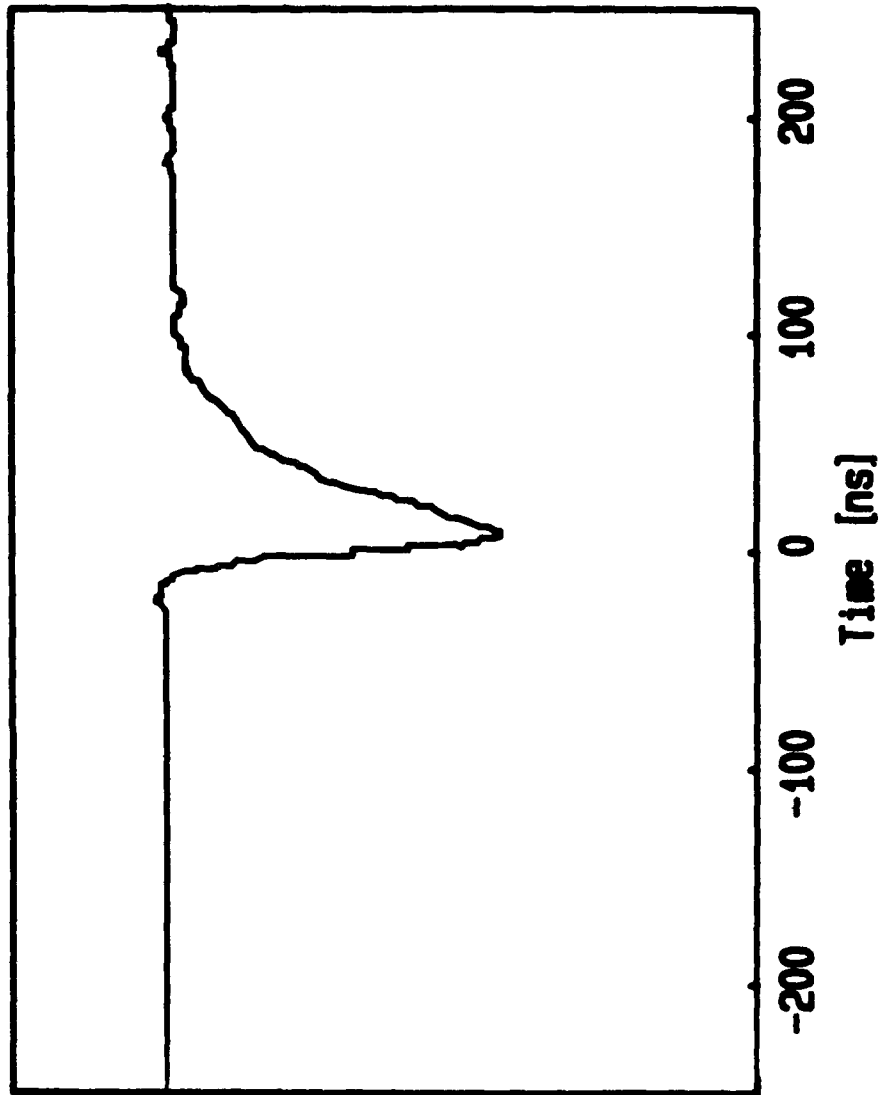


Figure 45. Nd:YAG Q-switched pulse width.

REFERENCES

1. J. E. Geusic, H. M. Marcos and L. G. Van Uitert, Appl. Phys. Lett. 4, 182 (1964).
2. J. C. Walling, H. P. Jenssen, R. C. Morris, E. W. O'Dell and O. G. Peterson, Optical Society of America Annual Meeting, Nov. 1978.
3. Contract F19628-85-C-0002 with MIT Lincoln Laboratories, Workunit 20010192.
4. P. F. Moulton, Opt. News 8, 9 (1982).
5. D. Pruss, G. Huber, A. Beimowski, V. V. Laptev, I. A. Shcherbakov and E. V. Zharikov, Appl. Phys. B28, 355 (1982).
6. P. F. Moulton, J. Opt. Soc. Am. B 3, 125 (1986).
7. A. Sanchez, private communication.
8. B.F. Gachter and J.A. Koningstein, J. Chem. Phys. 60, 2003 (1974).
9. E.D. Nelson, J.Y. Young and A.L. Schawlow, Phys. Rev. 156, 298 (1967).
10. R. C. Powell, G. E. Venikouas, L. Xi, J. K. Tyminski and M. R. Kokta, J. Chem. Phys. 84, 662 (1986).
11. M. J. Weber and T. E. Varitimos, J. Appl. Phys. 45, 810 (1974).
12. A. Sanchez of MIT Lincoln Lab attempted to observe cw pumped lasing of a sample provided by AFWAL/AADO.
13. Private conversation with P. Moulton, Schwartz Electro-Optics.
14. B. Perner, Jiri Kvapil and Josef Kvapil, Czech. J. Phys. B 38, 181 (1988).
15. K. Schepler and M. Kokta, J. Appl. Phys. 63, 960 (1988).
16. Y. Tanabe and S. Sugano, J. Phys. Soc. Japan 2, 753 and 766 (1954).
17. A. von Hippel, Z. Physik 101, 680 (1936).

18. F. Seitz, Trans. Faraday Soc. 35, 74 (1939).
19. C. C. Klick and J. H. Schulman, Solid State Phys. 5, 97 (1957).
20. M. D. Sturge, The Jahn-Teller Effect in Solids, Solid State Physics Advances in Research and Applications Vol. 20, p. 110, Academic Press, New York (1967).
21. J. Franck, Trans. Faraday Soc. 21, 536 (1925).
22. E. U. Condon, Phys. Rev. 32, 858 (1928).
23. H. A. Jahn and E. Teller, Proc. Roy. Soc. A161, 220 (1937).
24. R. M. Macfarlane, J. Y. Wong and M. D. Sturge, Phys. Rev. 166, 250 (1968).
25. P. Albers, "Ti³⁺ dotierter Saphir und YAG : Elektron-Phonon-Kopplung und Lasereigenschaften eines 3d¹-Elektronen-systems," Doctoral Dissertation, University of Hamburg, 1985.
26. B. Di Bartolo and R. Peccei, Phys. Rev. 6, A1770 (1965).
27. N. F. Mott, Proc. Roy. Soc. (London) A167, 384 (1938).
28. C. W. Struck and W. H. Fonger, J. of Lumin. 10, 1 (1975).
29. Z. J. Kiss and R. C. Duncan, Appl. Phys. Letters 5, 200 (1964).
30. W. Deleranko, "Energy Transfer Kinetics of Cr,Nd:GSGG," Masters Thesis, Wright State University, to be published.